

UNIVERSITÀ DEGLI STUDI DI MODENA E REGGIO EMILIA

Facoltà di Ingegneria “Enzo Ferrari”

Ph.D. In: Ingegneria Industriale e del territorio Enzo Ferrari

**Procedures for the InterLaminar Tensile Stress evaluation in
Finite Elements modeled curved laminates: critical
assessments and application to Formula One components.**

Tutor:

Prof. Enrico Bertocchi

Candidate:

Sergio Fanelli

School director:

Alberto Muscio

XXXII cycle

Index

1. Introduction.....	5
2. Composites materials.....	7
3. Damage in composite materials.....	9
3.1 <i>Interfacial debonding:</i>	9
3.2 <i>Matrix microcracking / Intralaminar cracking</i>	10
3.3 <i>Interfacial sliding</i>	11
3.4 <i>Delamination / Interlaminar Cracking</i>	11
3.5 <i>Fiber breakage</i>	12
3.6 <i>Void growth and manufacturing defects</i>	12
4. Delamination and Interlaminar Stresses	13
4.1 <i>Free edges</i>	14
4.2 <i>Holes and exposed surfaces through-the-thickness</i>	15
4.3 <i>Low velocity impacts</i>	16
4.4 <i>Matrix cracks</i>	16
4.5 <i>Out of plane joints</i>	17
5. State of the art.....	19
5.1 <i>Analytical methods</i>	20
5.2 <i>Numerical methods</i>	21
5.2.1 <i>2D shell and plates</i>	22
5.2.2 <i>3D elements</i>	24
5.2.3 <i>Shell/3D elements</i>	25
5.3 <i>Failure Criteria: VCCT and CZM</i>	25
5.4 <i>X-FEM and enriched shells</i>	28
5.6 <i>Experimental tests</i>	30
6. Post processing analytical model implementation	32
6.1 <i>Geometric curvature radii estimation techniques</i>	33
6.1.1 <i>Geometric curvature Radii estimation: Projection on principal planes</i>	

<i>method</i>	35
6.1.2 <i>Geometric curvature Radii estimation: differential geometry surfaces method</i>	39
6.2.3 <i>Geometric curvature Radii estimation: methods comparison</i>	42
6.2 <i>Radial Equilibrium equation</i>	45
6.3 <i>Numerical resolution of radial equilibrium</i>	48
6.4 <i>A comparison of curvature aware and curvature unaware laminate theories</i> . .	50
6.5 <i>Laminate features influencing ILTS</i>	56
6.5.1 <i>Results: E1/E3 variation</i>	57
6.5.2 <i>Results: C/LT variation</i>	58
6.6 <i>Model Implementation</i>	60
6.6.1 <i>Required information</i>	60
6.6.2 <i>Out of plane materials' properties</i>	61
6.6.3 <i>Systems of References</i>	61
7. Single geometric curvature FE Test	63
7.1 <i>Single geometric curvature FE Test: Results</i>	66
7.1.1 <i>Single geometric curvature FE Test: maximum ILTS Value</i>	66
7.1.2 <i>Single geometric curvature FE Test: maximum ILTS region</i>	67
7.1.3 <i>Single geometric curvature FE Test: ILTS distribution through-the-thickness</i>	68
7.1.4 <i>Single geometric curvature FE Test: Minimum integration points</i>	74
7.1.5 <i>Single geometric curvature FE Test: Non-aligned mesh</i>	75
7.1.6 <i>Single geometric curvature FE Test: Angled anisotropic plies</i>	76
8. Enhancing model: introducing in - plane deformations	78
9. Enhanced analytical model: test results	80
10. Double geometric curvature FE Test	82
10.1 <i>Double geometric curvature FE Test: Spherical Cap</i>	82
10.2 <i>Double geometric curvature FE Test: Double elbow tube</i>	84
10.3 <i>Double geometric curvature FE Test: Change of curvature</i>	87
11. Single geometric curvature FE Test: deformative curvature purposely not aligned with the principal directions of geometric curvature	95

12. Postprocessing 3D FE model: an alternative to the analytical postprocessing model.....	100
13. Design application: Ferrari Formula One Front Wing.....	104
<i>13.1 Front Wing FE Test: Results.....</i>	<i>108</i>
14. Conclusions.....	112
REFERENCES.....	117

1. Introduction

The present work focuses on the delamination issue that can occur in fiber composite materials. Delamination of composite material is a type of damage that highly compromises the stiffness and strength of components made by composite materials. Since these particular materials are being used on structural applications, the possibility to have available a practical tool that could help foresee the occurrence of delamination during the design phase has been extensively investigated. In this study, an analytical post processing model for the calculation of the Interlaminar Tensile Stress (ILTS) has been implemented to be coupled with 2D Finite Elements (FE) models. The ILTS can be used as an indicator of the state of the interface between two layers of a fiber composite component, alongside the Interlaminar Shear Stress (ILSS). During the design process of every structural component, the evaluation of its strength is usually investigated using a Finite Element Model (FEM), i.e. a numerical discretization of the component. In general, due to their construction and large surfaces with relatively thin thicknesses, fiber composite components are relatively easy to be discretized with 2D shells FE. In comparison to the 3D Solid FE models, 2D shells have a great advantage in terms of computational cost, providing at the same time accurate results. During the design process of fiber composite components, a required low computational effort represents an important gain especially in some contexts as The Formula One. Indeed, the possibility to spare computational time for a technical department influences the development of competitive projects. The advanced shells and plates theories for 2D FE can add the ILSS to the results obtained with 2D Shell FE models, but they are unable to predict ILTS. This study investigates the development of a low computational effort tool to calculate ILTS. The ILTS can be calculated with: analytical methods, numerical methods and obviously with experimental tests. The analytical methods exist for composite laminates with simple geometries, loading and boundary conditions. Nevertheless, analytical methods are usually used as post processing methods by integrating equilibrium equations of 3D elasticity instead of using constitutive relations. Numerical methods are capable to calculate the ILTS, but through complex models. Indeed, the 2D and 3D FE models can be integrated with techniques involving failure

criteria as the virtual crack closure technique (VCCT) and cohesive zone method (CZM) but the computational effort becomes too high. Some advanced shell Finite Elements called “X-FEM” and “enriched shells” are computationally more efficient but remain still very complicated when compared to the traditional 2D shell FE models.

The implemented model combines the 2D shell FE model computing agility with a simple post processing analytical model that can be applied on a doubly curve laminate. The analytical model is based on the solution given by Huang [1] and utilized by Roos in [2]. The post processing analytical model bases the ILTS calculation on the strain results of the 2D shell FE model and the geometric curvature radii estimation of the geometry. In this study, two alternative methods for the geometric curvature radii calculation exposed by Roos [3] are presented. Both the methods rely on an auxiliary eight noded quadrilateral mesh, which may be easily produced by commonly available FE preprocessors, thus being applicable to each single element regardless of the topology of its neighborhood. Moreover, the ILTS calculation uses the principal geometric curvature system as reference system, instead of the principal strain coordinate system. Before testing it on a complex component as a Ferrari Formula One front wing, it was tested on single geometric curvature and simple double geometric curvatures models. The tests on the single geometric curvature were performed using various geometric curvature radius / laminate thickness ratio (C/LT) and angled plies laminates. The test with angled highly anisotropic laminates highlighted a deficiency of the analytical model regarding the exclusion of the in plane shear term from the stiffness matrix. Indeed it does not directly participate to the ILTS equilibrium equation but its relevance is emphasized in angled plies stiffness matrices. The enhanced model is consistent in the results for various C/LT ratios, stacking sequences, and various kinds of geometries. Finally the model is tested on a portion of a Ferrari Formula One Front Wing and compared to the direct 3D solid model. Thus, in order to investigate the lack of precision of the analytical model in defining the through-the-thickness ILTS trend for the Front wing complex model, a specific loading case is tested. This loading case produces a particular deformation curvature and a double curvature in the through-the-thickness ILTS trend. Finally an alternative 3D postprocessing solution is proposed initially to check the analytical model performance, then as an alternative to the analytical model itself.

2. Composites materials

Composite materials have been extensively used in engineering design due to their remarkable performance / weight ratio, and possibility to tailor their structural behavior. As stated in [4] a composite material consist of “a strong and stiff component, ... , embedded in a softer and more compliant constituent”.

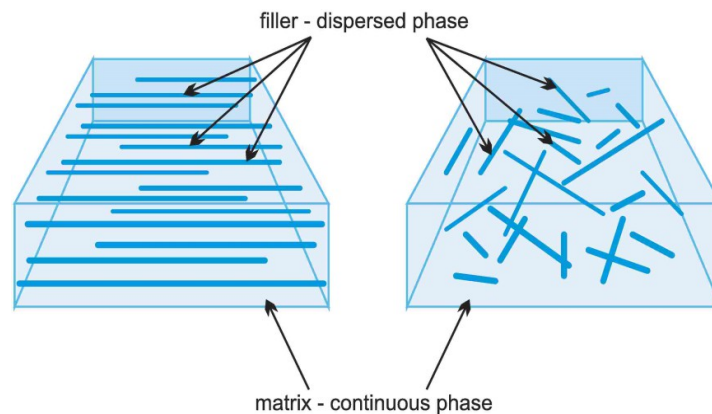


Figure 2.1. Example of fiber reinforced composite materials

Thus, composite materials can have highly anisotropic structural properties when the reinforcement is made of fibers. With no doubt, all the isotropic materials used in the industry show a certain degree of anisotropy due to the crystallographic texture which is not a constant during production. But composite materials exploit this feature that can be used to make high performance components [5]. The anisotropy is, on one hand, the strength of the composite materials because during the design process it can be used to optimize certain features of a component while, on the other hand, it exposes the component to issues (as for example manufacturing complexity) and type of damage that isotropic materials do not have. In this study, the principal composite material consists of resin matrix plus Carbon fiber reinforcement.

In general the pros of composite material can be summarized as:

- Anisotropic properties
- High strength-to-weight ratio (depending on Type of fiber)
- High stiffness-to-weight ratio (depending on Type of fiber)
- Low thermal expansion
- Low density
- Low thermal conductivity

While the cons are:

- Anisotropic properties
- Generally expensive
- Manufacturing complexity



Figure 2.2. Example of fiber reinforced composite materials

3. Damage in composite materials

During the design process of every sort of structural component, a special focus is given to the strength of the structure. Strength is intended as the capacity of the structure to handle the loads at which is designed and also some unpredictable extra.

The complexity of the composite components in terms of heterogeneity of micro structure and large difference between constituent parts, which induces the anisotropy of structural properties, is, on one hand, their big advantage and on the other hand, can cause many strength difficulties. The composite materials are affected not only by the “conventional” type of damage and failures, usually present in isotropic materials, but also have some peculiarities due to their micromechanics structure. Reporting this feature to the design process has as a consequence that a stress analysis is not as simple as for the isotropic materials. Moreover, the behavior of a composite component under loading can change after damage incurred during service in less predictable way respect to isotropic materials. The main damage mechanisms that can happen on a composite component can be summarized as:

- Interfacial debonding
- Intralaminar cracking
- Interfacial sliding
- Interlaminar cracking
- Fiber breakage and fiber microbuckling

3.1 Interfacial debonding:

In fiber composite materials, the interfaces are present between fiber and matrix. The stress/ load transfer happens through all these interfaces. The general properties of the composite materials are highly influenced by the interface properties between fiber and matrix resin. Indeed a micromechanical aspect as the adhesion at the inter-facial surface between the constituents of the composite material affects the macroscopic mechanical

properties in terms of stiffness and strength. Moreover, if the fibers are not well bonded to the matrix, the composite can start to form a crack at relatively low stresses. As the load is applied, the fiber and the matrix deform differently, when the shear stress developed at the interface exceeds the shear strength, a debonding along the fiber direction occurs.



Figure 3.1 . Debonds in a fiber- reinforced composite. From Compos Sci Technol, Vol 59, E.K. Gamsted and B.A. Sjorgren, Micromechanisms in tension-compression fatigue of composite laminates containing transverse plies, pp. 167-78, copyright Elsevier (1999).

3.2 Matrix microcracking / Intralaminar cracking

The composite materials, when fiber reinforced, present high stiffness and strength properties along the fiber direction. Because the fiber can hold the major part of the load. On the contrary, their properties are lower in the transverse direction and so is easier to develop a crack onto that direction. The cracks can form starting from defects like voids and inclusions or even interfacial debonding and run parallel to the fiber of a ply through the matrix. The matrix cracking does not cause an irreversible structural failure by itself, but it can result in an important stiffness penalty and can induce more severe damages as delamination and fiber breakage, plus it becomes an easy path for fluids to enter into the laminate.

3.3 Interfacial sliding

The interfacial sliding happens between the constituents of a composite material when there's a differential displacement of them. When the matrix and the fibers are not well bonded together but by a shrink-fit mechanism, the interfacial sliding could be easier to be activated. Instead, when the matrix is bonded to the fibers, the interfacial sliding can occur when there's the presence of an interface debonding. Than interfacial sliding can couple with the matrix cracking causing interactive effects on the composite delamination.

3.4 Delamination / Interlaminar Cracking

The interlaminar cracking is represented by a crack in the interfacial plane between two adjacent plies in a laminate. It can cause the separation of the plies and that is why is also called delamination. The development of an interlaminar crack leads to a deterioration of the mechanical properties because it can reduce the role of strong fibers and make the matrix properties govern the structural strength and stiffness. The critical property in initiating a delamination is the interlaminar strength that is mostly determined by the matrix. In Fig. 2 are represented the three most common loading conditions with respect to two adjacent plies that can trigger a delamination. These are the Interlaminar tension, and the interlaminar shear along the two principal directions: sliding shear and scissoring shear. The combination of these three interlaminar loading conditions is not always linearly an amplification factor for the interlaminar cracking. Indeed, a study conducted by Wisnom et al. [6] showed that an onset can resist more to the delamination when both tensile and shear interlaminar loads are applied, this feature is caused by a size effect that influences the volume affected by tensile interlaminar stress.

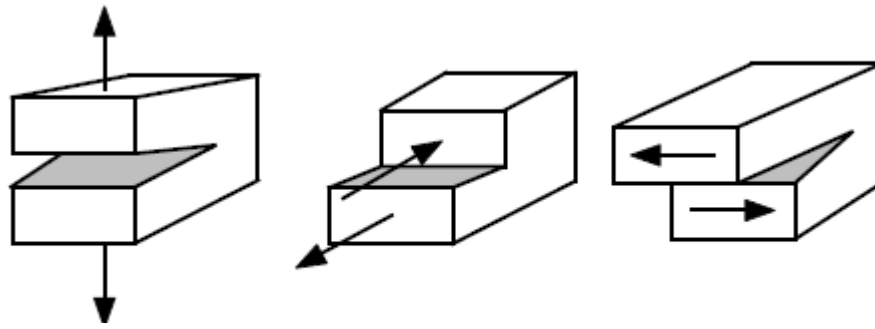


Figure 3.2. Interlaminar modes. On the Left the interlaminar mode I: Tension Mode. In the middle the Interlaminar mode II: Siding shear Mode. On the right the interlaminar mode III: Scissoring shear Mode.

3.5 Fiber breakage

The ultimate failure of a fiber composite component comes from the breakage of the fibers. The interface between fiber and matrix transfers the load along the component. When the load exceeds the strength of the fibers, they break and the load is redistributed along all the rest of the fibers that were less loaded, with the possibility to start the breaking process on all the fibers. The fiber breakage process has a statistic behavior because of the non uniformity of fibers strength among all the fibers, within the fiber itself, and also because of the stress redistribution.

3.6 Void growth and manufacturing defects

In composite materials, more than metals, it is likely to have manufacturing induced defects. These defects could be in the fiber architecture, for example, a fiber misalignment or an irregular distribution in the cross section, or fibers that are already broken; could be in the matrix, for example, voids or excess or lack of resin; could be at the interface between fiber and matrix or plies, such as debonding or delaminations. Also, a manufacturing defect could be induced by machining the components for

fasteners holes or design cutouts. The voids are virtually found in all types of composite materials. The formation of a void is induced by manufacturing parameters as vacuum pressure, cure temperature and cure pressure and also depends on resin viscosity. The presence of voids has as a consequence a decreasing effect on all material properties. The bending, transverse and shear properties are the most affected ones.

4. Delamination and Interlaminar Stresses

The delaminations are one of the most common damage type for composite components. Delamination happens when the separating stress between plies (interlaminar tensile stress ILTS) is larger than its bonding strength (typically the Resin bonding strength). Moreover, the bonding strength between plies is usually one order smaller than the in-plane strength.

The principal effect of delamination is the stiffness and strength loss, local stress concentrations, local instability under compressive loads. Under tensile loading, the presence of delamination promotes a drop of strength but its size does not significantly influence the value of the tensile strength [7]. The bending properties are impacted by delaminations [8] mainly due to alterations in shear stress profiles [9].

Typical delamination triggers are:

- Free edges
- Holes and exposed surfaces through the thickness
- Low velocity impacts
- Matrix cracks
- Out of plane joints
- Stress concentrations due to ply drop-off or thick laminate with high geometric curvatures

4.1 Free edges

The composite components are designed to face in plane loads, due to their anisotropic material properties. But even as a consequence of in plane load, a through-the-thickness normal and shear stress can be particularly concentrated at the traction-free surface in a composite laminate. These concentrations of stresses occur because of the mismatch of mechanical properties such as Poisson's ratio between the composite layers [10].

Indeed, considering two layers of a lamina with different fiber orientation, under axial tension, if they are not bonded together, there would be different axial deformation due to different Poisson ratios. But if these layers are tied together, into the laminate, under axial tension, they must have the same axial strain. Such stress and strain state is achieved by the interlaminar shear stress component. In Fig. 4.1 are represented the stress components acting on two layers (A and B) of a laminate at a free edge. The layers have different fiber angle. The axial stress is indicated with σ_y and the interlaminar shear stress with τ_{yz} while the interlaminar tensile stress with σ_z .

Analyzing the layer A near a free edge, it follows that interlaminar shear component τ_{yz} is balanced with axial stress σ_y . But, in order to satisfy the equilibrium of moments in the "YZ" plane, the distribution of normal stress σ_z must be such that there is no resultant force in the z direction [11].

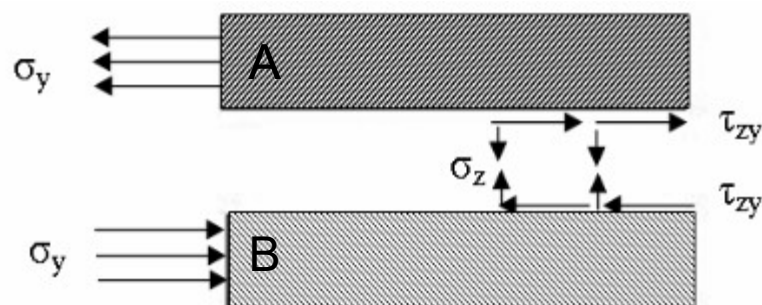


Figure 4.1. Particle of laminate, layer A and B have different fiber orientation

Herakovic [12] found that laminates with angled plies ($\pm\theta$) adjacent to each other develop higher interlaminar shear stresses at free edges. Moreover, he showed that interspersing ± 45 degree layers reduces the interlaminar tensile stress at the free edges. Even if there are two adjacent plies with the same orientation is not certain that delamination will not happen. Indeed, if there are some plies in a different direction in the neighborhood of the ones taken into account, there will be an interface moment caused by the neighborhood plies anyway [13]. Another parameter that influences the interlaminar stresses is the ply thickness, indeed the thicker plies tend to encourage higher interlaminar stresses at free edges.

4.2 Holes and exposed surfaces through-the-thickness

Most of the structures made by composite material contain holes for design reasons, such as bolted or riveted joints for fastening the composite structure with other components, or also manufacturing reasons. The holes are usually machined after lamination and cure processes. The occurrence of delamination during machining depends on the condition of the tool, the fiber cutting angle on the top laminate layers [14], the critical tangential cutting force at which peel-up and the critical thrust force at which push-out occurs. The drilling-induced delamination damage usually occurs at the hole entry and hole exit [15].

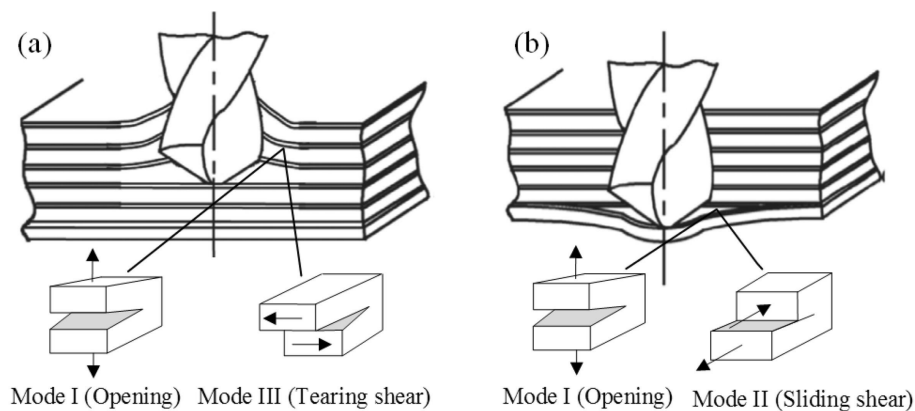


Figure 4.2. Mechanism of drilling induced delamination. (a) peel-up delamination. (b) push-out delamination [15]

The holes not only act as principal stress concentration but acting on shear stress distribution plays an important role on delamination initiation [16]. Moreover, holes contain free edges themselves because of the way they are made.

4.3 Low velocity impacts

Under an impact loading condition, there is a very localized area affected by a high deformation gradient. This causes shear and normal stresses that can cause delamination. Moreover, the high compressive load on the front surface means high tensile stresses on the back surface that can cause damages at the first weak point of the laminate. The laminate could develop high interlaminar shear stresses and delamination or bending failure (Fig. 4.3) depending on its constraint, if it can be represented by a short beam or a long beam respectively. To be mentioned the behavior under high velocity impacts, the laminate acts as rigid and the result is a shear out of the projectile [17].

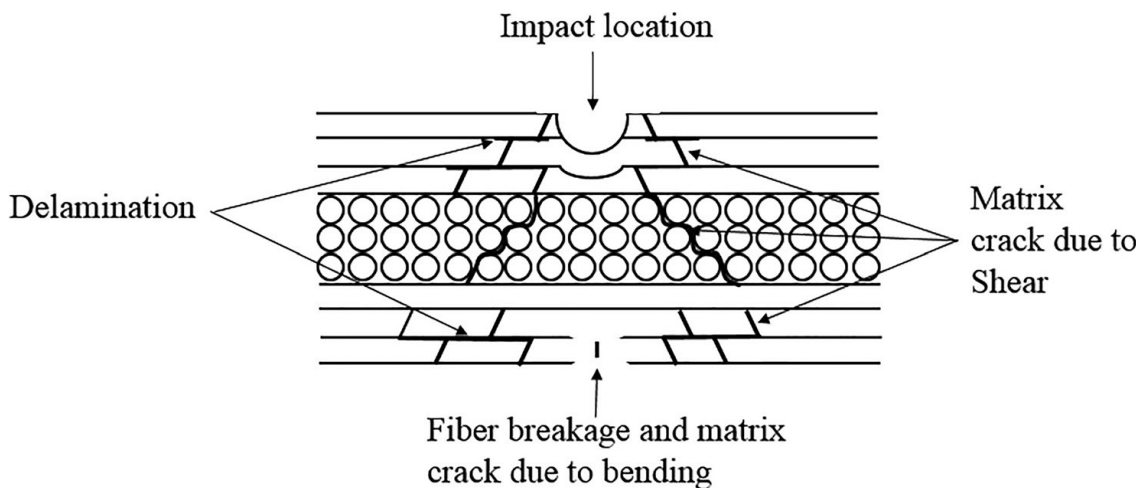


Figure 4.3. Impact damage mode of composite material

4.4 Matrix cracks

The matrix microcracking, as already said, can grow through the ply ending on the interface between plies and became a crack that separates them causing delamination (see Fig 4.4). There usually is a critical crack density that is a function of the composite structure and the material properties after that the laminate starts to develop delaminations [18]. Furthermore, these cracks act as stress concentrators because they are weak points in the load paths. Wang and Karihaloo [19] showed that the stress concentration is higher when there is a different angle ply of 90 degrees between plies and minimum with different angle ply of 40 degrees.

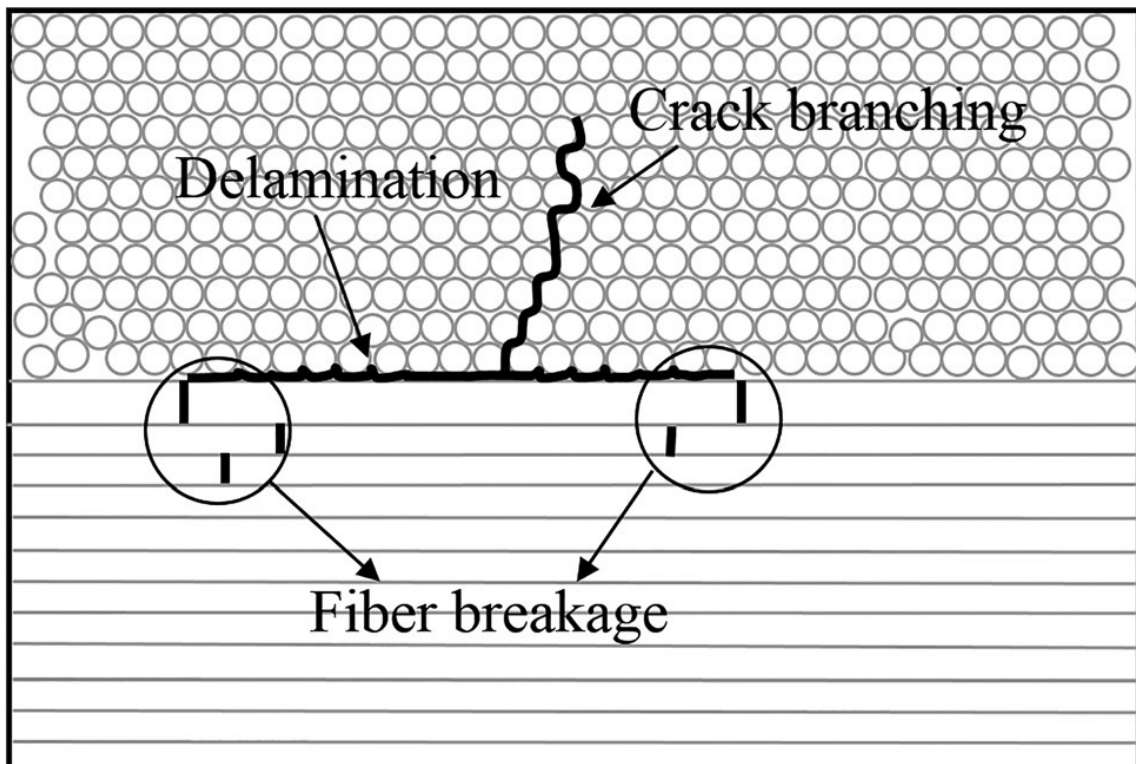


Figure 4.4. Delamination at the layers interface due to matrix crack

4.5 Out of plane joints

The components made by fiber reinforced plastic usually by design and production constraint have the necessity to have a certain number of joints of two different typologies: in-plane joints and out-of-plane joints. Typical out-of-plane joints are the tee ones (see Fig 4.5). The function of an out-of-plane joint is to transmit flexural, shear and tensile load between two orthogonal sets of panels. The regions that are most susceptible to delamination damages are the curved regions of the joint's root [20] [21]. Also, due to their particular mechanism of load transfer, these joints are prone to cause interlaminar tensile stresses on the main laminate where they are bonded/ fixed/ jointed.

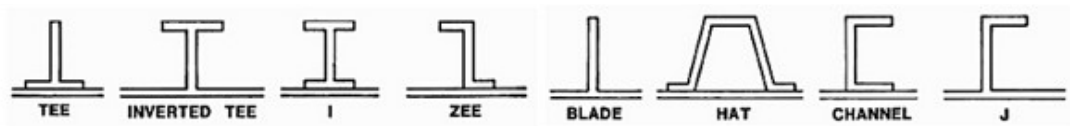


Figure 4.5. Different typology of out of plane joint in fiber composite component. From Delamination damage analysis of curved composites subjected to compressive load using cohesive zone modelling, Raju Raju (2014). Conference: First world Conference on Fracture and Damage Mechanics (FRACTURE-2014) At: Kottayam, India

5. State of the art

The delamination issue has been studied since the composite components have been part of the avant-garde of engineering design. The capacity to predict or at least provide a warning about a delamination issue has been the center of multiple tests and studies that develops in different branches of support for the design process.

The most direct criteria to check if a delamination is developing is expressed by [22]

$$\sigma_{zz} \geq T \quad \text{Eq. 5.1}$$

Defining x and y as the plane of the lamina, z represents its thickness direction; thus, σ_{zz} is the ILTS and T the tensile strength between the layers. While a more complete secondary stress criteria have been developed by [23] and is expressed by the equations:

$$\frac{\sigma_{zz}}{T} + \frac{\tau_{xz}^2}{S^2} + \frac{\tau_{yz}^2}{S^2} \geq 1 \quad \text{For ILTS} > 0 \quad \text{Eq. 5.2}$$

$$\frac{\tau_{xz}^2}{S^2} + \frac{\tau_{yz}^2}{S^2} \geq 1 \quad \text{For ILTS} < 0 \quad \text{Eq. 5.3}$$

Where τ_{xz} and τ_{yz} are the Interlaminar shear stresses (ILSS) and S is the in-plane shear strength .

Here is an overview of what has been developed to help the design and dimensioning of fiber composite components.

The principal branches are:

- analytical methods
- numerical methods
- experimental test

5.1 Analytical methods

A simple technique to analyze symmetric laminates under tension or compression based on assumed stress distributions using the principle of minimum complementary energy and the force balance method was presented by Kassapoglou and Lagace [24]. Later Kassapoglou [25] generalized this approach for general unsymmetric laminates under combined in-plane and out-of-plane (moment and shear) loads. The formulation, although accurate for homogeneously anisotropic plates, does not adequately model the mismatches in Poisson's ratios and the coefficients of mutual influence that exist between different plies in the through thickness direction.

Lu and Liu [26] developed an Interlaminar Shear Stress Continuity Theory (ISSCT). Using this theory it could be possible to determine Interlaminar shear stress directly from the constitutive equations. The only weakness is that the interlaminar normal stress could not be determined due to the fact that this theory neglects the deformation through the thickness. They developed in continuation of ISSCT a so-called Interlayer Shear Slip Theory. In this theory, they used Hermite cubic shape functions as the interpolation function for composite layer assembly in the thickness direction. From the results it was assessed that this theory could satisfy the continuity of both interlaminar shear and normal stress at the composite interfaces.

Wang and Li [27] used 3D anisotropic elasticity and the method of separation of variables to derive the equilibrium equations with unknown displacements for each cylindrical lamina of a multilayered shell subjected to axisymmetrically distributed mechanical and thermal load with various end boundary conditions. Then making the displacements and stress expressions satisfy the boundary conditions at the interfaces of the plies, they were able to determine the interlaminar stresses exactly.

Connolly [28] obtained simplified equations for the determination of interlaminar normal stress based on the simplification of the more general solution provided by Kassapoglou [25]. The equation takes into account the influence of material properties and geometry on the maximum values of normal interlaminar stresses at layer interfaces. He [29] proposed a refined shear deformation laminated shell theory. In this theory, the assumption is that the transverse shear strain across two different layers are

linearly dependent on each other. However, this theory can be applied only to shell which thickness is small compared to principal geometric curvature radius.

In “Calculating 3D stresses in layered composite plates and shells” Rohwer and Rolfes [30] used equilibrium conditions to calculate the transverse stresses *a posteriori* but not on curved shells. The main issue with these analytical methods is that they cannot be easily applied to curved shells. Matsunaga [31] based a method on the arch theory introducing a global higher order arch theory and using 3D equations of equilibrium to predict ILTS in circular arches. Because of the complexities, analytical solutions for the prediction of transverse/interlaminar stresses exist for composite laminates with simple geometry, loading and boundary conditions.

Anyway in the evaluation of transverse/interlaminar stresses, the stresses are most commonly obtained using post processing technique by integrating the equilibrium equations of 3D elasticity rather than using the constitutive relations, as the latter method leads to discontinuities of stresses at the interface of two adjacent layers of a laminate and thus violates the equilibrium equations.

5.2 Numerical methods

The disadvantage of the analytical methods consists of an inadequate local stress concentrations evaluation, indeed they are used mostly for simplified geometric cases. Also, these procedures become less practical when a multilayered laminate is involved in the evaluation. On the contrary numerical methods can have the possibility to refine the mesh near relevant regions and can evaluate with dequate accuracy complex geometries of multilayered composite components. Numerical methods require the discretization of a component usually through finite elements. The main numerical approaches are :

1. 2D shell and plates
2. 3D elements
3. enriched shells
4. Virtual Crack Closure Technique (VCCT) and Cohesive Zone Method (CZM)

5.2.1 2D shell and plates

The Finite Elements models of composite components usually consist of 2D elements as plates and shells elements or can be discretized with 3D elements. Because of complexities involved in the solution of three-dimensional equations of elasticity various technical theories have been developed by making suitable assumptions concerning the kinematics of deformation or stress state throughout the thickness of the laminate. These assumptions allow the reduction of a three-dimensional problem to a two-dimensional problem.

The 2D elements can be modeled as an Equivalent Single Layer (ESL) as the classical laminate theory (CLT), or a first order shear deformation theory (FSDT), but also with layerwise models (LWM) and individual layer plate theory (ILP). In the CLT there are many simplifications/ assumptions as the plane stress used to simplify the stress-strain relations, or the normal of the middle plane of the laminate assumed to remain straight when the element is deformed. The consequence of this assumption is that the plate or shell normal is not deformed and no transverse shear strain is taken into account. Consequentially the shear stiffness of the element is overestimated with respect to the actual component. This error is called shear locking and tends to give bending displacements results that are smaller than they should be. These features of the CLT are representing the Kirchoff hypothesis for plates and also the Kirchoff-Love hypothesis for shells [32]. Furthermore, many theories including the shear effects are developed, indeed Whitney and Pagano [33] studied a First-order Shear Deformation Theory (FSDT) for multi-layered anisotropic plates.

The FSDT can avoid shear locking effect by using reduced integration, and can calculate in very good agreement with 3D models the Interlaminar shear stresses but it is not able to predict interlaminar normal stresses because it still cannot take into account the warping of the cross section.

The exact analyses performed by Pagano [33] on the composite plates have indicated that the in-plane distortion of the deformed normal depends not only on the laminate thickness, but also on the orientation and the degree of orthotropy of the individual layers. Therefore, the hypothesis of non-deformable normals, while acceptable for isotropic plates and shells, is often quite unacceptable for multi-layered anisotropic

plates and shells that have a large ratio of Young's modulus to shear modulus, even if they are relatively thin.

Moreover, Whitney [34] showed that the shear deformation can significantly affect gross plate response for highly anisotropic laminates. Reddy [35] developed a higher-order shear deformation theory of laminated composite. The theory contains the same dependent unknowns as in the first-order shear deformation theory of Whitney and Pagano [33], but accounts for a parabolic distribution of the transverse shear strains through the thickness of the plate. This theory predicts the deflections and stresses more accurately when compared to the first-order theory.

While according to Auricchio and Sacco [36] the shear stress profile is represented either by independent piece-wise quadratic functions in the thickness or by satisfying the three-dimensional equilibrium equations written in terms of midplane strains and curvatures. Another theory that is based on FSDT is presented by Rolfes and Rohwer and Ballerstaedt [37] In this study the magnitude of the transverse shear stresses is determined from the transverse shear forces which are calculated from the material law. Also Nosier and Bahrami [38] presented an analysis based on the first-order shear deformation theory (FSDT) and then Robbins and Reddy layerwise theory (LWT) [39] is used to investigate the edge-effect interlaminar stresses. The CLT and First-order shear deformation theory (FOST) generally provide an acceptable compromise between accuracy and economy in predicting the global responses of thin and also relatively thin composite laminates. But these theories fail to give accurate results for the through-the-thickness stress response in regions of discontinuity such as cut-outs, holes, and boundaries.

Moreover, these theories require shear correction coefficients to rectify unrealistic variations of the shear strain/stress through the thickness. Hossain and Sinha and Sheikh [40] adopted the Mixed Interpolation of Tensorial Components (MITC) approach to overcome the effects of shear and membrane locking on the predicted structural response composite shell problems. The least-square weighted residual method is applied for the solution of out-of-plane differential equilibrium equations. The LWM and ILP differ from ESLs models by making displacement assumptions for every layer. Obviously, they can provide more accurate results in terms of displacements and strain fields but are extremely more complicated to implement. The difference between LWM and ILP consists in an a priori enforced continuity of the

interlaminar shear and normal stresses. Williams [41] proposed a mixed approach where ESL and LWM coexist in the same framework. A review of earlier shell finite elements which as been developed is given by [42] .

An eight-noded quadrilateral plate element with five Degrees of freedom (DoF) at each of the midside and corner nodes was formulated by Hamdallah and Engblom [43] . The plate element developed includes shear effects. To analyze 3D structures, they introduced a sixth DoF to represent rotations normal to the plane of the element. They used the equilibrium equations for calculating the transverse stresses. An interlaminar stress mixed finite element method based on the local higher-order lamination theory was presented by Wu and Kuo [44] to analyze thick symmetric laminated composite plates. In their theory, the displacement continuity at the interface between layers is introduced into the potential energy functional of the considered laminates using Lagrange multipliers and these Lagrange multipliers are defined to be the interlaminar stresses (shear and normal ones) at the interface between layers. Later Wu and Yen [45] extended the same formulation to analyze unsymmetrically laminated composite plates. While Tanov and Tabiei [46] presented an approach to account for the transverse normal stress distribution through a layered shell thickness. Tornabene [42] [47] adopted the First-order Shear Deformation Theory. The generalized strains and stress resultants are evaluated by applying the Differential Quadrature rule to the generalized displacements themselves. The transverse shear and normal stress profiles through the laminate thickness are reconstructed a posteriori by simply using local three-dimensional equilibrium equations. No preliminary recovery or regularization procedure on the extensional and flexural strain fields is needed when the Differential Quadrature technique is used.

5.2.2 3D elements

3D theories, in which each layer is treated as a homogeneous anisotropic material, predicts the 3D stress state at the boundaries more accurately than CLT and FOST, but their storage requirements due to a large number of variables and computer costs make them impracticable.

Kim and Hong [48] used a 16 noded curved isoparametric element without a midside node in the thickness direction and 48 Degrees of freedom (DoF). Davila and Johnson [49] studied the high interlaminar stress at dropped plies in laminates 3D FE models. Than Schiffer and Tagarielli [50] modeled the non-uniformity of the ILT strength by introducing discrete random fields of material parameters in the simulation. They showed there's a statistical toughening effect due to random material properties because of difficult crack patterns.

5.2.3 Shell/3D elements

For many applications, a full 3D finite element analysis is not cost effective as it needs large computer core storage and running times in comparison with 2D finite element analysis. Thus, a 2D/3D global/local finite element method can drastically improve the efficiency of computerized analysis and provide sizable savings by circumventing the need to perform expensive analyses near critical regions.

Krueger and O'Brien [51] developed a shell/3D modeling technique for which a local three-dimensional solid finite element model is used only in the immediate vicinity of the delamination front. The shell/3D modeling technique offers great potential for reducing the model size because only a relatively small section in the vicinity of the delamination front needs to be modeled with solid elements. Then Krueger and Minguet [52] combined a shell/3D modeling technique with the virtual crack closure technique (VCCT).

5.3 Failure Criteria: VCCT and CZM

There are some methods used to predict with a certain accuracy composite laminate failure due to interlaminar tension and shear stresses at discontinuities. The failure criteria are based on interlaminar fracture mechanics and the calculation of the total

strain energy release rate, GT , the mode I component due to interlaminar tension, GI , the mode II component due to interlaminar sliding shear, GII , and the mode III component, $GIII$, due to interlaminar scissoring shear. These calculated G components are compared to interlaminar fracture toughness properties measured over a range from pure mode I loading to pure mode II loading.

The virtual crack closure technique (VCCT) is widely used for computing energy release rates based on results from continuum (2D) and solid (3D) finite element analyses to supply the mode separation required when using the mixed-mode fracture criterion. To apply VCCT to a finite element model, a crack or delamination has to be included in the model as a discrete discontinuity “when a crack extends for a small amount, the energy it takes to open the crack equals the energy it takes to close the crack” Krueger [53].

Krueger [53] gives an overview of the virtual crack closure technique and provides an

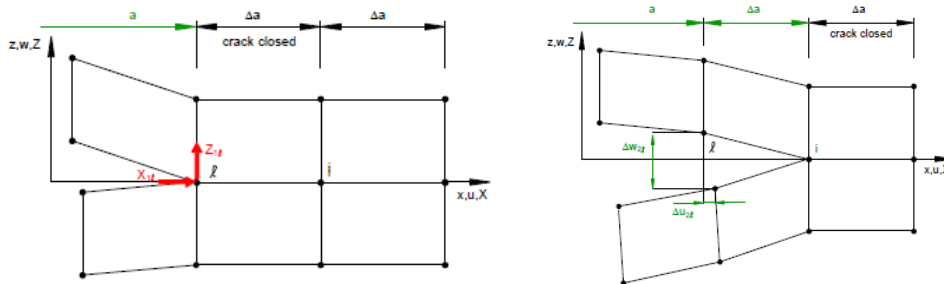


Figure 5.1. VCCT working principle

insight into its application. Later he [54] presented necessary modifications for the use of the method with geometrically nonlinear finite element analysis and corrections required for elements at the crack tip with different lengths and widths. The only negative feature of the VCCT is that it cannot predict the crack initiation, but it can be used with some stress-based criteria to predict it. Pietropaoli and Riccio [55] proposed a methodology, implemented in ANSYS © as post-processing routines, combined with a finite element model, using both shell and solid elements.

Tay et al [56] made a comparison between 2D and 3D FE analyses of delamination growth in post buckling, the virtual crack closure technique (VCCT) and crack closure technique (CCT) have been used in the paper. A method based on Virtual crack closure technique and on an extended layerwise method is proposed by Li [57] to predict the

delamination and transverse crack growth of laminated composite plates and shells.

The cohesive zone method (CZM) introduces a fracture mechanism in the analysis by relying on softening relationships between traction and separation. The interfaces of the different materials can be represented by special elements (interface elements or contact elements). The formulation of a cohesive element for shell analysis can be used to simulate the initiation and growth of delaminations. There are basically two types of cohesive law:

- *An intrinsic cohesive law*: Need to know “a priori” the extension of the cohesive zone
- *An extrinsic cohesive law*: No need to know anything “a priori” but has a too high computational effort

Dàvila [58] proposed cohesive element for shells that can be used to represent the propagation of a pre-existing delamination, as well as the onset and propagation of delamination in components that do not contain pre-existing cracks. While Li [59] proposed a 8-node interface element made by 8 rigid bars plus 8 zero thickness cohesive elements. Another application of the CZM was investigated by Soroush [60] using the commercial finite element code ABAQUS on a structure subjected to low-velocity impact. The procedure is based on cohesive zone elements and surfaces plus a progressive damage model. The procedure that is proposed could be used as a benchmark method in damage modeling of composite structures under high velocity impact. Mikulik [61] showed a comparison on FE model made by shells and cohesive elements between the VCTT and the crack tip element methodology proposed by Davidson [62]. Ye et al [63] proposed a micromechanical model to predict the cohesive strength of many laminates at various fiber cross-angles. They aimed to use predicted cohesive strength instead of interlaminar strength. And Camanho [64] proposed a mixed-mode decohesion element used at the interface between solid finite elements. Wisnom [65] applied cohesive zone interface elements with 3D FE models studying the effect of dropped plies in composite laminates.

Gliszczynski [66] presented a comparison between VCCT and CZM highlighting the main features of the CZM that can overcome the VCCT as : the possibility of applying the method for coarse meshes; convergence of results achieved for both two- and three-dimensional models; significantly shorter CPU time; no need of the initial delamination front assumption.

5.4 X-FEM and enriched shells

The finite element method (FEM) has been widely used for the linear elastic fracture analysis of layered structures. However, accurate solutions by the conventional FEM is computationally expensive since the mesh must conform to the geometry of the crack and a refinement in the area of the crack tip is generally required.

Shell element models are computationally efficient, and due to a simplified mesh when compared to a high-fidelity solid element approach, the models are inherently less expensive for an analyst to create and use. Layer-wise stacking is a common technique for using shell elements for laminate damage simulation. In such an approach, independent layers of shell elements are defined and connected across ply interfaces in a laminate. If delamination is placed at a specific ply interface of interest, a mesh may consist of two layers of shell elements, one on either side of the ply interface location. The two layers can be connected by rigid links and delamination growth can be simulated using the Virtual Crack Closure Technique.

An inherent disadvantage of the two-layer stacked shell models is that the delamination interface must be predefined, thereby limiting the model's utility as a general predictive tool. Furthermore, by restricting the delamination to a single ply interface location, multiple delaminations, or delamination and matrix crack interaction, is not possible. The eXtended Finite Element Method (XFEM) [67], introduces extra degrees of freedom (DoF) and enrichment functions to represent the displacement field in the neighborhood of a crack. The element interpolation functions are enriched to explicitly represent the displacement fields in the presence of discontinuities, each element is changed to a different formulation when a crack propagates within its domain.

The advantage of X-FEM is that the finite element mesh can be completely independent of the morphology of these entities.

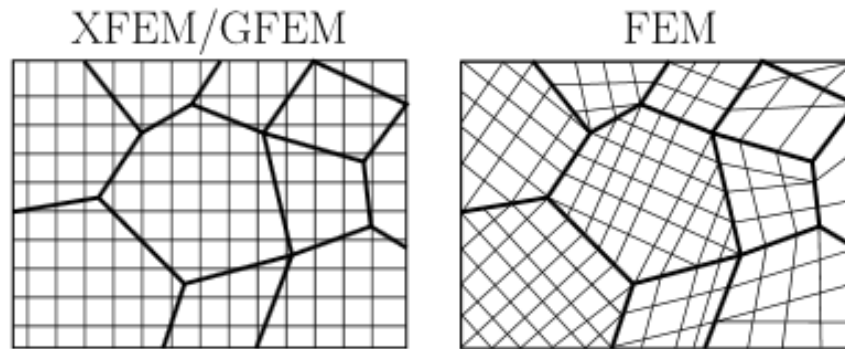


Figure 5.2 .Discretizations of a grain boundary problem for an XFEM/GFEM model with a structured mesh and a FEM model.

Furthermore, when certain aspects of the solution of the field are known, as for example the near tip displacement fields for cracks, enrichment functions based on these fields can be added to the approximation space. An accurate review of X-FEM methods has been proposed by Belytschko, Gracie and Ventura [68].

McElroy [69] [70] used an enriched shell element model to simulate delamination-migration in a composite laminate. The element enrichment allows for adaptive mesh fidelity through the thickness where a single element splits into two elements only as required locally to characterize an evolving delamination process [71]. At any location in the model where the damage does not occur, the original discretization remains unaffected and a single shell element is used to represent the entire laminate thickness as defined in the beginning of the analysis. Another approach is used by Medikonda and Tabiei [72] where thickness-stretch shell elements, which utilize a 3-D material model sub-routine, are used in conjunction with a stress-based approach. These elements are able to predict quite realistic delamination results along with the proposed micro-mechanical model for impact simulations considered. While Cardoso and Yoon [73] showed a shell element with an incorporated additional degree of freedom in order to obtain a linear variation of strain field along thickness direction.

Hansbo and Hansbo [74] proposed a phantom node method, the main feature is that the material domain with a potential internal discontinuity can be modeled by one element with two pairs of nodes, namely real nodes and ghost nodes. And if the stresses on the element reach the material allowable strength, a discontinuity is automatically modeled creating two duplicated elements with the help of the phantom nodes. Each of the two

elements contains only part of the material domain.

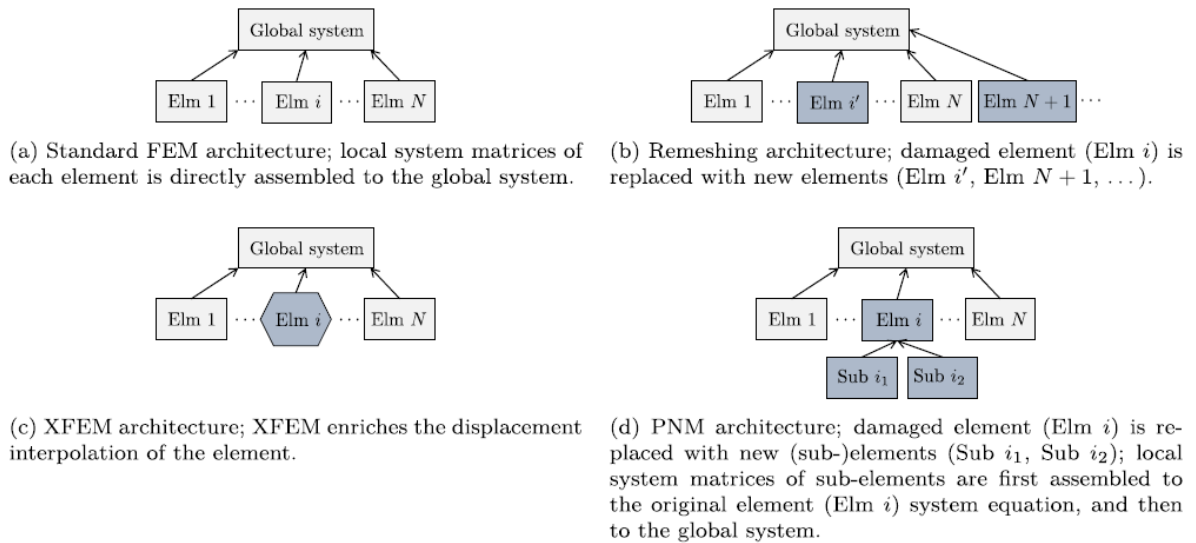


Figure 5.3. PNM work flow

Chen [75] proposed a Floating node method where the main difference with respect to the phantom node is that sub elements nodes could be anywhere in the element space, indeed nodes coordinates are directly the crack boundaries.

De Cicco and Taheri [76] presented x-Fem enriched element, and they also combined these elements with cohesive elements. The results are good when combined, they can predict also a change of delamination path. They stated that only x-FEM is not enough accurate, because it overestimates the energy rate. One of the most limiting feature is the big computational effort.

Demasi et al [77] presented the Generalized Unified Formulation extended to the case of Variable Angle Tow composite structures. This formulation gives the possibility of tailoring the theory/order to increase the accuracy in desired directions/ zones of a component.

5.6 Experimental tests

In order to predict the structural behavior of composite components the analyses have to be supplemented by experimental programs studying failure mechanisms and stress patterns. It is necessary that a correct assessment of delamination fracture toughness is made using some test methods.

The short beam shear test method is one of the main common tests employed for interlaminar composites material characterization. It is able to cause Interlaminar shear failures but not interlaminar tensile failure caused by peel stresses as stated by Davies et al. [78]. Wilkins et al. [79] proposed a double cantilever beam specimen to test mode I delamination. ASTM D 6415 [80] uses a curved-beam configuration for measuring interlaminar tensile strength. While ASTM D7291 / D7291M – 07 [71] sets tensile forces applied normal to the plane of the composite laminate using adhesively bonded thick metal end-tabs.

Then Charrier et al. [82] proposed a complete protocol to identify the out-of-plane tensile strength of specimens composed of unidirectional plies. The protocol is based on a four-point L-shape specimen bending test. Another interesting statement is that Interlaminar tensile strength is not dependent on the laminate sequence but highly dependent by laminate quality, indeed thick specimen with less quality because of manufacturing difficulties have less interlaminar tensile strength respect to a thin specimen. On the contrary Makeev et al. [83] suggested that ASTM D 6415 is not adequate to measure interlaminar tensile strength because manufacturing process to produce curved-beam uniform coupons could be challenging and the results may be coupon related. They tried to couple short beam specimen with digital image correlation to measure ILTS.

Jackson and Martin [84] proposed a technique to determine interlaminar tensile strength still based on a curved specimen (Fig.5.4), but with a different loading mechanism. Wisnom et al. [6] showed a special specimen for combined stress, the study showed that the size effect produced by the interlaminar shear stress has a positive effect on the interlaminar tensile stress due to the smaller volume where the load is applied. Size effect were also studied by Wisnom and Atkinson [85] developing a tapered tensile test

specimen to produce failure away from the grips. The size effect was observed by the decrease in terms of strength of the failure strain with increasing specimen size. Bosia et al. [86] compared experimental tests and numerical analyses. They showed that experimental results agree with 3D numerical simulations and don't agree with 2D ESL shell elements.

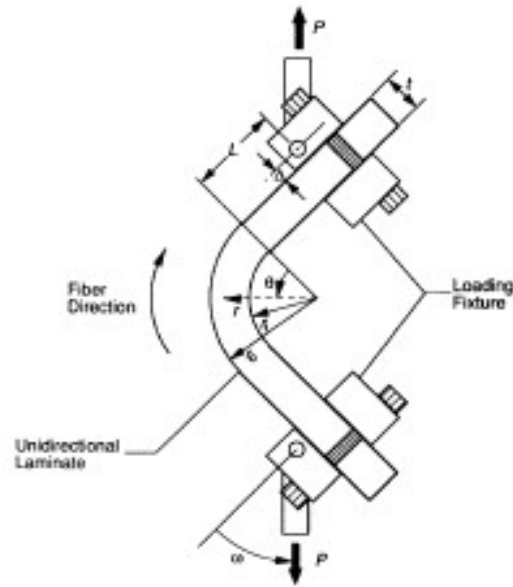


Figure 5.4. curved specimen subjected to tensile loading to induce ILT stress into the laminate. From Jackson and Martin [84]

6. Post processing analytical model implementation

The present chapter describes the necessary steps for deriving the interlaminar normal stresses from the results of a customary FE analysis based on four noded quadrilateral shell elements; a forced migration to different element technologies has in fact been evaluated as not viable, especially in the case of complex assemblies.

Paragraph 6.1 describes the retrieval of the shell local curvatures at each element; in order to avoid the analysis of the element neighborhood topology - a single, isolated four noded element lacks in fact of proper curvature representation - a method is proposed based on the provision of eight-noded counterparts for the element subjected to ILTS analysis; such a second order mesh may be straightforwardly derived by modern geometry-aware preprocessors.

Paragraph 6.2 describes the radial equilibrium of a doubly curved laminate angular section, which is satisfied only in the presence of normal stress distribution (named ILTS where tensile), which is usually neglected in the flat laminate model employed in formulating the four-noded quadrilateral element.

Paragraph 6.3 casts such an equilibrium relation in a second order differential equation, and it describes a finite-difference solution method which allows the evaluation of the ILTS as a function of the element geometric and load-induced curvatures.

Paragraph 6.4 completes the picture with a brief digression which quantifies the inconsistency between the curvature-unaware laminate theory, based on which the global structure response is predicted, and the curvature-aware formulation introduced in Paragraph 6.2 and employed in deriving the ILTS.

Paragraph 6.5 explores the main variables that influence the ILTS magnitude in curved laminate members, consisting in particular in the geometric (initial) curvature, and the level of orthotropy.

Paragraph 6.6 details the actual implementation of the postprocessing method, describing the quantities employed in the Matlab code, and some relevant technicalities.

6.1 Geometric curvature radii estimation techniques

The geometric curvature radius is calculated on the undeformed shape of the model. There are many ways to obtain data about the geometry geometric curvature; the easiest ones are: by extracting data about the curvature from a quadratic 6 or 8 nodes shell element, or, by evaluating the curvature radius considering linear shell elements and their adjacent neighborhoods. The quadratic shell element has the vantage to map curved surfaces in a better way than the linear element and also, for isoparametric elements, the shape functions can describe the element geometry. Their use is usually limited by the high computational effort. The linear shell elements, instead, have not the possibility to evaluate the radii of a curved surface because there are only 2 nodes for each edge, consequentially the element's edges are always straight. Therefore, in case of linear shell elements, there's the need to involve also the elements adjacent to the reference one. Usually the adjacent elements share an edge with the reference element, the edge is represented by two consecutive nodes (which are the corner nodes of the element). In this postprocessing analytical model, quadratic shell elements are used to evaluate geometric curvature radii. This solution is more robust with respect to the use of adjacent linear elements because a too coarse mesh will end up in a misleading evaluation of the real geometric curvature radius. Indeed a peak of a parabolic surface could not be represented with good accuracy by linear elements because could happen that none of the element nodes are placed near the peak, so during the approximation it will be skipped. An 8node shell element instead can follow the geometry curvature in a better way.

The geometric curvature radii, both principal and secondary, and also the angle between the principal geometric curvature and the principal direction of the element are calculated for each quadratic element of the model to be analyzed.

The principal geometric curvature radius will be signed as $R1$ and the secondary with $R2$, and they are placed in the midsection of the 2D shell element. The sign of the geometric curvature Radii depends on the shell FE normal direction that is defined by the first three nodes with the right-hand rule. In general, the geometric curvature radius

R is defined positive if the curvature radius vector \vec{R} and element normal vector \vec{n} have the same direction.

$$\begin{aligned}
 R > 0, \text{ if } \vec{R} \cdot \vec{n} > 0 \\
 R < 0, \text{ in other cases}
 \end{aligned}
 \tag{Eq. 6.1}$$

The subsequent considerations are done on 4 nodes shell elements for clarity of description, moreover the 3 nodes shell elements are considered as degenerated 4 nodes shell elements with one of the 4 nodes collapsed.

The quadratic shell element nodes are organized as represented in the scheme in Fig. 6.1. The first 4 nodes (indicated in Fig. 6.1 with G1 to G4) are the ones defining also the linear version of the same element, so they are placed at the 4 corners of the element. The supplementary nodes (indicated in fig. 6.1 with G5 to G8) are the mid side ones created during the conversion from the linear elements (they are placed onto the geometry surface). The estimation of the geometric curvature Radii has an important role in the estimation of the ILTS with this post processing method and has to be as much precise as possible.

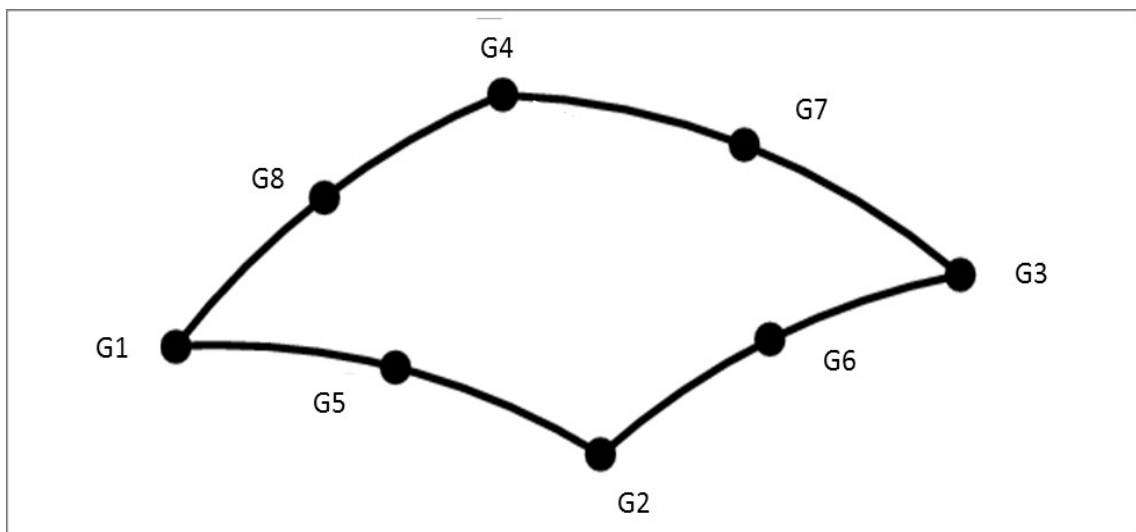


Figure 6.1. 8 nodes shell element definition

In [87] Kress proposes the geometric curvature radius as defined by

$$R = \frac{(1 + g''^2)^{1.5}}{g''} \quad \text{Eq. 6.2}$$

Where g is the representation of a surface and ' denotes the derivative of the function g , plus the assumption is that the reference surface follows a parabolic function.

In this study, two different methods were implemented to evaluate the geometric curvature radii. One method recalls the Barlow points and the projection of vectors on the principal planes. The other one follows the differential geometry of surfaces [88].

6.1.1 Geometric curvature Radii estimation: Projection on principal planes method

For each element the local Cartesian axis system ξ, η, ζ (see Fig. 6.2) is calculated. The ζ axis is oriented along the element normal while the ξ axis is oriented along the bisector to the diagonals d_{13} (diagonal between $G1$ - $G3$) and d_{24} (diagonal between $G2$ - $G4$).

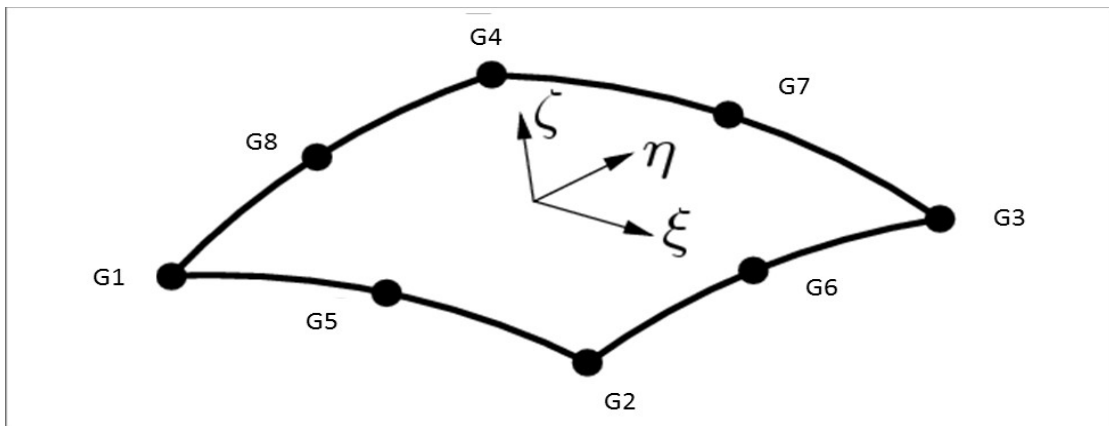


Figure 6.2. Local axis system

From nodes coordinate x, y, z , are calculated the two vectors associated with the diagonals, indicated with d_{13} and d_{24} . The local element ζ vector is perpendicular to the plane defined by the two diagonals and calculated with eq. 6.3

$$\zeta = d_{13} \times d_{42} \quad \text{Eq. 6.3}$$

Where the two diagonals are defined as:

$$\begin{aligned} d_{13} &= \overline{G3 - G1} \\ d_{42} &= \overline{G4 - G2} \end{aligned} \quad \text{Eq 6.4}$$

The local vectors ξ and η are defined by the bisectors of the diagonals. The two geometric curvature radii are calculated with respect to this local system evaluating the normal at the 4 Gauss integration points of the 2 X 2 integration scheme.

The centroid coordinates are evaluated with the quadratic elements shell shape functions. Furthermore, are defined the Barlow points coordinates.

$$\begin{aligned} \xi_i &: \left[-\frac{1}{\sqrt{3}}, \frac{1}{\sqrt{3}}, \frac{1}{\sqrt{3}}, -\frac{1}{\sqrt{3}} \right] \\ \eta_i &: \left[-\frac{1}{\sqrt{3}}, -\frac{1}{\sqrt{3}}, \frac{1}{\sqrt{3}}, \frac{1}{\sqrt{3}} \right] \end{aligned}$$

These are the isoparametric coordinates at the 4 Gauss points of the integrated quadratic element that give the best estimates of stress for an element. For triangle shell elements these are the full Gauss integration points while for quadrilateral shell elements are the reduced Gauss points.

Furthermore, the 8 parametric shape functions N_i (eq 6.5) of the quadratic isoparametric shell element and their derivatives respect to ξ and η are defined.

$$\begin{aligned} N_1 &= \frac{1}{4}(1-\xi)(1-\eta)(-\xi-\eta-1) \\ N_2 &= \frac{1}{4}(1+\xi)(1-\eta)(\xi-\eta-1) \\ N_3 &= \frac{1}{4}(1+\xi)(1+\eta)(\xi+\eta-1) \\ N_4 &= \frac{1}{4}(1-\xi)(1+\eta)(-\xi+\eta-1) \\ N_5 &= \frac{1}{2}(1-\xi^2)(1-\eta) \end{aligned} \quad \text{Eq 6.5}$$

$$N_6 = \frac{1}{2}(1+\xi)(1-\eta^2)$$

$$N_7 = \frac{1}{2}(1-\xi^2)(1+\eta)$$

$$N_8 = \frac{1}{2}(1-\xi)(1-\eta^2)$$

These shape functions are used to calculate integration points coordinates respect to the element centroid coordinates. They are multiplied by the distance of each Barlow point from the element centroid expressed in the global coordinate system of the FE model. Then these distances are projected on the local system axes to find the coordinates of the Barlow points. The shape function derivatives are used to calculate the directions, at each Barlow point, locally tangent to the element surface. The local normal ζ_i , which is the most relevant one, at each Barlow point is then calculated as vector product of the locally tangent vectors ξ_i, η_i (Fig. 6.3).

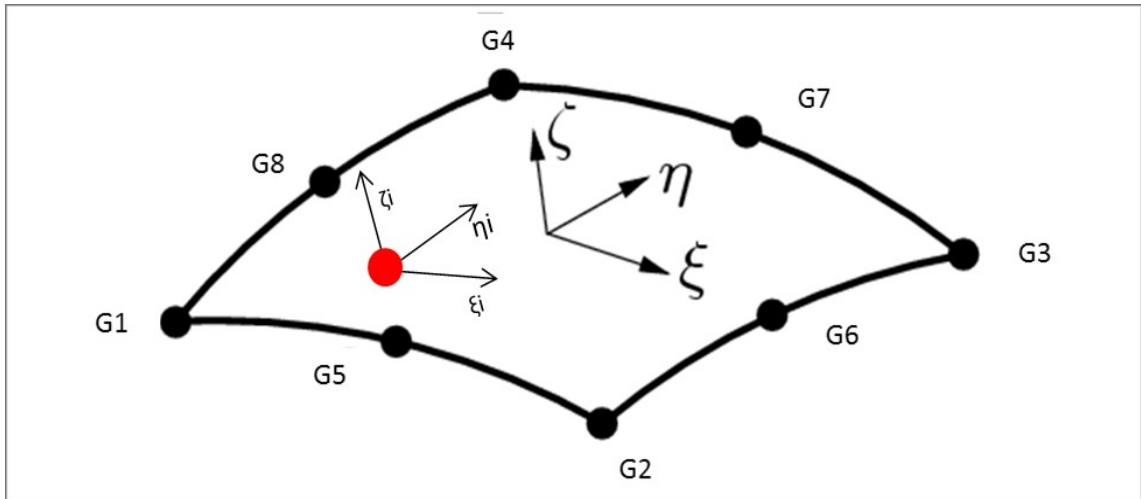


Figure 6.3. Local axis at Barlow point

The rotation angles are calculated between the local normal ζ_i of each Barlow point and the ζ axis of the element. The local normal vector ζ_i is projected on the ζ - η plane by removing its component along ξ axis creating an auxiliary vector $\zeta_{i-projected}$. Then is calculated the rotation angle Rx_i for each Barlow point along ξ respect to ζ using the relationship between \sin and the magnitude of the cross product eq 6.6.

$$Rx_i = \sin^{-1}((\zeta \times \zeta_{i-projected}) \cdot \xi) \quad \text{Eq. 6.6}$$

The same procedure is used to calculate the rotation angle Ry_i for each Barlow point projecting the local normal vector η_i on the plane ζ - ξ and using eq 6.6.

Finally is defined the curvature Cx as the first derivative of the function $R_x(\xi,\eta)$ along η , and Cy as the first derivative of the function $R_y(\xi,\eta)$ along ξ , and the mixed curvature Cxy as in eq 6.7

$$\begin{aligned} Cx &= \frac{\partial Ry(\xi, \eta)}{\partial \xi} \\ Cy &= -\frac{\partial Rx(\xi, \eta)}{\partial \eta} \\ Cxy &= \frac{\partial Ry(\xi, \eta)}{\partial \eta} - \frac{\partial Rx(\xi, \eta)}{\partial \xi} \end{aligned} \quad \text{Eq. 6.7}$$

Where the function $R_x(\xi,\eta)$ is a linear interpolation of the function angle R_x along ξ and η (eq 6.8). Same for function $R_y(\xi,\eta)$

$$\begin{aligned} Rx(\xi, \eta) &= \alpha_1 x + \alpha_2 y + \alpha_3 \\ Ry(\xi, \eta) &= \beta_1 x + \beta_2 y + \beta_3 \end{aligned} \quad \text{Eq. 6.8}$$

Where α and β are the coefficient vectors to be calculated, x and y are the Barlow points coordinates in the local system ξ, η, ζ . the coefficient vectors are calculated by resolving the system below:

$$(A) \times (\alpha) = [Rx]$$

Where matrix A is filled with vector x, y and a vector of ones

$$(A) = \begin{pmatrix} x & y & 1 \end{pmatrix}$$

The coefficient vectors α and β are calculated by resolving the system with a Moore-Penrose pseudoinverse matrix of the matrix A according to eq 6.9

$$\begin{aligned} \alpha &= \text{pseudinv}(A) \times [Rx] \\ \beta &= \text{pseudinv}(A) \times [Ry] \end{aligned} \quad \text{Eq. 6.9}$$

Finally eq 6.10 could be resolved

$$\begin{aligned} Cx &= \beta_1 \\ Cy &= -\alpha_2 \end{aligned} \quad \begin{array}{l} \text{Eq.} \\ 6.10 \end{array}$$

$$C_{xy} = \beta_2 - \alpha_1$$

The curvatures C_x , C_y and C_{xy} are then used to calculate the principal curvatures C_1 and C_2 (where $C_1 > C_2$) and γ is the angle between the principal curvature direction with respect to the principal direction of the element. Where C_1 , C_2 and γ are expressed by eq 6.11

$$\begin{aligned} C_1 &= \frac{1}{2} \left((C_x + C_y) + \sqrt{C_x^2 + C_y^2 - 2C_x C_y + 4C_{xy}^2} \right) \\ C_2 &= \frac{1}{2} \left((C_x + C_y) - \sqrt{C_x^2 + C_y^2 - 2C_x C_y + 4C_{xy}^2} \right) \\ \gamma &= \frac{1}{2} \text{atan2}(2C_{xy}, (C_x - C_y)) \end{aligned} \quad \text{Eq. 6.11}$$

From the principal curvatures, the geometric curvature radii R_1 and R_2 are calculated through the eq. 6.12. Where z_{offset} is the offset of the 2D shell element.

$$\begin{aligned} R_1 &= 1/C_1 + z_{offset} \\ R_2 &= 1/C_2 + z_{offset} \end{aligned} \quad \text{Eq. 6.12}$$

6.1.2 Geometric curvature Radii estimation: differential geometry surfaces method

The second method is based on differential geometry. Taking into account a generic point P on a surface (constituted by one element in this case as in Fig. 6.4), the vectors

ξ , η , ζ , are defined as:

$$\begin{aligned} \xi &= \partial P / \partial x \\ \eta &= \partial P / \partial y \\ \zeta &= \frac{\xi \times \eta}{\|\xi \times \eta\|} \end{aligned} \quad \text{Eq. 6.13}$$

Where x and y define the plane perpendicular to ζ .

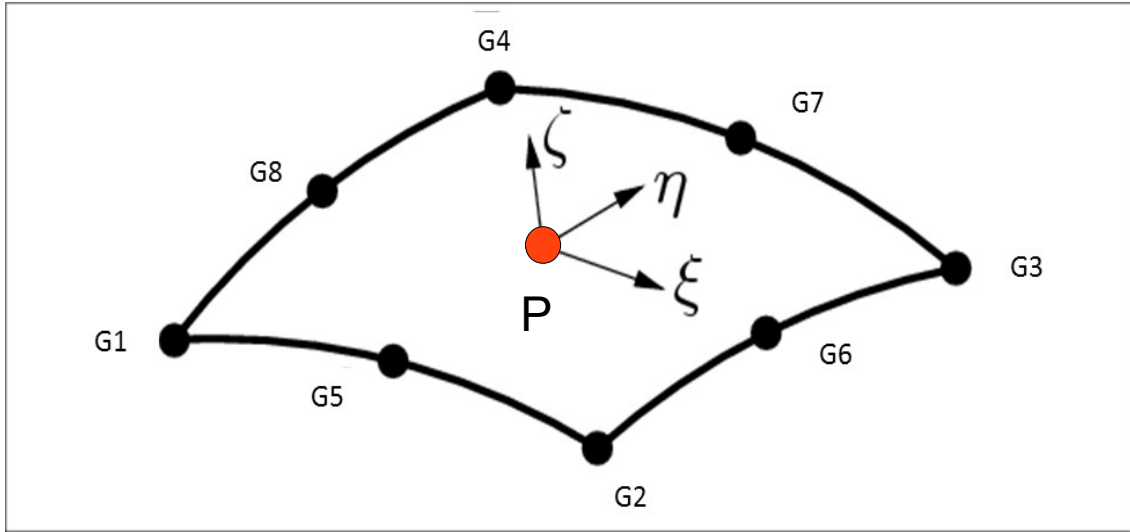


Figure 6.4. Local axis on generic point P on a surface

Then the shape of the surface is characterized by two structures: the first and the second fundamental forms. The first fundamental form is called also Metric form. It is possible to take measurements of the surface with this form as lengths or area or even angles between two curves laying on the surface. The first fundamental form I is defined as eq 6.14 and represents the arc element of a regular curve on the surface.

$$I = g_{11} dx^2 + 2g_{12} dx dy + g_{22} dy^2 \quad \text{Eq. 6.14}$$

Where $g_{ij} = P_i \cdot P_j$ ($i, j = 1, 2$) and the subscript represent the derivatives.

Therefore the first fundamental form is defined as the dot product of the infinitesimal displacement of a curve on the surface. While the second fundamental form II is defined as the dot product of dP and infinitesimal variation $d\zeta$ on the surface unit normal ζ . It can be expressed by eq. 6.15:

$$II = -dP \cdot d\zeta = h_{11} dx^2 + 2h_{12} dx dy + h_{22} dy^2 \quad \text{Eq. 6.15}$$

Where $h_{ij} = P_{ij} \cdot \zeta$ ($i, j = 1, 2$).

there's a family of planes containing the surface normal ζ at a generic point P, these

planes cut the surface generating a family of normal section curves C passing through the point P (in Fig. 6.5 a representation of one plane cutting the surface X)

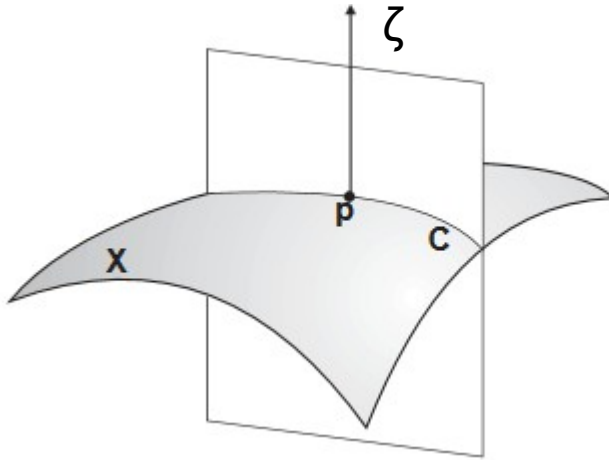


Figure 6.5. Surface cut by plane in P point

Assuming t to be the tangent vector of the normal section curve C at P . the curvature K of the surface is defined as the curvature of the normal section curve and can be calculated with differential equation $\zeta' = 0$ along C (eq 6.16)

$$K = -\frac{II}{I} = \frac{-(h_{11} + 2h_{12}\lambda + h_{22}\lambda^2)}{g_{11} + 2g_{12}\lambda + g_{22}\lambda^2} \quad \text{Eq. 6.16}$$

Where $\lambda = dy/dx$ specifies the direction of the curve.

The general rule is that at each point of the surface the curvature K varies together with each direction λ . The solution of this problem of eigenvalues and eigenvectors produces values of curvatures K and directions λ . The extreme values K_1 and K_2 are called principal curvature, they are linked to the roots λ_1 and λ_2 .

$$\det \begin{vmatrix} \lambda^2 & \lambda & 1 \\ g_{11} & g_{12} & g_{22} \\ h_{11} & h_{12} & h_{22} \end{vmatrix} = 0 \quad \text{Eq. 6.17}$$

Therefore K_1 represent the maximum curvature and K_2 the minimum, the directions λ_1 and λ_2 are always orthogonal. The only exception happen at umbilical points, where

$K_1=K_2$ and the principal directions are undefined. Finally can be calculated the angle between the maximum principal direction and the x direction of the element.

6.2.3 Geometric curvature Radii estimation: methods comparison

One of the first features to test about the model is the capability to catch the correct geometric curvature radius. It has to be able to calculate the radius in favorable conditions as a fine mesh aligned with the radius but also non favorable condition as coarse mesh not aligned with the geometric curvature radii.

The two methods to calculate the principal geometric curvature radii are tested firstly on a single geometric curvature then on a double geometric curvature FE model. One of the simplest tests is a single geometric curvature model composed by an arc of 5 mm Radius extruded by 10 mm. The geometry is meshed with different mesh sizes. In fig 6.6 the geometry is composed by a mean mesh size of 0.4 mm aligned with the geometric curvature radii.

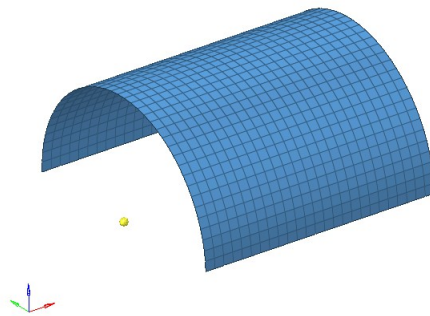


Figure 6.6. FE model, representation of a fine mesh

The model should be able to calculate the same geometric curvature radius on a more coarse mesh as in Fig. 6.7. Where the model has same radius of 5 mm but a mean mesh size of 1 mm aligned with the geometric curvature radii.

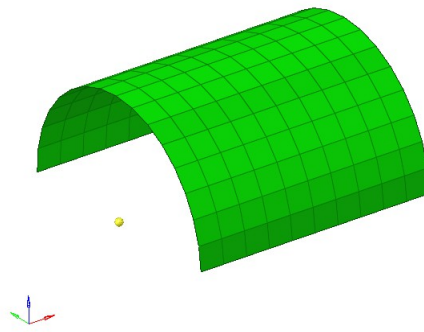


Figure 6.7. FE model, representation of a Coarse mesh

Here below in Fig. 6.8 is represented the comparison of the trending error in the calculation of the Radius for different mesh sizes with both developed methods. The results showed good results even with a coarse mesh of the geometry and showed little more precision by the projection method.

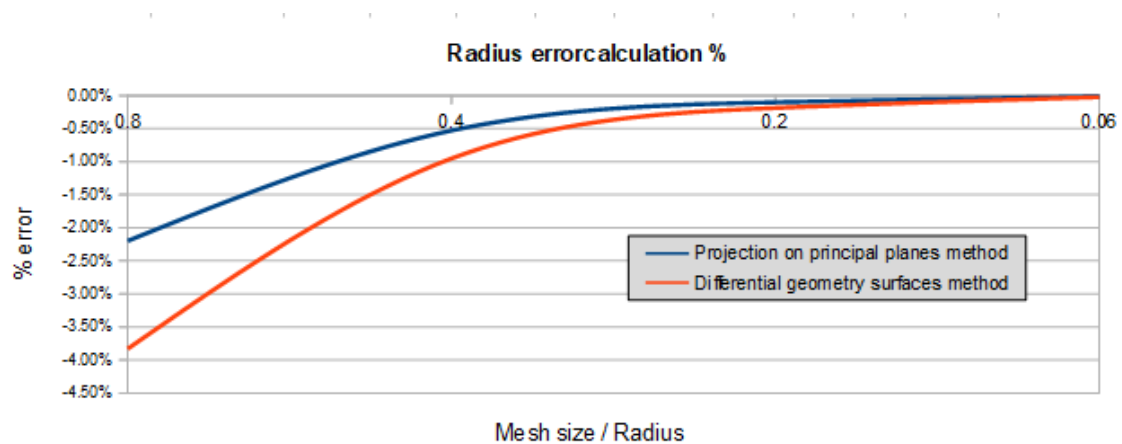


Figure 6.8. Error % on radius vs mesh size/Radius Ratio

Thus both methods give good results with a single geometric curvature geometry and an aligned mesh. The mesh sensitivity performed showed a maximum error of -2,5% in the calculation of the Radius with a 0.8 ratio between mesh size and radius, which is on the limit to be called proper mesh. The second test aims to look at the possibility to face a mesh not aligned with the radius as in Fig. 6.9 where is represented an arc of 180° of radius 5 mm with a random mesh of 1.0 mm mean size and the elements on top of the surface rotated by 45° (worst case) with respect to the principal curvature radius.

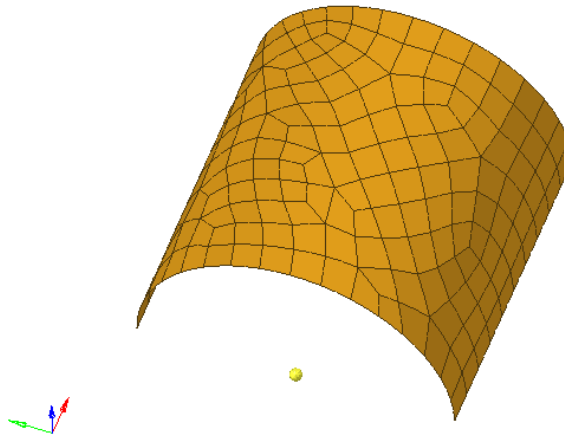


Figure 6.9. Non aligned mesh model

The difference between the two methods is quite highlighted in this case. Indeed, the projection method calculates the two geometric curvatures of the highlighted element in their local axis configuration even if with good precision, while the differential one catches the real global geometric curvature of the element Fig 6.10.

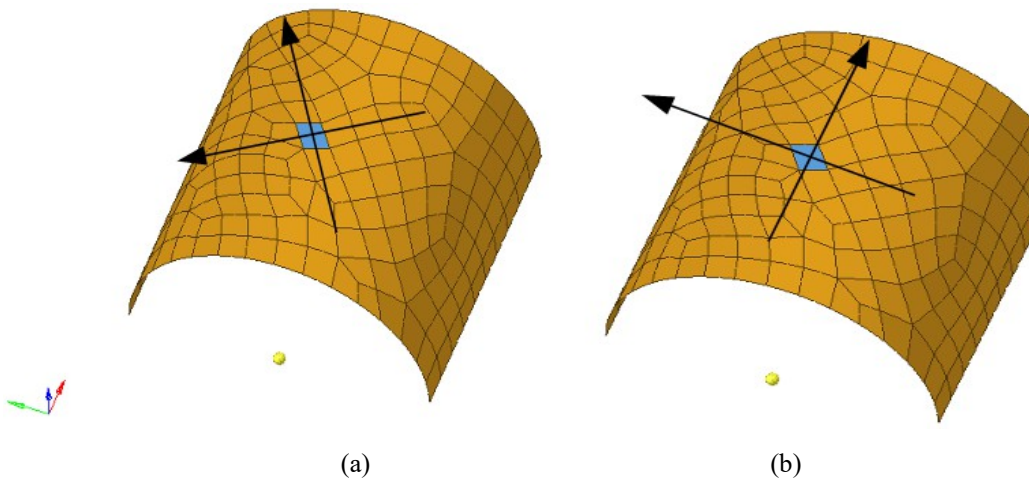


Figure 6.10. Principal curvature direction comparison. (a): Projection method. (b): Differential method

Since was chosen to perform the analysis in the principal geometric curvature system, the projection method for the calculation of the geometric curvature radii is abandoned.

6.2 Radial Equilibrium equation

A description of the doubly curved laminate panel and its equilibrium equation is given by Huang [1] and utilized by Ross in [2]. An infinitesimal fraction of laminate subdivided into angular segments $d\theta$ and $d\varphi$ is represented in Fig 6.11, where R_1 and R_2 are the principal geometric curvature radii taken to be constant, while θ and φ and R are the main coordinates.

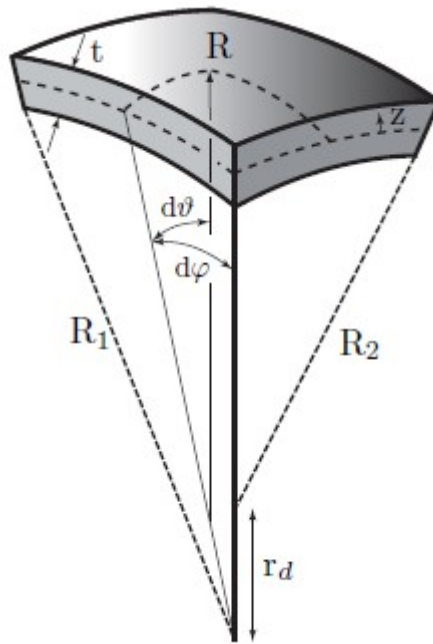


Figure 6.11. Infinitesimal fraction of a doubly curved laminate. From Compos Structures, Vol 81, R.Ross·G.Kress·P.Ermanni , A post-processing method for interlaminar normal stresses in doubly curved laminates, Pages 463-470 , copyright Elsevier (1999).

The equilibrium equations in the radial direction are [89]:

$$\frac{\partial \sigma_r}{\partial r} + \frac{1}{r} \frac{\partial \sigma_{\varphi r}}{\partial \varphi} + \frac{1}{r+D} \frac{\partial \sigma_{\theta r}}{\partial \theta} + \frac{\sigma_r - \sigma_\varphi}{r} + \frac{\sigma_r - \sigma_\theta}{r+D} = 0$$

$$\frac{\partial \sigma_{\varphi r}}{\partial r} + \frac{2}{r} \sigma_{\varphi r} + \frac{1}{r+D} \sigma_{\varphi r} + \frac{1}{r} \frac{\partial \sigma_\varphi}{\partial \varphi} + \frac{1}{r+D} \frac{\partial \sigma_{\varphi \theta}}{\partial \theta} = 0$$

$$\frac{\partial \sigma_{\theta r}}{\partial r} + \frac{1}{r} \sigma_{\theta r} + \frac{2}{r+D} \sigma_{\theta r} + \frac{1}{r} \frac{\partial \sigma_{\varphi \theta}}{\partial \varphi} + \frac{1}{r+D} \frac{\partial \sigma_\theta}{\partial \theta} = 0$$

Eq.

6.18

Where $r = R_1 + z$ and $D = R_2 - R_1$ with $z = \left(\frac{-t}{2}, \frac{t}{2}\right)$ and t is the element thickness.

To simplify the model maintaining a good accuracy the shear terms are neglected as proposed by Kress [87] with the first order theory. Then the equilibrium equation 6.18 is reduced to :

$$\frac{\partial \sigma_r}{\partial r} + \frac{\sigma_r - \sigma_\varphi}{r} + \frac{\sigma_r - \sigma_\theta}{r + D} = 0 \quad \text{Eq. 6.19}$$

The model gives good results in singly curved laminates [87] and also quite good results in a doubly curved laminates [2]. The flat plate model based on Kirckhoff [32] assumptions shows a linear strain distribution:

$$\varepsilon(z) = \varepsilon^0 + z \cdot k \quad \text{Eq. 6.20}$$

where ε is the strain and $z = \left(\frac{-t}{2}, \frac{t}{2}\right)$ is the through the thickness coordinate. But the curvature Radii causes a non-linear distribution of the strain through the thickness. The coordinate z is replaced by the radial coordinate r and the geometric curvature Radii R_1 and R_2 . Then the general deformations in-plane of the element, u and v , could be expressed as

$$\begin{aligned} d u &= R_1 \cdot d \varphi (\varepsilon_\varphi^0 + (r - R_1) k_\varphi) \\ d v &= R_2 \cdot d \theta (\varepsilon_\theta^0 + (r - R_2 + D) k_\theta) \end{aligned} \quad \text{Eq. 6.21}$$

While the strain is expressed as

$$\begin{aligned} \varepsilon_\varphi &= \frac{1}{r} \left(w + \frac{\partial u}{\partial \varphi} \right) \\ \varepsilon_\theta &= \frac{1}{r + D} \left(w + \frac{\partial v}{\partial \theta} \right) \\ \varepsilon_r &= \frac{\partial w}{\partial r} \end{aligned} \quad \text{Eq. 6.22}$$

The material law, neglecting the shear terms, becomes:

$$\begin{pmatrix} \sigma_\varphi \\ \sigma_\theta \\ \sigma_r \end{pmatrix} = \begin{pmatrix} C_{11} & C_{12} & C_{13} \\ C_{21} & C_{22} & C_{23} \\ C_{31} & C_{32} & C_{33} \end{pmatrix} \begin{pmatrix} \varepsilon_\varphi \\ \varepsilon_\theta \\ \varepsilon_r \end{pmatrix} \quad \text{Eq. 6.23}$$

By replacing eq 6.22 into eq 6.23, the material law can be expressed

$$\begin{aligned} \sigma_\varphi &= \frac{C_{11}}{r} \left(w + \frac{\partial u}{\partial \varphi} \right) + \frac{C_{12}}{r+D} \left(w + \frac{\partial v}{\partial \theta} \right) + C_{13} \frac{\partial w}{\partial r} \\ \sigma_\theta &= \frac{C_{21}}{r} \left(w + \frac{\partial u}{\partial \varphi} \right) + \frac{C_{22}}{r+D} \left(w + \frac{\partial v}{\partial \theta} \right) + C_{23} \frac{\partial w}{\partial r} \\ \sigma_r &= \frac{C_{13}}{r} \left(w + \frac{\partial u}{\partial \varphi} \right) + \frac{C_{23}}{r+D} \left(w + \frac{\partial v}{\partial \theta} \right) + C_{33} \frac{\partial w}{\partial r} \end{aligned} \quad \text{Eq. 6.24}$$

Combining the material law eq.6.24 with the equilibrium equation 6.19 is obtained a second order differential equation problem as already stated by Ross [2].

$$\begin{aligned} 0 &= C_{33} \frac{\partial w}{\partial r^2} + \frac{\partial w}{\partial r} C_{33} \left(\frac{1}{r} + \frac{1}{r+D} \right) \\ &+ w \left[-\left(\frac{C_{11}}{r^2} \right) - \left(\frac{C_{22}}{(r+D)^2} \right) + \frac{(C_{32}+C_{31})}{r(r+D)} - 2C_{12} \right] \\ &+ u_\varphi \left[-\left(\frac{C_{11}}{r^2} \right) + \frac{(C_{31}+C_{21})}{r(r+D)} \right] + v_\theta \left[-\left(\frac{C_{22}}{(r+D)^2} \right) + \frac{(C_{32}+C_{11})}{r(r+D)} \right] \\ &+ \frac{\partial u_\varphi}{\partial r} C_{31} + \frac{\partial v_\theta}{\partial (r+D)} C_{32} \end{aligned} \quad \text{Eq. 6.25}$$

Where the derivatives of the displacements along the principal curvatures can be expressed as:

$$\begin{aligned} u_\varphi &= R_1 (\varepsilon_\varphi^\circ + (r-R1) k_\varphi) \\ \frac{\partial u_\varphi}{\partial r} &= R_1 k_\varphi \\ v_\theta &= R_2 (\varepsilon_\theta^\circ + (r-R2+D) k_\theta) \\ \frac{\partial v_\theta}{\partial r} &= R_2 k_\theta \end{aligned} \quad \text{Eq. 6.26}$$

6.3 Numerical resolution of radial equilibrium

The second order differential equation obtained from radial equilibrium equation can be generally written as

$$\ddot{w} + \alpha(r)\dot{w} + \beta(r)w = P(r) \quad \text{Eq. 6.27}$$

Where $P(r)$ represents the constant terms.

The solution of this differential equation is found through the finite difference explicit method [90]The thickness of the laminate is discretized into a certain number of points and the derivatives of the displacement w are expressed as eq. 6.28.

$$\begin{aligned} \dot{w} &= \frac{w_{n+1} - w_{n-1}}{2d} \\ \ddot{w} &= \frac{w_{n+1} - 2w_n + w_{n-1}}{d^2} \end{aligned} \quad \text{Eq. 6.28}$$

Where w_n represent the displacement through-the-thickness of each through-the-thickness point of the system of equation and d is the distance between two of the supporting points. The boundary conditions are represented by the ILTS equal to zero at the top and the bottom surfaces of the laminate [91].Moreover, if the laminate consists of several plies, there are other two boundary conditions at each interface between different plies that have to be satisfied. These additional boundary conditions are described by the continuity of the displacement and the stress through all the thickness. As a consequence, other 2 supporting points are necessary for each interface between layers. The additional equations at the interfaces can be expressed by:

$$w_n = w_{n+3} \quad \text{Eq. 6.29}$$

$$\sigma_n(r_n) = \sigma_{n+3}(r_{n+3}) \quad \text{Eq. 6.30}$$

The supplementary points are placed outside the ply borders. Considering n the point of a the layer A, placed on its border with the layer B. There are 2 supplementary points at this interface, supporting the additional equations, indicated with $n+1$ and $n+2$. These

points are not placed on the border, indeed the point $n+1$ is still part of the layer A but exceed the layer border into the layer B. While the point $n+2$ is part of the layer B but exceeds the layer border into the layer A. As shown in Fig 6.11 the point n and $n+3$ are placed on the layer interface. The points $n-1$ and $n+2$ are placed into the layer A, but one is part of the layer A and the other is part of the layer B. and the points $n+1$ and $n+4$ are placed into the layer B, but again the point $n+1$ is part of the layer A while the point $n+4$ is part of the layer B. Here below a representation of the layer interface scheme for the differential system solution:

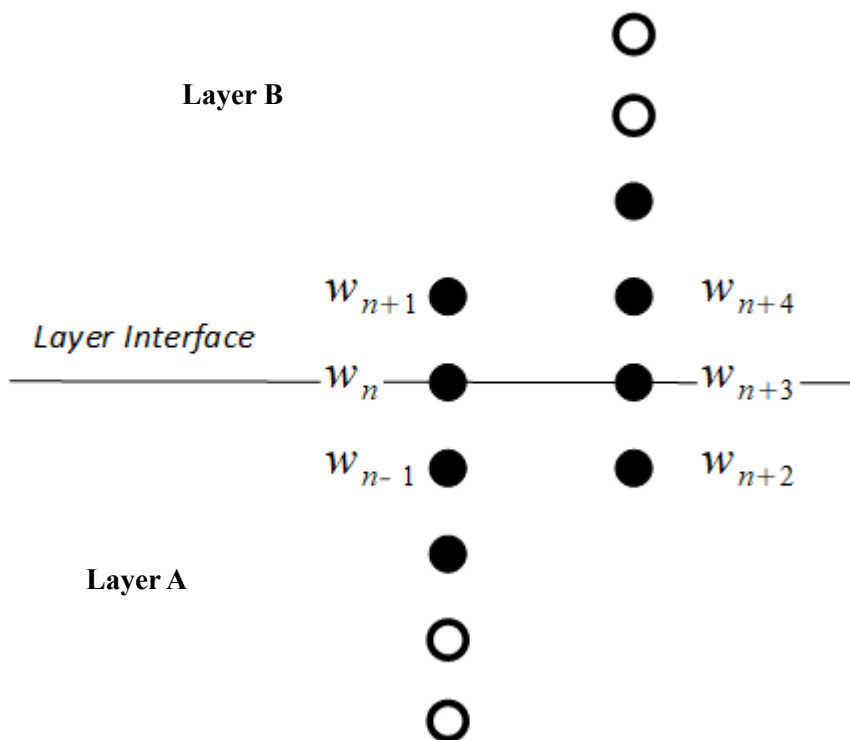


Figure 6.12. layer interface scheme for finite difference calculation

Then the eq 6.27 can be expressed in terms of displacements w_n of the eq 6.28:

$$w_{n-1} \left(\frac{-C_{33}}{2d} \right) + w_n \alpha_n + w_{n+1} \left(\frac{C_{33}}{2d} \right) + w_{n+3} (-\alpha_{n+3}) + w_{n+4} \left(\frac{-C_{33}}{2d} \right) = \beta_{n+3} - \beta_n \quad \text{Eq. 6.31}$$

The through the thickness distribution of the ILTS can be calculated with the eq 6.24. Moreover, the precision of the calculation will be affected by the numbers of integration point used.

6.4 A comparison of curvature aware and curvature unaware laminate theories

The Kirckhoff [28] hypothesis of linear strain distribution through-the-thickness for flat plates can be expressed by the eq 6.32

$$\varepsilon(z) = \varepsilon^0 + z \cdot k \quad \text{Eq. 6.32}$$

Where z is the coordinate along the thickness t of the shell and is defined as $z = [\frac{-t}{2}, \frac{t}{2}]$

and ε^0 are the in-plane strains and k the deformative curvatures. In the case of a single geometric curvature plate, the geometric curvature radius R causes a non linear distribution of the strain through-the-thickness. Indeed the neutral axis, as a result of deformation, is no more placed in the middle of the thickness but is shifted toward the intrados face. This condition of the neutral axis causes higher strain around the minor radius face of the plate. To help describing this particular strain distribution a rational function $Z(z)$ is introduced in eq 6.33

$$Z(z) = \frac{R}{(R - z)} \quad \text{Eq. 6.33}$$

Then the strain distribution expressed in eq 6.32 can be combined with eq 6.33

$$\varepsilon(z) = Z \cdot \varepsilon^0 + Z \cdot z \cdot k \quad \text{Eq. 6.34}$$

In the case of $R = \infty$, the rational function $Z(z) = 1$ and the eq 6.34 becomes equal to eq 6.32, a linear distribution of strain.

The in- plane strains through-the-thickness in a polar coordinates system can be expressed as:

$$\begin{Bmatrix} \varepsilon_{\varphi} \\ \varepsilon_{\vartheta} \\ \gamma_{\varphi\vartheta} \end{Bmatrix} = \begin{Bmatrix} Z \cdot \varepsilon_{\varphi}^0 \\ Z \cdot \varepsilon_{\vartheta}^0 \\ Z \cdot \gamma_{\varphi\vartheta}^0 \end{Bmatrix} + z \begin{Bmatrix} Z \cdot \kappa_{\varphi} \\ Z \cdot \kappa_{\vartheta} \\ Z \cdot \kappa_{\varphi\vartheta} \end{Bmatrix} = \begin{bmatrix} Z & 0 & 0 \\ 0 & Z & 0 \\ 0 & 0 & Z \end{bmatrix} \left(\begin{Bmatrix} \varepsilon_{\varphi}^0 \\ \varepsilon_{\vartheta}^0 \\ \gamma_{\varphi\vartheta}^0 \end{Bmatrix} + z \begin{Bmatrix} \kappa_{\varphi} \\ \kappa_{\vartheta} \\ \kappa_{\varphi\vartheta} \end{Bmatrix} \right) \quad \text{Eq. 6.35}$$

Where φ and ϑ are the tangential directions, corresponding to x, y of a cartesian coordinate system. Thus, following the CLT [32] assumption which states that each layer of the laminate is subjected only to planar stress, the material law can be expressed as:

$$\sigma = \bar{Q} \cdot \varepsilon \quad \text{Eq. 6.36}$$

Where the stiffness matrix Q is expressed as:

$$\bar{Q} = \begin{bmatrix} Q_{11} & Q_{12} & Q_{13} \\ Q_{21} & Q_{22} & Q_{23} \\ Q_{31} & Q_{32} & Q_{33} \end{bmatrix} \quad \text{Eq. 6.37}$$

The integration through-the-thickness follows the CLT combining eq 6.36 with eq 6.34 and the result is the ABD matrix (I.e stiffness matrix) for a curved laminate.

$$\begin{Bmatrix} N \\ M \end{Bmatrix} = \sum_{k=1}^N \int_{z_{k-1}}^{z_k} \sigma \begin{Bmatrix} 1 \\ z \end{Bmatrix} dz = \sum_{k=1}^N \bar{Q}_k \int_{z_{k-1}}^{z_k} \begin{bmatrix} 1 & z \\ z & z^2 \end{bmatrix} dx \begin{Bmatrix} \varepsilon^0 \\ \kappa \end{Bmatrix} \quad \text{Eq. 6.38}$$

Where N is the number of total layers, k is the pointer indicating the current layer, while $z(k)$ and $z(k-1)$ represent the coordinate along the z axis (through-the-thickness of the laminate) the end and the beginning of a layer. $Q(k)$ is the stiffness matrix of the k layer and it depends on the orientation of the lamina. Thus, the eq 6.38 could be written in its short form as :

$$\begin{Bmatrix} N \\ M \end{Bmatrix} = \begin{bmatrix} \bar{A} & \bar{B} \\ \bar{B} & \bar{D} \end{bmatrix} \begin{Bmatrix} \varepsilon^0 \\ \kappa \end{Bmatrix} \quad \text{Eq. 6.39}$$

And A, B and D are 3X3 matrices that for a flat plate are defined as:

$$[A, B, D] = \sum_{k=1}^N \bar{Q}_k [(z_k - z_{k-1}), \frac{1}{2}(z_k^2 - z_{k-1}^2), \frac{1}{3}(z_k^3 - z_{k-1}^3)] \quad \text{Eq. 6.40}$$

While in case of the curved laminate the A,B,D matrices are updated introducing the diagonal Z matrix of eq 6.33

$$\begin{bmatrix} \bar{A}_z & \bar{B}_z \\ \bar{B}_z & \bar{D}_z \end{bmatrix} = \sum_{k=1}^N \bar{Q}_k \int_{z_{k-1}}^{z_k} \begin{bmatrix} 1 & z \\ z & z^2 \end{bmatrix} \bar{Z}(z) dz \quad \text{Eq. 6.41}$$

In components made by fiber composite materials, the aim is usually to not have flexural-membrane couplings, and it is possible when all the terms of B-matrix are equal to 0. Besides, the case of the curved laminate, both in symmetric and quasi-isotropic laminate, there is a flexural-membrane coupling. This coupling is emphasized when the geometric curvature radius/ laminate thickness (C/LT) ratio tends to 0.5 (case of a solid cylinder). While, in the case the C/Lt ratio tends to ∞ , the flexo - membrane coupling is equal to 0 (flat plate case).

The stiffness difference between flat and curved laminate is investigated with an eigenvalues analysis.

$$K_p \cdot V = K_c \cdot V \cdot \lambda \quad \text{Eq. 6.42}$$

Where K_p and K_c are the stiffness matrices of the Flat and Curved laminate, V is a matrix of eigenvectors and λ is the diagonal matrix of eigenvalues. The eigenvectors that can be found with this equation represent the strain states which make the vectors of forces and moments of the two stiffness matrices comparable. The eigenvectors point out the difference between the two stiffness matrices, the difference is then represented in the eigenvalues diagonal matrix. To asses the difference between the stiffness matrices of a flat and a curved laminate, a couple of tests are performed with the C/LT ratio varying between 0.5 and 100. For each test is plotted the maximum and minimum eigenvalue.

The performed tests are:

- Cloths laminate, all plies at 0°
- Cloths laminate, all plies at 45°

- Cloths laminate, mixed angle ($0^\circ/45^\circ/45^\circ/0^\circ$)
- Cloths laminate, mixed angle ($45^\circ/0^\circ/0^\circ/45^\circ$)
- Mixed laminate, mixed angles (45° CI/ 0° UD/ 0° CL/ 0° UD/ 45° CL)

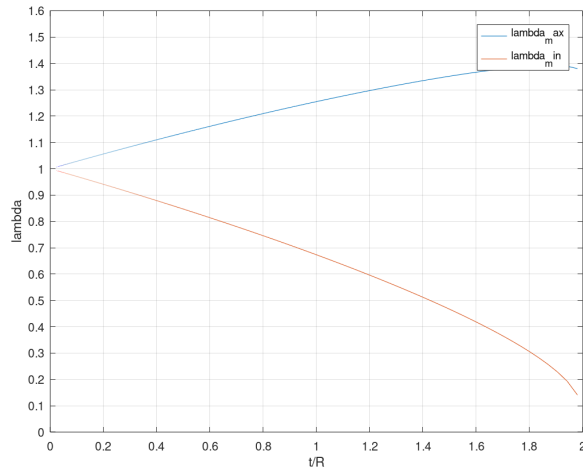


Figure 6.13. Stiffness comparison for a 0° cloth laminate. The blue line represents the maximum eigenvalue and the red line indicates the minimum eigenvalue for different C/LT ratios.

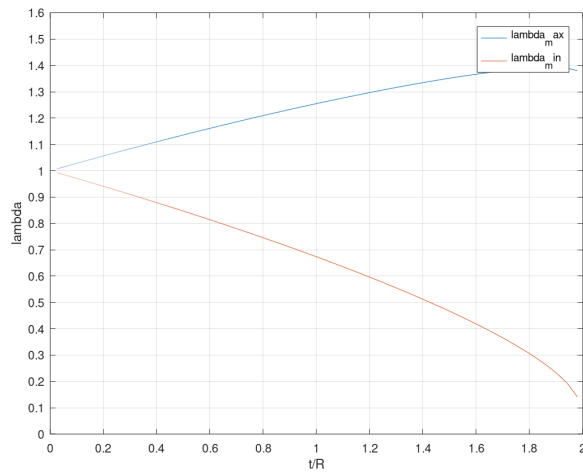


Figure 6.14. Stiffness comparison for a 45° cloth laminate. The blue line represents the maximum eigenvalue and the red line indicates the minimum eigenvalue for different C/LT ratios.

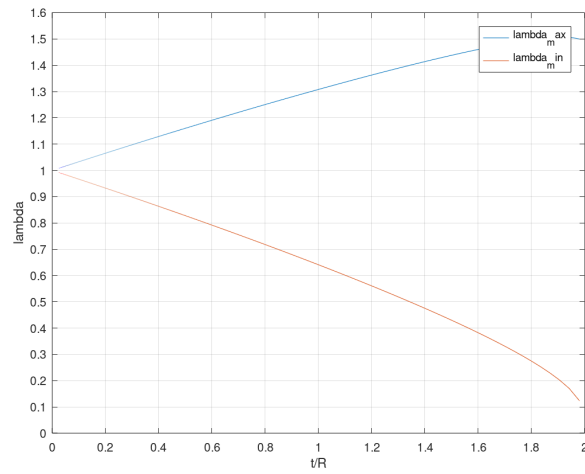


Figure 6.15. Stiffness comparison for a $(0^\circ/45^\circ/45^\circ/0^\circ)$ cloth laminate. The blue line represents the maximum eigenvalue and the red line indicates the minimum eigenvalue for different C/LT ratios.

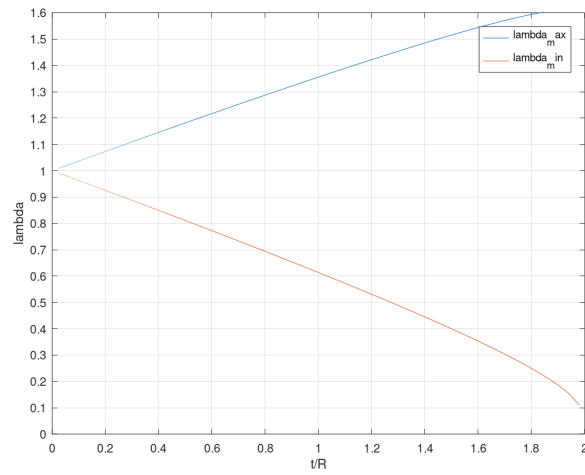


Figure 6.16. Stiffness comparison for a $(45^\circ/0^\circ/0^\circ/45^\circ)$ cloth laminate. The blue line represents the maximum eigenvalue and the red line indicates the minimum eigenvalue for different C/LT ratios.

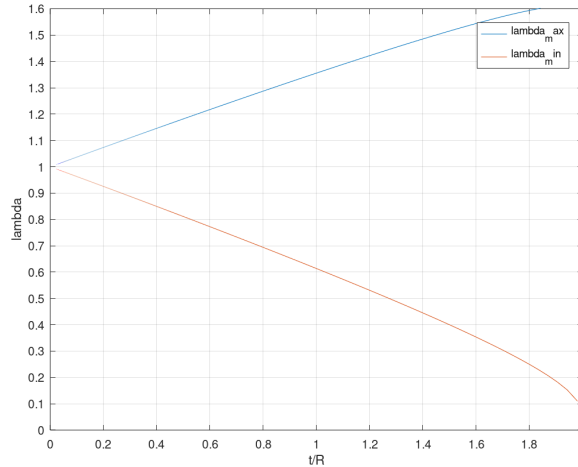


Figure 6.17. Stiffness comparison for mixed UD & cloths laminate. The blue line represents the maximum eigenvalue and the red line indicates the minimum eigenvalue for different C/LT ratios.

The stiffness difference between the flat and curved laminate stiffness matrices vanishes when the radius tends to ∞ as can be seen in figures above, and is not depending on laminate stacking sequence. Indeed, several performed tests highlighted this behavior. While, the difference in stiffness matrix between flat and curve laminate increases with a non linear trend with a maximum at the C/LT ratio of 0.5, which is not a physical limit, indeed, this C/LT ratio is only representing a Cylinder, while a curved geometry could have even higher thicknesses. The point is that over a certain C/LT ratio a 2D shell FE model is no more representative of the component behavior with respect to a 3D model.

6.5 Laminate features influencing ILTS

The two main parameters influencing the ILTS magnitude are the geometry curvature / laminate thickness (C/LT) ratio and the orthotropic level [92]. The orthotropic level is defined as $E1/E3$ where $E1$ is the in-plane Young's modulus along the principal geometric curvature direction; $E3$ is the out of plane Young's modulus. To investigate the behavior of the ILTS varying the C/LT ratio and the $E1/E3$ ratio, a numerical analysis (with FEM) is performed. The laminate considered for the several tests is orthotropic and homogeneous for simplicity. The FE model used to perform the analysis is axial symmetric for computational cost reasons. The model represents a circular section, thus, only the axial symmetric rectangular portion of it is meshed. The thickness of the rectangular section is 1mm and the average curvature radius of the geometry is 1mm. The total width is 10 mm but just half geometry is represented, exploiting the symmetry plane normal to the cylinder axis. Fig 6.18 illustrates the mesh in white and the symmetry plane constraints in red.

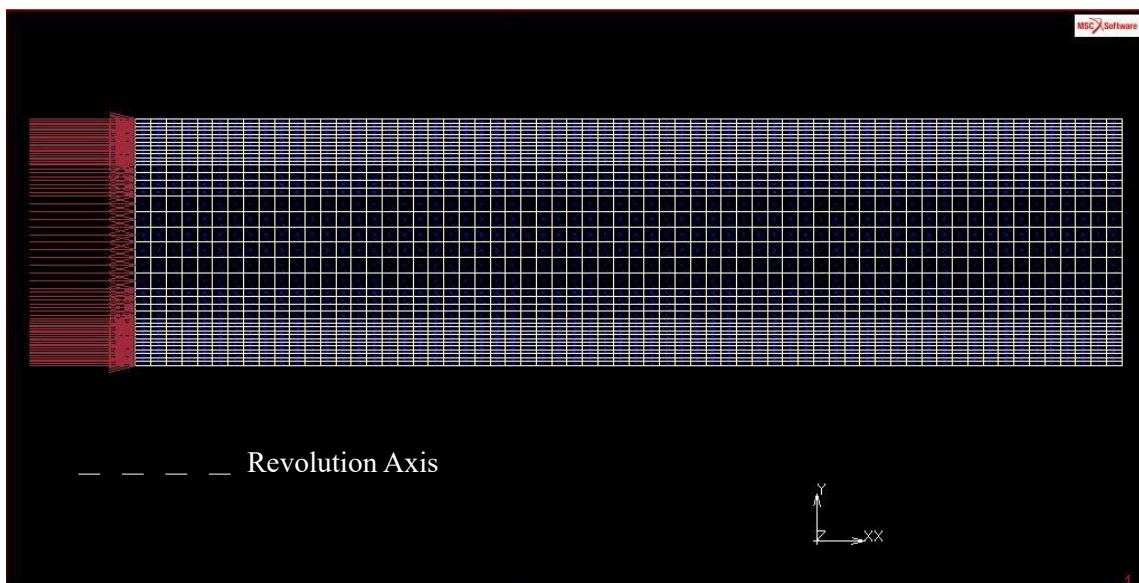


Figure 6.18. FE axis symmetric model

The mesh consists of shell 8 nodes elements, and the mesh size is decreased from the middle of the section to the edges. The model is loaded with a unitary bending moment, the application axis correspond to the revolution axis, the moment is applied by a thermal gradient. The thermal expansion coefficient in radial and axial direction (X and Y in Fig. 6.18) are equal to 0, while the one in tangent direction is equal to 1, the aim is to impose the circular section to expand only in a tangential direction. The imposed thermal gradient ΔT is unitary.

The tests are divided into two types:

- E1/E3 ratio variation
- C/LT & E1/E3 ratio variation

6.5.1 Results: E1/E3 variation

The first group of tests keeps the model geometry constant (Radius and laminate thickness) and the E1/E3 ratio is changed. Fig. 6.19 represents the reference model's ILTS distribution through-the-thickness. The results are obtained with software Marc [93]

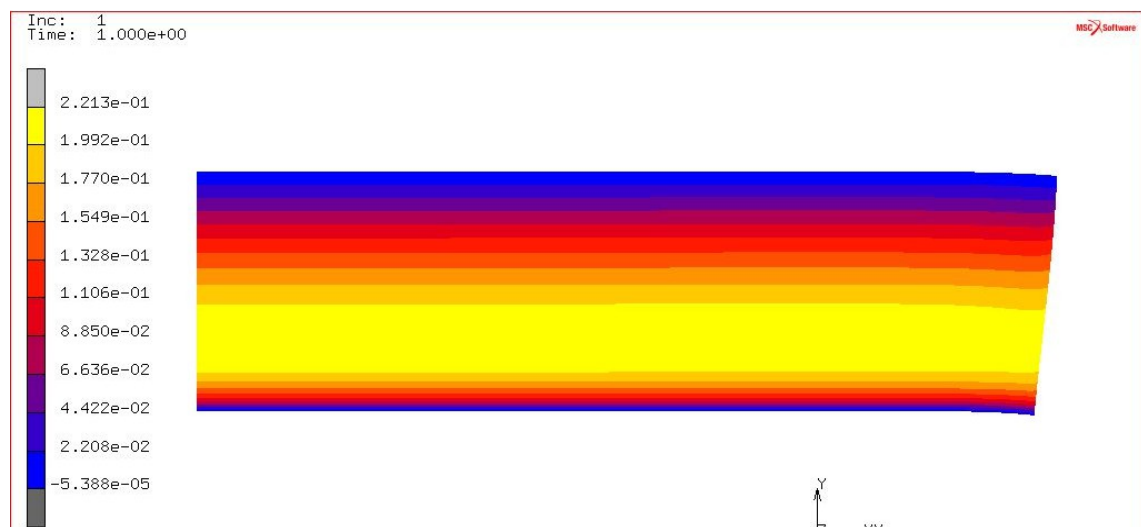


Figure 6.19. FE Results: ILTS through-the-thickness

The ILTS trend through-the-thickness is equal to 0 at the top and the bottom of the laminate. The maximum ILTS value is reached near the inner surface of the circular section. In the subsequent tests the C/LT ratio is fixed and the $E1/E3$ ratio is varied by decreasing the $E3$ modulus. Fig 6.20 reports the main results. The ILTS is less influenced by the $E1/E3$ ratio in a range between 1 and 10, then from 10 to 100 there is a decrease. The ILTS with a $E1/E3$ ratio of 100 is around 20% smaller than that corresponding to an $E1/E3$ ratio of 10.

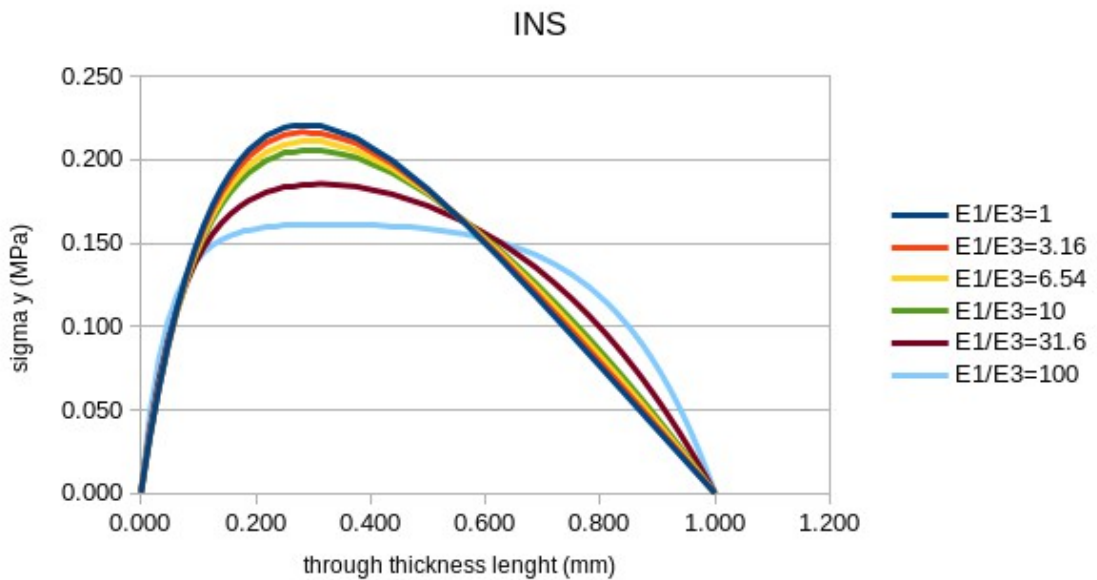


Figure 6.20. Results: ILTS through-the-thickness

6.5.2 Results: C/LT variation

The group of tests concerning the variation of the geometric curvature/ laminate thickness ratio (C/LT) is performed with a Matlab [94] code. The variation range of C/LT is between 0.5 and 4, while the $E1/E3$ ratio is varied too between 1 and 100. In Fig. 6.21 are illustrated the results in terms of Maximum ILTS of the analysis performed, the full lines refer to the numerical results while the dashed lines refer to the

Kedward formulation [92]. For every C/LT ratio tested is represented the ILTS trend varying the $E1/E3$ ratio. The ILTS is less influenced by the $E1/E3$ ratio with high C/LT ratios. The C/LT ratios are indicated with Rt .

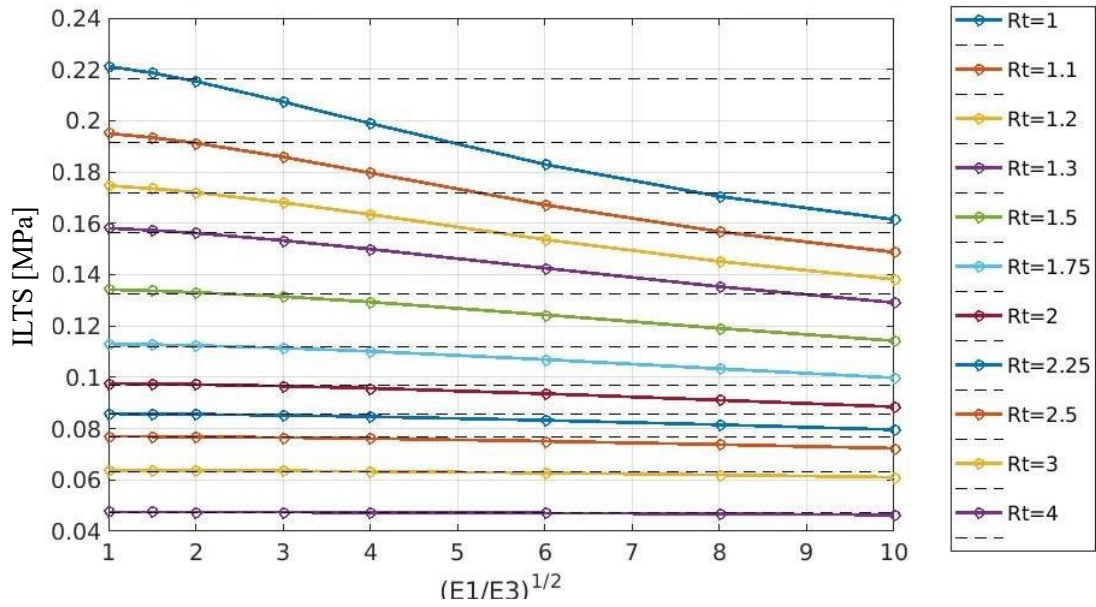


Figure 6.21. Results: Maximum ILTS

6.6 Model Implementation

The post processing method for calculating the ILTS in doubly curved laminates is implemented in a self-developed code for MATLAB [94] and also OCTAVE [95] software. The code is built to interface with the pre-processing, analysis and post-processing software which belong to the Hyperworks pack [96].

Looking at it as a black box, it collects in input data from the FE model under analysis and generates as output a file suitable for Hyperview (Altair pack) which includes the ILTS results of each analyzed element.

More in particular, once collected all the relevant information, the in-made code starts a FOR loop, and, for every element to be analyzed, it calculates the element curvature and the element's stiffness matrix. Then, before starting the numerical resolution of radial equilibrium, it projects the strain and stiffness matrices onto the geometric curvature system. Finally, once calculated the radial displacements, the in-made code generates the through-the-thickness ILTS trend. The output file could contain the maximum ILTS value or the complete trend for each analyzed element. The following paragraphs focus on the required information, the out of plane material properties involved in the stiffness matrix building and a more detailed elucidation of the reference system employed.

6.6.1 Required information

The required information are read from the input FE model file and the results file, then are stored in Map Data Structures, which are a fast key lookup data structures.

The in-made code collects from the input FE model the following information:

- nodes Ids and coordinates
- elements IDs and nodes
- element material principal orientation
- element properties
- element normal direction

- element offset
- material properties
- laminate number of plies and stacking sequence
- plies extensions
- plies orientations
- plies' materials

While from the result file, the in-made code collects data about :

- Top and bottom elements strain matrix
- strain angle
- element laminate thickness

6.6.2 Out of plane materials' properties

The in-made code collects, from the input FE model file, the data about plies material properties. These properties are usually expressed specifically for shell elements, indeed the only terms that are used for the 2D FE model analysis are the in-plane Young's modulus (E_1, E_2), Shear modulus (G_{12}), Poisson coefficient (ν_{12}). Where 1 and 2 represent the in-plane main directions and 3 the out of plane direction.

Whereas, for the numerical resolution of the radial equilibrium is required a 3D expression of such material properties, which means, the definition of the out of plane Young's modulus (E_3), Shear modules (G_{13}, G_{23}), Poisson coefficients (ν_{13}, ν_{23}). Thus, depending on the availability of these information, the code allows to read (from the FE model input file) or manually set (a priori) the out of plane material properties.

6.6.3 Systems of References

All the evaluations are referred to the principal geometric curvatures system, so that all the strain matrix and material stiffness matrix are rotated along that system.

In Fig. 6.22 are represented the main direction that are influencing the calculation:

- \mathbf{x} is the element direction (usually defined by the first two nodes G1 and G2), the strain are written along this direction
- \mathbf{m} is the principal material direction, the reference upon which the orientation of a ply of a composite laminate is defined
- \mathbf{a} is the principal geometric curvature direction and is the reference for the ILTS evaluation of the analytical model
- $\mathbf{1}$ is the ply direction

Furthermore, there are three principal angles among these directions:

- α_{mx} the angle of the material respect to the element direction
- α_{1m} the angle between the ply direction and the material reference direction
- α_{xa} the angle between the element reference direction and the principal geometric curvature direction

these angles are used to let the strain matrix and the stiffness matrix rotate toward the principal geometric curvature direction.

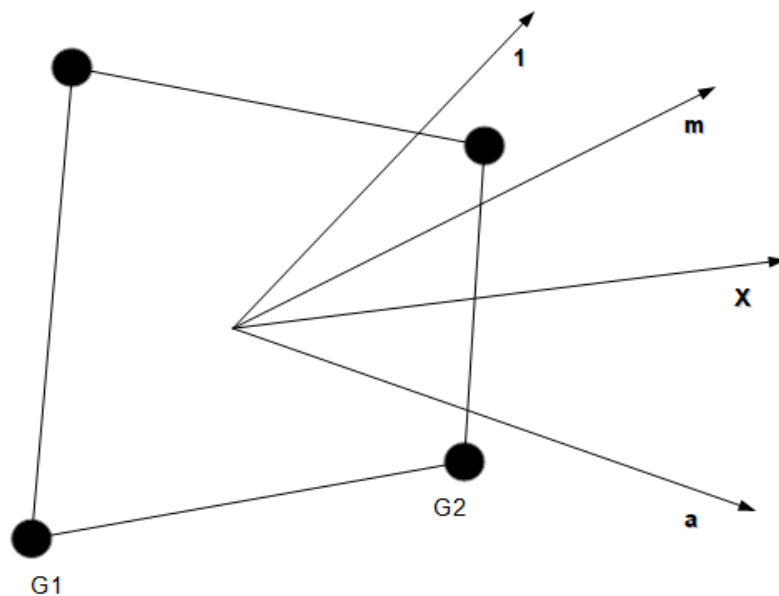


Figure 6.22. Linear 4nodes shell element main directions

7. Single geometric curvature FE Test

The post processing analytical method is tested on geometries with gradually more complex features and the test mainly consists of a comparison between the results of the post processing analytical model (that is based on the 2D shell FE model results) and a 3D Solid FE model.

The first test is performed on a single geometric curvature geometry which is quite simple, indeed a portion of a cylinder is used as reference . Once the geometry is defined, some features can be modified to perform several test, these are:

- overall Thickness
- ply thicknesses
- ply Stack Sequence

One of the FE models is described with details shared by all tested models . In this first case, a portion of 180° of a cylinder is generated by extruding an arc. The arc is centered on [0,0,0] and has a Radius of 5mm placed on the x-y plane, the extension of the semicylinder is 10 mm along x. The mesh size is around 0.8 mm and is aligned with the geometric curvature radius. Since the geometric curvature radius/ mesh size ratio is 0.16, as consequence the radius calculated by the model has a maximum error <0.02% as previously illustrated. The mesh consists of 4nodes shell elements (CQUAD4 in Optistruct [96]).

One end of the semi-cylinder is linked with a rigid link (RBE2) and fixed in all its DoF while on the other end is applied a Linear Force of 100N along Y+. The model consists of 260 elements and 294 nodes +2 nodes for the RBE 2. The 4 node shell elements are used to calculate the elements strain. While the model with 8nodes shells (CQUAD8 in Optistruct) is used just for the Radius calculation with the post processing model, indeed this auxiliary model is saved apart. The element's normal is assigned in order to simulate a laminate growing toward the inside (decreasing Radius) or the outside (increasing radius) of the structure depending on test case. The laminate stack is created in Hypermesh and assigned through a composite property to the elements (PCOMPP in

Optistruct). The main direction of the material is assigned to be along X for all the elements of both the FE models.

Here below in Fig. 7.1 the representation of the shell 2D model with its boundary conditions and a representation of a 1.5 mm thickness laminate developing toward the inside.

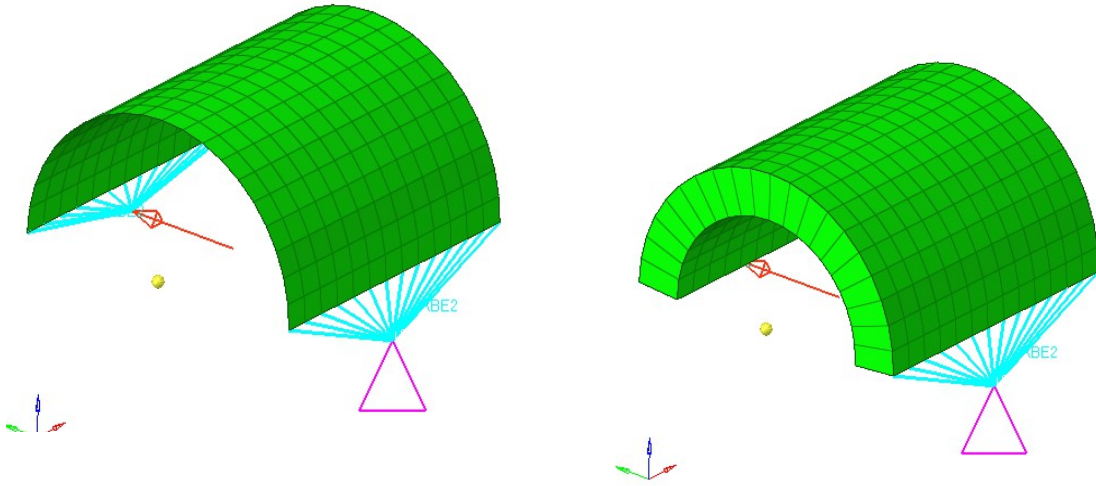


Figure 7.1. 2D shell element and its 3D representation

Two carbon fiber reinforced plastic composite material (CFRP) are used for the numerical tests. Here below in table 1 and table 2 are shown the main structural properties for the composite cloth and UD used for the numerical and analytical calculations:

Composite Cloth						
E_1	50000	MPa		ν_{13}	0.3	
E_2	50000	MPa		G_{12}	6000	MPa
E_3	6000	MPa		G_{23}	4000	MPa
ν_{12}	0.05			G_{13}	4000	MPa
ν_{23}	0.3					

Table 1. Composite cloth material properties

Composite UDs						
E_1	105000	MPa		ν_{13}	0.3	
E_2	6000	MPa		G_{12}	6000	MPa
E_3	5000	MPa		G_{23}	4000	MPa
ν_{12}	0.05			G_{13}	4000	MPa
ν_{23}	0.3					

Table 2. Composite UD material properties

The 3D FE model is created directly from the 2D 4node shell model. The 2D elements are extruded along their normal to create 8nodes solid elements (CHEXA in Optistruct), the height of each element is the layer thickness they represent.

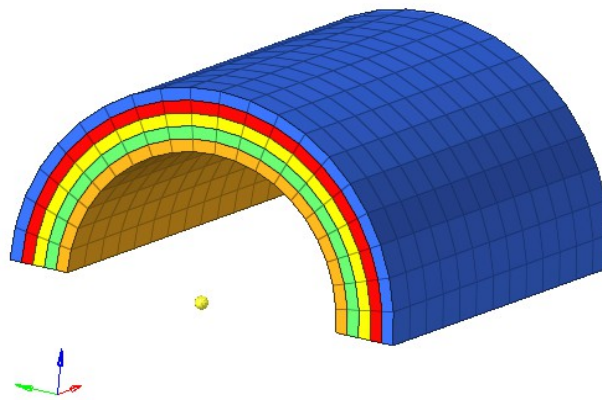


Figure 7.2. 3D solid model elements

In Fig. 7.2 is shown a rendering of a 1.5 mm overall thickness laminate, where each ply is 0.3 mm thick so that the 3D model has 5 solid elements of 0.3mm height through the thickness. The laminate grow inward with respect to the 2D shell elements.

The elements share a solid composite property (PCOMPLS in Optistruct) where are indicated thickness, material and direction of each ply assembling the laminate. Besides, the material principal direction is assigned to be along X as for the 2D shell model.

7.1 Single geometric curvature FE Test: Results

The first result showed is a comparison among FE models with different geometric curvature Radius/ overall laminate thickness ratio. The models share the same geometric curvature radius ($R= 5\text{mm}$) but differ in overall thickness and number of plies. The laminates are kept simple and as first test three configurations are analyzed:

1. All Cloths at 0°
2. All Cloths at 45°
3. All cloths with alternated orientation $0^\circ/45^\circ$

each ply has a thickness of 0.3mm and laminates with a geometric curvature radius / laminate thickness ratio inside the range $[10.0 - 0.5]$ are tested.

7.1.1 Single geometric curvature FE Test: maximum ILTS Value

Results show that the postprocessing analytical model tends to underestimate the maximum value of ILTS of the laminate for each type of simple laminate (0° and 45° cloths). There is a range between 10.0 and 2.0 (of geometric curvature C/LT ratio) where the error on the maximum ILTS is between 8% and 20% as can be seen in Fig. 7.3. as the ratio become smaller and the laminate has relevant thickness respect to the geometric curvature radius the underestimation become quite high, but also the concept of shell become uncomfortable with laminate thicknesses that are so big, indeed the results in strain and stresses start to have a significant distance from the 3D FE solid model.

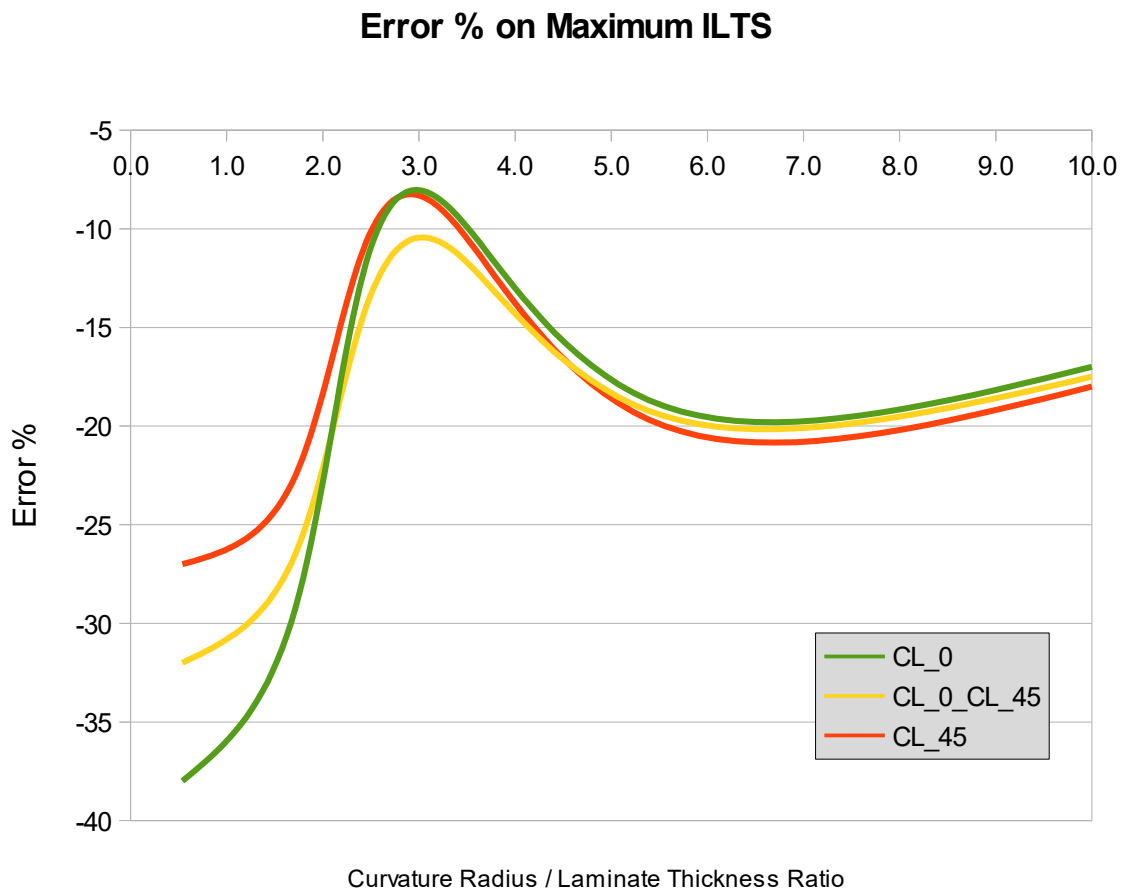


Figure 7.3. Error % on maximum ILTS value vs radius/thickness ratio

7.1.2 Single geometric curvature FE Test: maximum ILTS region

Qualitatively, the post processing model is able to pick the extension of the area with important amount of ILTS. Indeed as can be seen in Fig. 26 the laminate 1 (with all cloths at 0°) presents the maximum ILTS at around 90° of the 180° of the arc, and the area with high ILTS extends for all the length of the semi cylinder. While the laminate 2 (all cloths at 45°), even presenting the maximum at around 90° of the circumference, shows a more circumscribed area with remarkable ILTS.

In fig 7.4 are shown the ILTS results of the 2 tested laminates for a 2.1 mm thick model composed by 7 plies of 0.3mm thickness. The 3D model results are ISO cut to let the most stressed elements be better visible, because of their position inside the laminate.

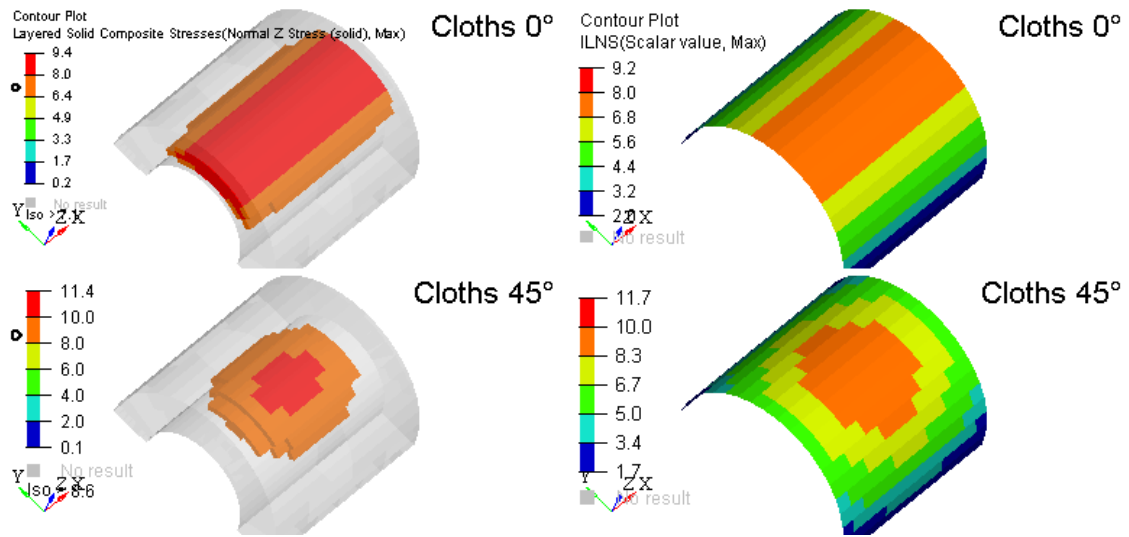
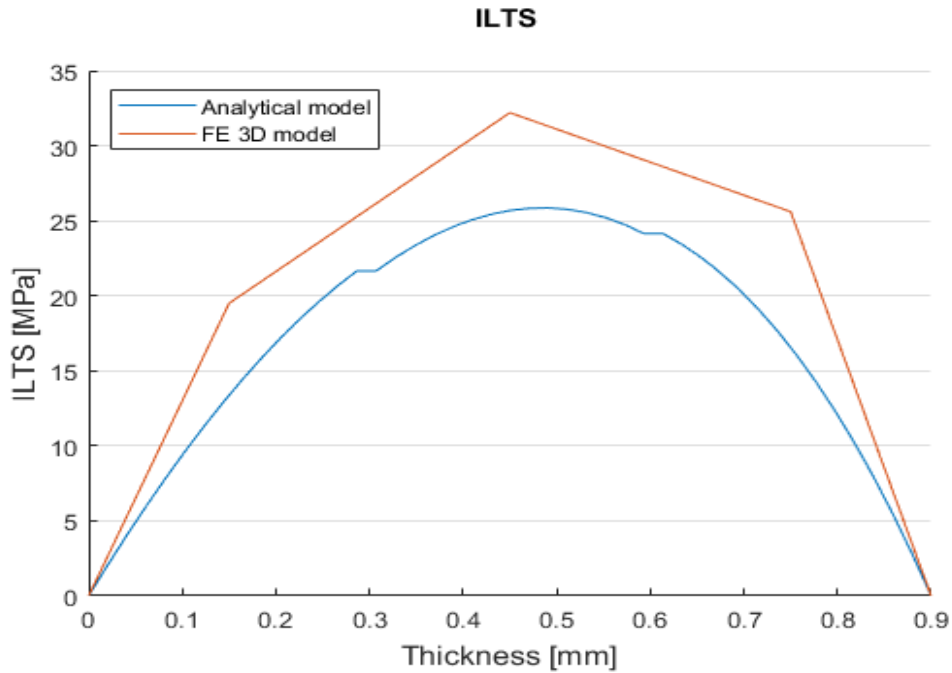


Figure 7.4. ILTS results comparison for a 0° and 45° cloths laminate

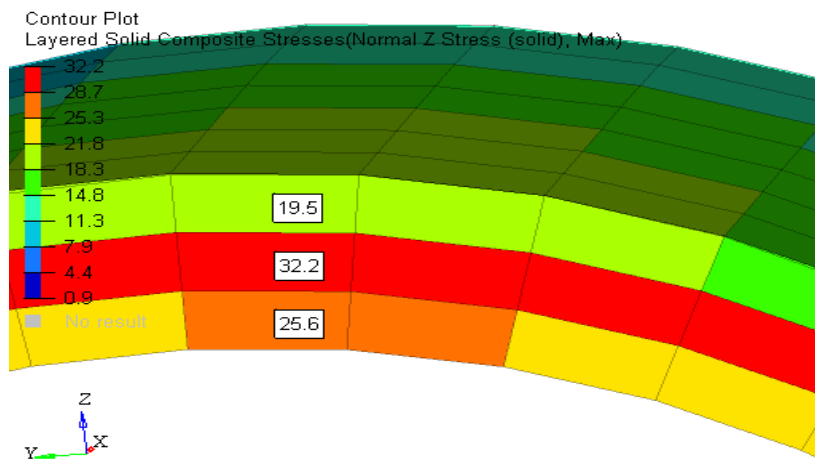
7.1.3 Single geometric curvature FE Test: ILTS distribution through-the-thickness

A comparison between the FE 3D solid model and the post processing analytical model is done to check the precision to calculate the maximum ILTS along the overall thickness of the laminate. The comparison is done on FE models sorted by thickness.

In Fig. 7.5 are shown the results of a 0.9mm thick laminate composed by 3 cloth ply (0°/0°/0°). The analytical model shows the expected parabolic curve of ILTS along the laminate thickness, with values equal to 0 at the borders and the maximum ILTS reached in the middle of the laminate, the curve is not symmetric in both analytical and 3D solid models, but the inner ply (which is in tension) is a bit more stressed.



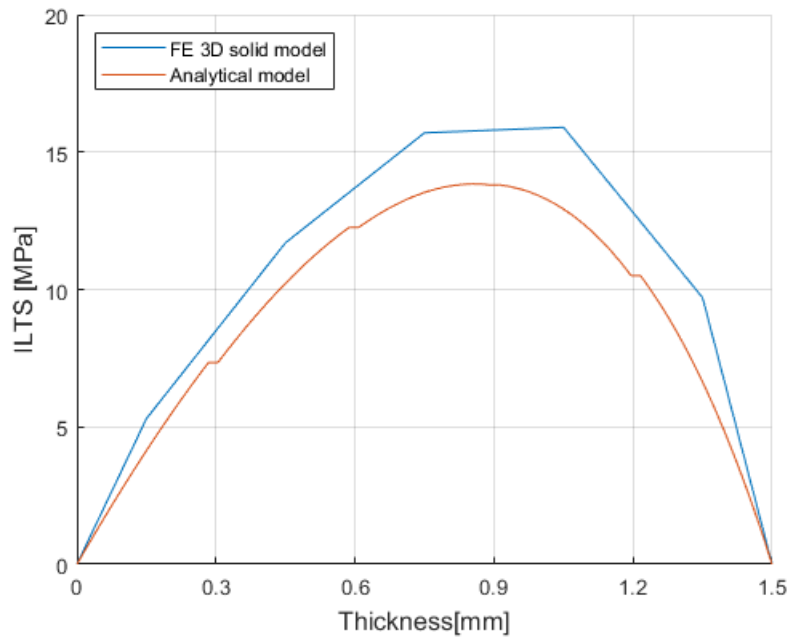
(a)



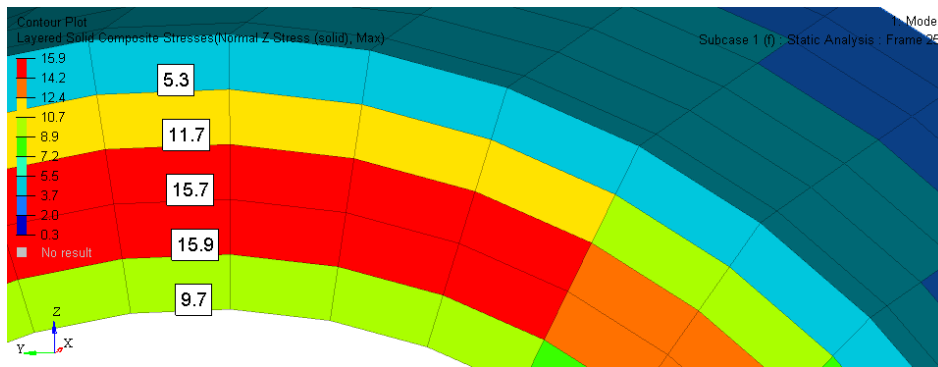
(b)

Figure 75. (a): comparison of ILTS trend along thickness. (b): ILTS result for the 3plies 3D solid model

In Fig 7.6 is represented the comparison between ILTS calculated with a 3D solid model and the one calculated with the analytical model. The model has a 1.5 mm thick laminate and consists of 5 cloths plies at 0° , with 0.3mm thickness each. The analytical model underestimates the maximum ILTS of about 15% but the shape of the distribution agrees with the 3D solid FE model. The parabolic trend of the ILTS presents the maximum not exactly in the middle but shifted to the inner plies (3rd and 4th layer).



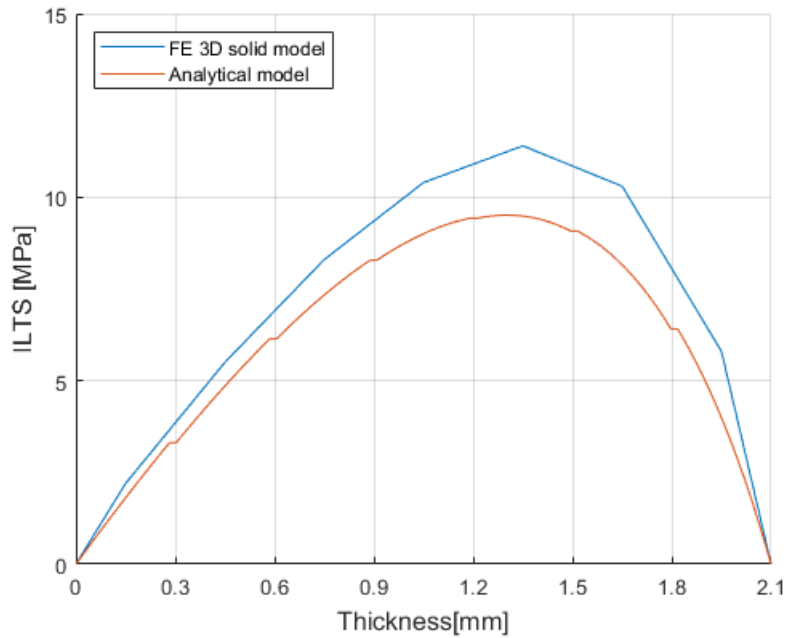
(a)



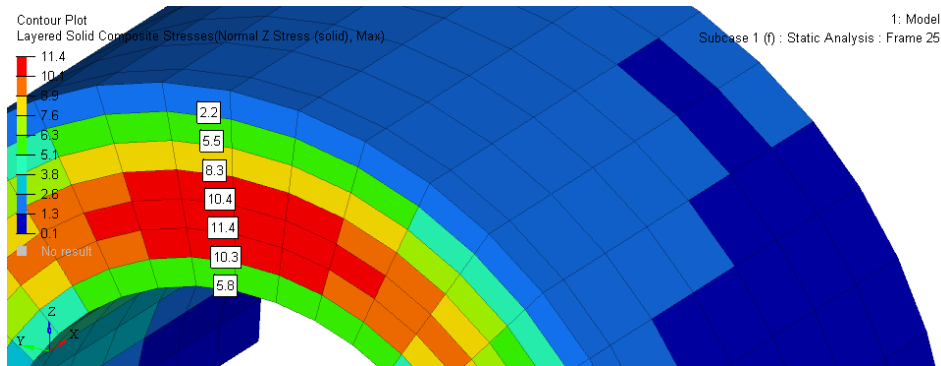
(b)

Figure 7.6. (a): comparison of ILTS trend along thickness. (b): ILTS result for the 5plies 3D solid model

In Fig 7.7 is represented the contour plot of the ILTS calculated by the 3D solid model, the section is a cut through the middle of the semi cylinder. The FE model representing a 7 plies laminate with a total thickness of 2.1mm (2.4 Radius/thickness ratio) is composed by 0.3mm thick cloths plies oriented at 45°. the maximum ILTS lies among the 4th, 5th and 6th plies as can be seen in Fig 7.7. the analytical model follows the 3D solid FE model trend with a maximum error of 12% of underestimation.



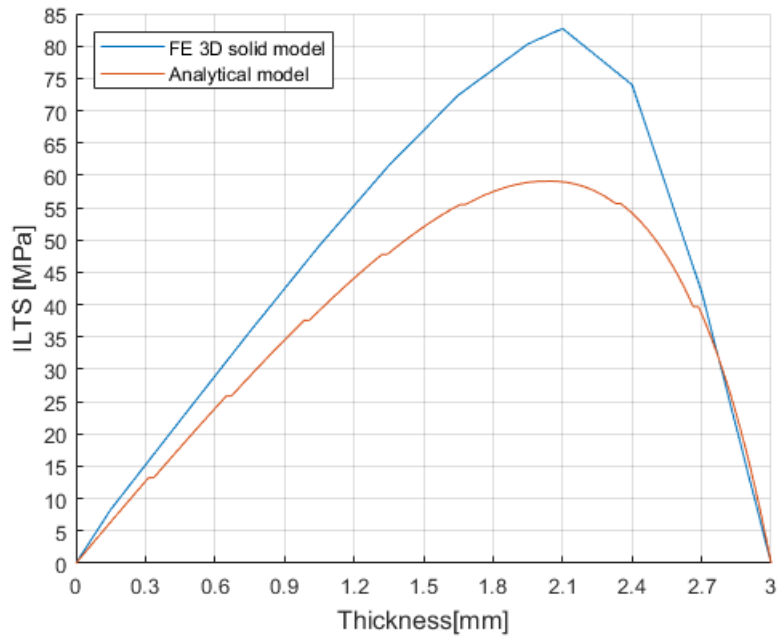
(a)



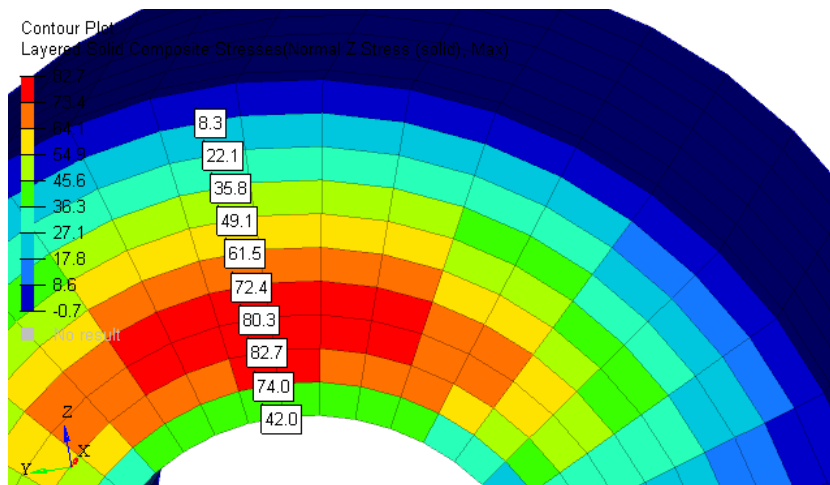
(b)

Figure 7.7. (a): comparison of ILTS trend along thickness. (b): ILTS result for the 7plies 3D solid model

In the case of a thick laminate with a 1.7 geometric curvature / thickness ratio the maximum error on ILTS increases till around 26% of underestimation. In Fig. 7.8 is shown the comparison for the ILTS calculation for a 10 plies FE model. The total thickness is 3 mm and the laminate is composed by 0.3mm thick plies of cloths at 45° . the parabolic trend of the ILTS is not symmetric and the maximum value can be found around the 7th and the ply.



(a)

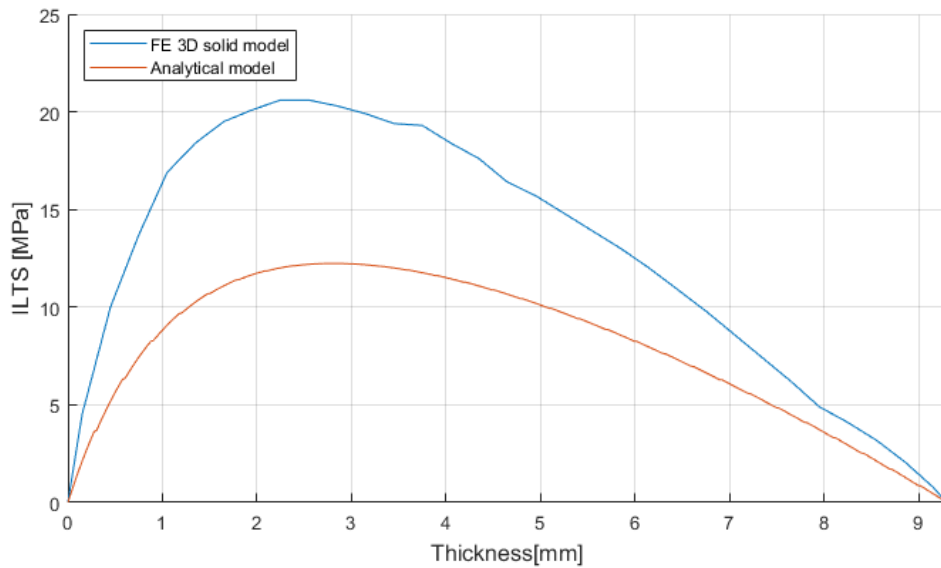


(b)

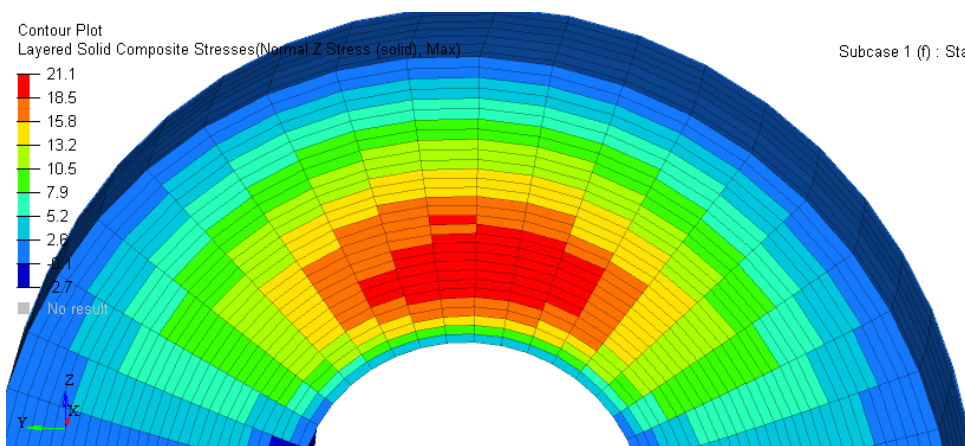
Figure 7.8. (a): comparison of ILTS trend along thickness. (b): ILTS result for the 10plies 3D solid model

In the end, the most severe FE model that has been tested has as main feature a 0.5 geometric curvature/thickness ratio. The semi cylinder has a radius of 5mm while the laminate has an overall thickness of 9.3 mm, it consists of 31 ply of 0.3mm thickness each. The plies are cloth all oriented at 0°. The laminate grows on the outside of the semi cylinder. This represents the worst case in term of ILTS estimation error, indeed the analytical model suffers a 38% error with respect to the 3D FE solid model. The parabolic trend of the ILTS calculated by the analytical model, despite the lack of

precision in terms of magnitude, agrees with the 3D solid model. In Fig. 7.9 are represented the two trends of ILTS. The maximum is located among the 7th, 8th and 9th plies for both models.



(a)



(b)

Figure 7.9. (a): comparison of ILTS trend along thickness. (b) : ILTS result for the 31plies 3D solid model

7.1.4 Single geometric curvature FE Test: Minimum integration points

One of the features of the analytical model that is customizable is the choice of the number of integration point for the finite difference calculation. Here are shown the results of a test with the aim to assess the minimum number of integration points to gain an acceptable level of precision. The test was done on a wide range of FE models calculation (around 100 FE models, between single and double geometric curvature), from ones with a small radius/ Laminate thickness ratio to the ones also far from reality . The result can be observed in Fig. 7.10 where the average of all results is plotted. After a number of around 10 points of integration for each layer there is no more gain in precision even in laminates with a big amount of layers.

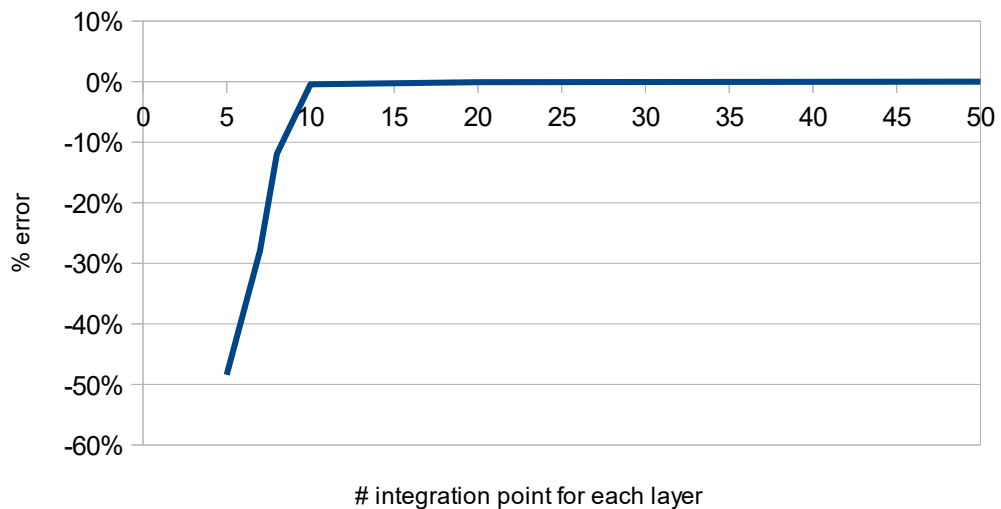


Figure 7.10. trend of the error of ILTS calculation respect to the number of integration points

7.1.5 Single geometric curvature FE Test: Non-aligned mesh

The models presented until now have in common a mesh aligned with the principal geometric curvature radius. The analytical model is tested on a random mesh. The baseline geometry is the semi cylinder of 5mm radius previously used. The laminate is made of 5 layers mixed $[45^\circ/0^\circ]$ cloth plies of 0.2 mm thickness each, the total thickness is 1.0 mm and the radius/thickness ratio is 5. The maximum of the ILTS lies around the middle of the laminate as can be seen by the 3D solid FE model in Fig. 7.11. The maximum ILTS is underestimated by 16 % as for the aligned mesh. The maximum ILTS area is less similar to the 3D solid model in the non aligned mesh.

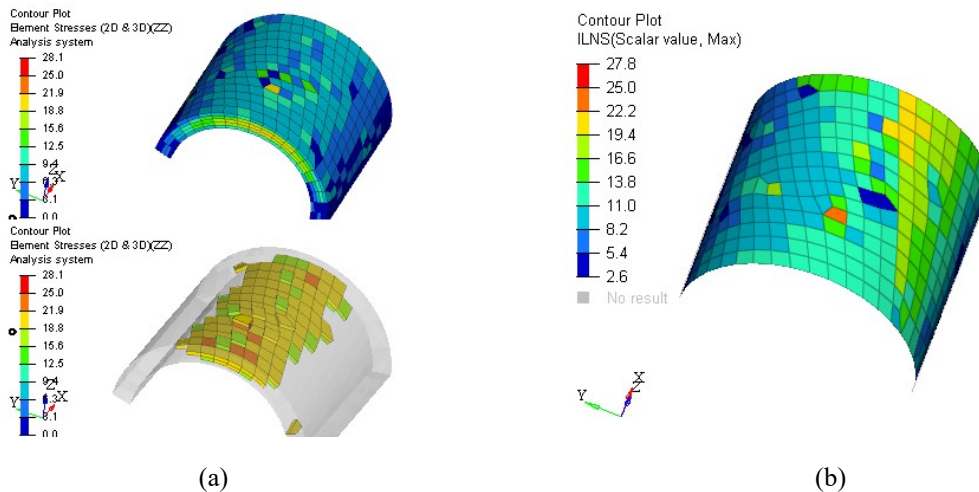


Figure 7.11. Results comparison of ILTS on a non-aligned mesh. (a): the 3D solid model results, (b): the 2D model with the analytical model results.

7.1.6 Single geometric curvature FE Test: Angled anisotropic plies

The post processing method is tested with highly anisotropic laminates. The aim is to check the precision of the analytical model in calculating the ILTS with extreme stiffness matrix. The Geometry is a semi cylinder of 5 mm Radius. The laminate thickness is 2.1 mm in total, and consist of 7 plies of UD's of 0.3 mm thickness each. Several tests are performed with all the UD's angled by the same angle. The range extends from 0° laminate, aligned along X to 90° laminate aligned along Y. Te applied load is 100 N along Y direction, the principal geometric curvature is along Y too. The same configuration (geometry, overall thickness, load, boundary conditions) with a cloth laminate instead, showed a maximum error on the ILTS calculation of around -15% with all the cloths plies at 0°. The results of a highly anisotropic laminate with all UD plies aligned at 0° shows an error of -20% on maximum ILTS calculated by the analytical model respect to the 3D solid model, and an error of -23% with UD plies at 90°. Moreover, the error becomes bigger as the plies have different angles and are not perpendicular to the load direction. In Fig 7.12 are shown as results the maximum error on the ILTS calculation for a wide range of angled UD plies.

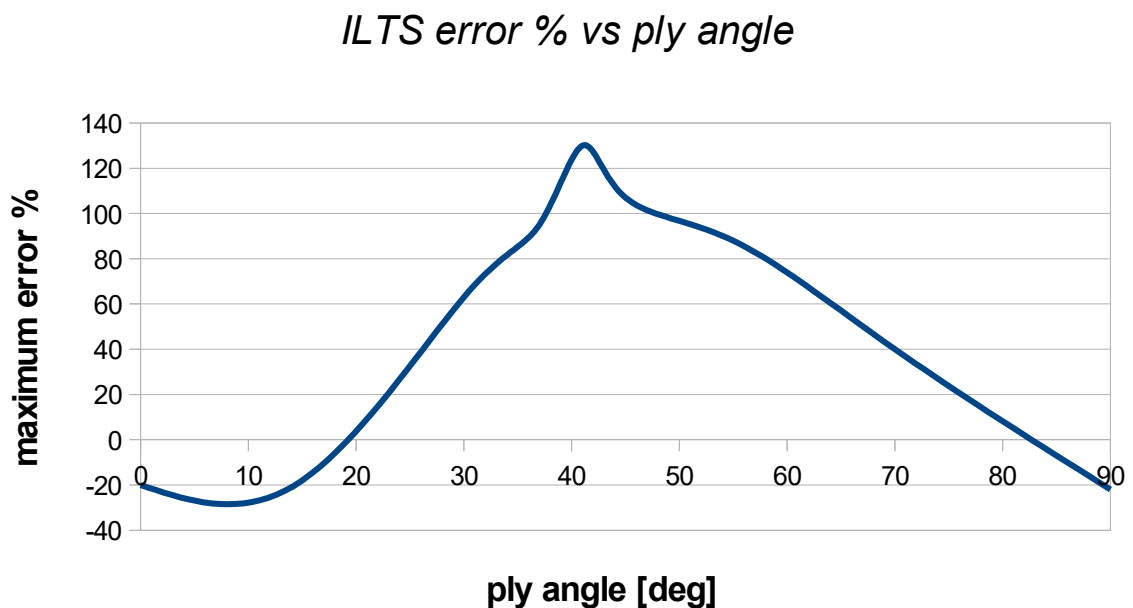


Figure 7.12. Trend curve of error on maximum ILTS value vs laminate orientation

The test highlights a relevant error when plies are angled, when the plies are angled with respect to the reference material direction the error on calculating the maximum ILTS goes from an underestimation as for the cloths laminate one, to a large overestimation. The maximum error is obtained with a 45° angled UD plies, and it became smaller as the plies became to be oriented at 90°, the perpendicular direction to the curvature. There are at least three features of the analytical model that could lead to this miscalculation of the ILTS for 45° angled UD plies. One is the absence of the shear stress τ_{12} in the equilibrium equation 17, but as was demonstrated by L. Marchignoli in “Valutazione numerica della componente normale di tensione in un laminato a doppia curvatura”[97] this type of stress does not have a direct influence on the overall ILTS of a component. The second feature is the absence of the interlaminar shear terms in the equilibrium equation, but as demonstrated by Kress et al [87] these stresses have a negligible effect on the overall ILTS calculation. Another feature of the analytical model is the exclusion of the shear terms from the stiffness matrix in the material law eq 22. The point is that in the case of angled plies the stiffness matrix is rotated and the terms that connect shear deformation to the principal normal stresses are not equal to 0. So that the shear in-plane deformation γ_{12} plays a role in the finite difference calculation and also directly in the calculation of the ILTS. The analytical model is then updated with the introduction of the in plane shear deformations.

8. Enhancing model: introducing in - plane deformations

The post processing analytical model is updated with the introduction of the in plane shear deformation into the calculation for the out of plane displacement through finite difference and also in the calculation of the ILTS. The eq 6.23 of the material law is expressed in its full orthotropic material form as in eq 8.1

$$\begin{pmatrix} \sigma_\varphi \\ \sigma_\theta \\ \sigma_r \\ \tau_{\varphi r} \\ \tau_{\theta r} \\ \tau_{\varphi\theta} \end{pmatrix} = \begin{pmatrix} C_{11} & C_{12} & C_{13} & 0 & 0 & C_{16} \\ C_{21} & C_{22} & C_{23} & 0 & 0 & C_{26} \\ C_{31} & C_{32} & C_{33} & 0 & 0 & C_{36} \\ 0 & 0 & 0 & C_{44} & 0 & 0 \\ 0 & 0 & 0 & 0 & C_{55} & 0 \\ C_{61} & C_{62} & C_{63} & 0 & 0 & C_{66} \end{pmatrix} \begin{pmatrix} \varepsilon_\varphi \\ \varepsilon_\theta \\ \varepsilon_r \\ \gamma_{\varphi r} \\ \gamma_{\theta r} \\ \gamma_{\varphi\theta} \end{pmatrix} \quad \text{Eq. 8.1}$$

When the ply principal direction of orthotropy is angled the stiffness matrix is rotated and the terms relating the normal stresses to the in plane shear deformation are not equal to 0 anymore. The eq 8.1 could be written in a short form as in eq 8.2.

$$\begin{pmatrix} \sigma_\varphi \\ \sigma_\theta \\ \sigma_r \end{pmatrix} = \begin{pmatrix} C_{11} & C_{12} & C_{13} & C_{16} \\ C_{21} & C_{22} & C_{23} & C_{26} \\ C_{31} & C_{32} & C_{33} & C_{36} \end{pmatrix} \begin{pmatrix} \varepsilon_\varphi \\ \varepsilon_\theta \\ \varepsilon_r \\ \gamma_{\varphi\theta} \end{pmatrix} \quad \text{Eq. 8.2}$$

As consequence the eq 6.18 can be updated into eq 8.3

$$\begin{aligned} \sigma_\varphi &= \frac{C_{11}}{r} \left(w + \frac{\partial u}{\partial \varphi} \right) + \frac{C_{12}}{r+D} \left(w + \frac{\partial v}{\partial \theta} \right) + C_{13} \frac{\partial w}{\partial r} + C_{16} \gamma_{\varphi\theta} \\ \sigma_\theta &= \frac{C_{21}}{r} \left(w + \frac{\partial u}{\partial \varphi} \right) + \frac{C_{22}}{r+D} \left(w + \frac{\partial v}{\partial \theta} \right) + C_{23} \frac{\partial w}{\partial r} + C_{26} \gamma_{\varphi\theta} \end{aligned} \quad \text{Eq. 8.3}$$

$$\sigma_r = \frac{C_{13}}{r} \left(w + \frac{\partial u}{\partial \varphi} \right) + \frac{C_{23}}{r+D} \left(w + \frac{\partial v}{\partial \theta} \right) + C_{33} \frac{\partial w}{\partial r} + C_{36} \gamma_{\varphi\theta}$$

Where $\gamma_{\varphi\theta}$ can be expressed as in eq 8.4.

$$\gamma_{\varphi\theta} = \frac{1}{2r} \left(\frac{1}{\cos\varphi} \frac{\partial u}{\partial \theta} + v \tan\varphi + \frac{\partial v}{\partial \varphi} \right) = \frac{1}{2r} \left(\frac{\partial u}{\partial \theta} + \frac{\partial v}{\partial \varphi} \right) = \frac{RI}{r} (\gamma^0 + (r-RI)k_\gamma) \quad \text{Eq. 8.4}$$

Where the term tangent of φ becomes equal to zero

Combining the updated material law (eq 8.2) and the equilibrium equation 8.3 is obtained a second order differential equation expressed by eq 8.5

$$\begin{aligned} 0 = & C_{33} \frac{\partial w}{\partial r^2} + \frac{\partial w}{\partial r} C_{33} \left(\frac{1}{r} + \frac{1}{r+D} \right) \\ & + w \left[-\left(\frac{C_{11}}{r^2} \right) - \left(\frac{C_{22}}{(r+D)^2} \right) + \frac{(C_{32}+C_{31})}{r(r+D)} - 2C_{12} \right] \\ & + u_\varphi \left[-\left(\frac{C_{11}}{r^2} \right) + \frac{(C_{31}+C_{21})}{r(r+D)} \right] + v_\theta \left[-\left(\frac{C_{22}}{(r+D)^2} \right) + \frac{(C_{32}+C_{11})}{r(r+D)} \right] \\ & + \frac{\partial u_\varphi}{\partial r} C_{31} + \frac{\partial v_\theta}{\partial (r+D)} C_{32} - \frac{C_{36}}{r^2} \gamma_{\varphi\theta} \\ & + \frac{(C_{36}-C_{26})}{(r+D)} \gamma_{\varphi\theta} + \frac{(C_{36}-C_{16})}{(r)} \gamma_{\varphi\theta} + \frac{\partial \gamma_{\varphi\theta}}{\partial r} C_{36} \end{aligned} \quad \text{Eq. 8.5}$$

The second order differential equation now takes into account an the effect of in plane shear deformation. The differential equation can be solved through the finite difference method with the same features previously illustrated in chapter 6.4.

9. Enhanced analytical model: test results

The post processing analytical model, with the update regarding the in plane shear terms is then tested again on a single geometric curvature geometry and compared to the previous analytical model and the 3D solid FE model. The range of angled plies goes from 0° to 90° . In Fig 9.1 are shown the main results in terms of error on maximum ILTS calculated with the analytical postprocessing model respect to the corresponding 3D FE solid model. Removing the exclusion of the shear terms from the stiffness matrix has the result of a better behavior of the analytical model. It presents now a consistent error of maximum ILTS placed in the range -20% / -13% which is acceptable also compared to the big amount of error of the previous version.

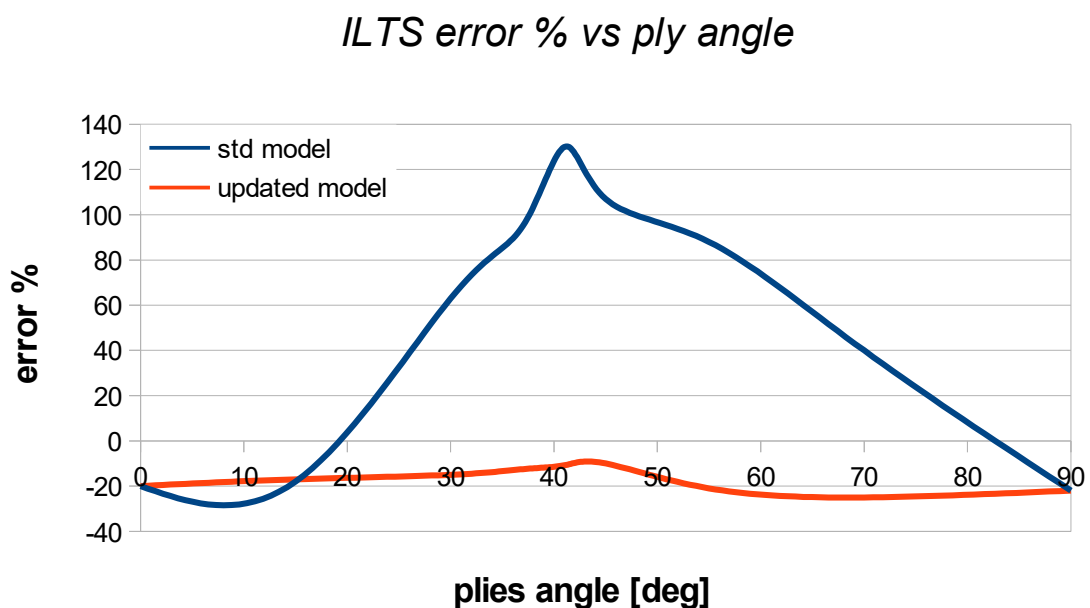


Figure 9.1. Comparison of error on maximum ILTS value trend vs laminate orientation between the simple

In Fig 9.2 are represented the ILTS distribution of three examples of angled ply laminate: a 15° , 45° and 70° laminate. On the right there are the results obtained from

the postprocessing analytical model calculated from the 2D FE model results. On the left there are the results of the 3D FE solid model, these are iso cut to better show the distribution of the ILTS which is maximum in the inside of the laminate. While the 2D results show directly the maximum values for each element.

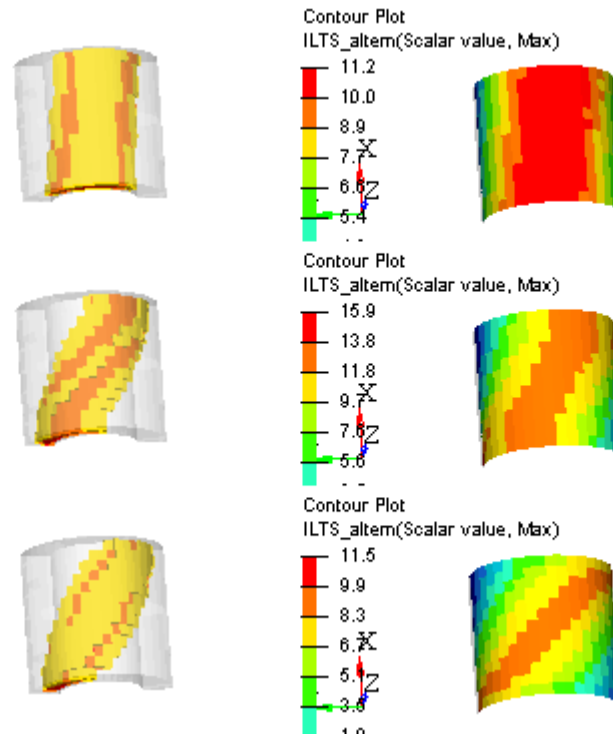


Figure 9.2. Comparison of ILTS distribution among three different ply orientation laminate: 15°, 45° and 70°

The distribution of ILTS calculated by the analytical model agrees with the 3D solid model, indeed the maximum ILTS area is rotated by a certain amount respect to the principal axes X and Y, it is placed perpendicular to the plies angle.

10. Double geometric curvature FE Test

The post processing analytical model exhibited the tendency to underestimate the value of the maximum ILTS but with consistency. It is worth to test it on a double curved geometry. The test consist (as per the single geometric curvature geometry) in a comparison between the 2D shell results and the 3D solid FE model results. The ultimate purpose is to test it on a Formula 1 FE model of a Front wing, so the process is to test the analytical model on geometries with increasing difficult features.

10.1 Double geometric curvature FE Test: Spherical Cap

The first test is performed on a simple double geometric curvature geometry. A spherical cap where both principal geometric curvature radii $R1$ and $R2$ measure 54mm is meshed with 2D linear shell 4nodes elements. The average mesh size is around 1.5mm and the mesh is aligned with the two principal geometric curvature radii. The cap chords are not equal, indeed one measures 31mm along Y and the other 54 mm along X. the edge nodes of the short side are linked together with two rigid links (RBE2 in Optistruct) as in Fig. 10.1.

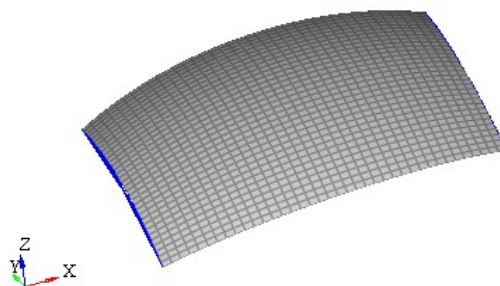


Figure 10.1. 2D FE model representation of the spherical cap.

The elements have their normal inward and the material reference direction is along the X axis for all the elements. One rigid link is constrained in all its DoF while on the other is applied a Force of 100N along x+. the laminate has an overall thickness of 5 mm and is made by 5 plies of 1mm thickness each. Consequentially the 3D solid model has 5 elements through-the-thickness with the same thickness. The material used to represent cloths plies was already shown in table 1 as for the material used to represent UD plies has its material properties shown in table 2. Two types of stacking sequence are tested:

- All 0° cloths
- All 45° cloths

The single geometry curvature FE model was tested also with a combined laminate [0/45° cloths]. Since the results obtained by this kind of laminate layup are in the middle between the results of the all 0° cloths and all 45° cloths laminates, it has been dismissed. The results (in Fig. 10.2) indicate that the model suffers from edge effects, but excluding the elements on the edge, a couple of conclusions can be extracted. The post processing analytical model is able to catch the ILTS distribution on the geometry exhibited by the 3D solid FE model.

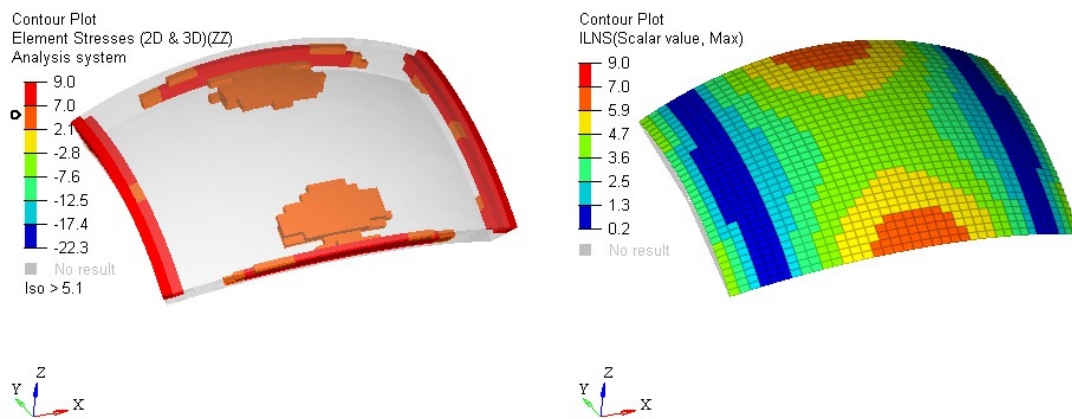


Figure 10.2. Comparison of ILTS distribution and values between 3D solid model and 2D FE model with analytical ILTS calculation

The error on the maximum ILTS is around +10% for a laminate with 0° cloth and -16% for a laminate of 45° cloths. In fig 10.3 is shown the ILTS distribution along the

laminate thickness with the help of the 3D solid model and the comparison with the analytical model results. The maximum peak is for both models in the middle of the laminate but the 3D solid model presents a larger area of high ILTS respect to the analytical model which let the ILTS decrease early.

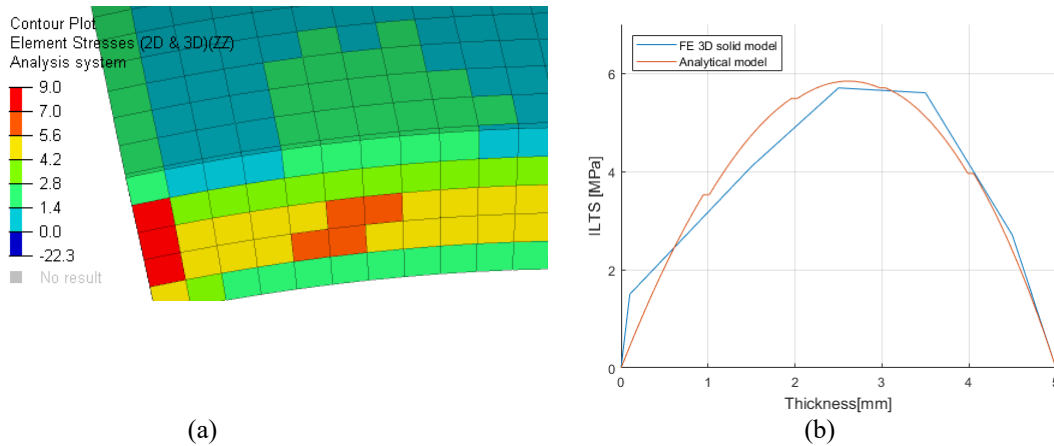


Figure 10.3. (a): ILTS results of 3D model through-the-thickness. (b): comparison between 3D model and analytical model ILTS results through-the-thickness

10.2 Double geometric curvature FE Test: Double elbow tube

The second model presents a more complex geometry, the aim of this test is to challenge the analytical model with a geometry where ILTS is far from free edges and where it could also be negative. The geometry is composed of 2 straight tubes plus two curved 90° connections, which resemble a double elbow connection. The radius of all the tubes is 35mm, and the two straight portions of the geometry are 100mm in length. The straight parts of the geometry extend along X, while the curved part are a rotation of 90° around Y axis. The geometry is meshed with 2S shell 4nodes elements with an average size of 5mm for the straight part and 3mm for the curved parts. The mesh in the curved parts is not aligned with the principal geometric curvature radii. Both ends of the geometry are constrained with rigid links (RBE2 in Optistruct), one end is fixed in all

its DoF and in the other end is applied on the master node of the rigid link a force of 1000N along Z-. The 2D elements have their normal pointed inward the geometry and the material reference direction is imposed to be in cylindrical coordinates along the tangent of the tube. The laminate is made by 10 plies of 0.5 mm thickness each, so that the laminate thickness is 5mm in total. Here below in Fig. 10.4 in shown the 3D FE solid model generated from the 2D shell model. The shell elements are extruded along their normal to create the 10 layer laminate, the height of each solid element is 0.5mm, the material reference direction is imposed to be the same as the 2D shell model.

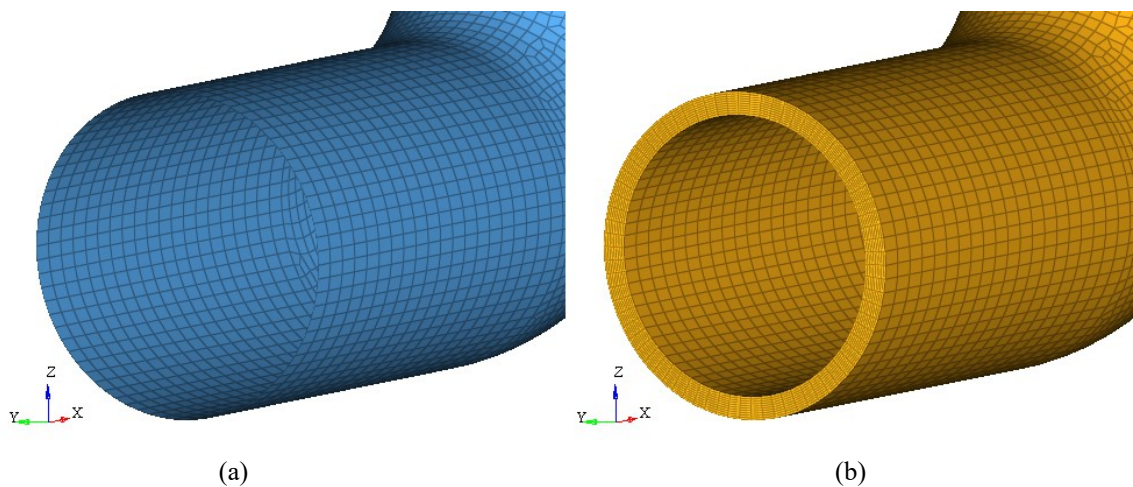


Figure 10.4. (a): 2D shell FE model representation. (b): 3D layered solid model generated from 2D shell model.

Two test with a simple laminate are done

- 10 cloth plies at 0°
- 10 cloth plies at 45°

The results of the post processing model are compared to the 3D solid model. The error on the maximum ILTS value is around 0% for the 0° laminate and -5% for the 45° laminate. Moreover, the post processing model was able to calculate also negative ILTS of some area.

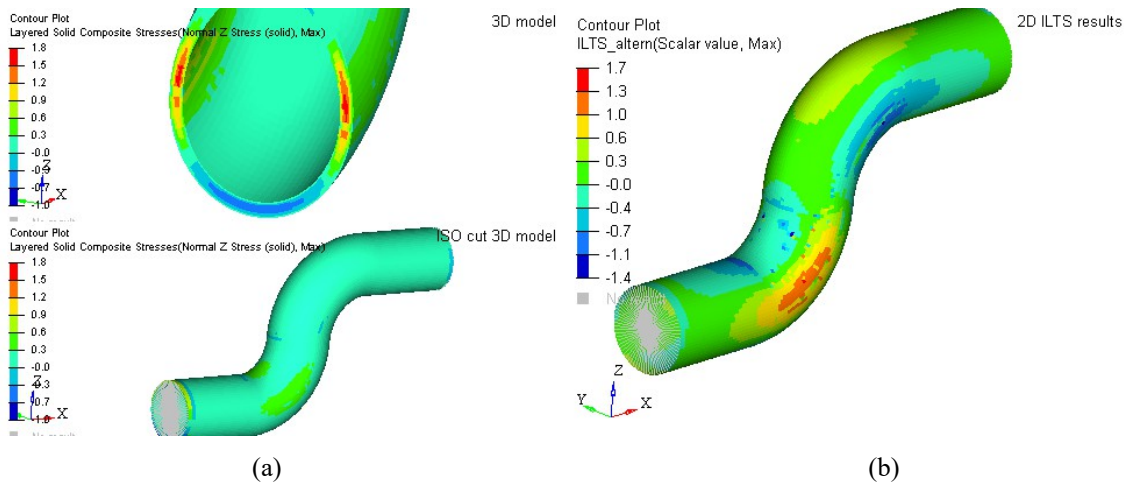


Figure 10.5. (a): 3D solid FE model results, on top a section cut to highlight the ILTS through-the-thickness, on bottom the overall ILTS distribution visible only on the external layer. (b): 2D shell model with ILTS results from analytical model.

In Fig 10.5 are illustrated on leftside the 3D solid model results of the 45° laminate , on bottom there is the overall contour of ILTS while on top the section cut detail of the maximum ILTS area, on right side the results calculated with the post processing model. The analytical models results in terms of ILTS distribution agree with the 3D solid model.

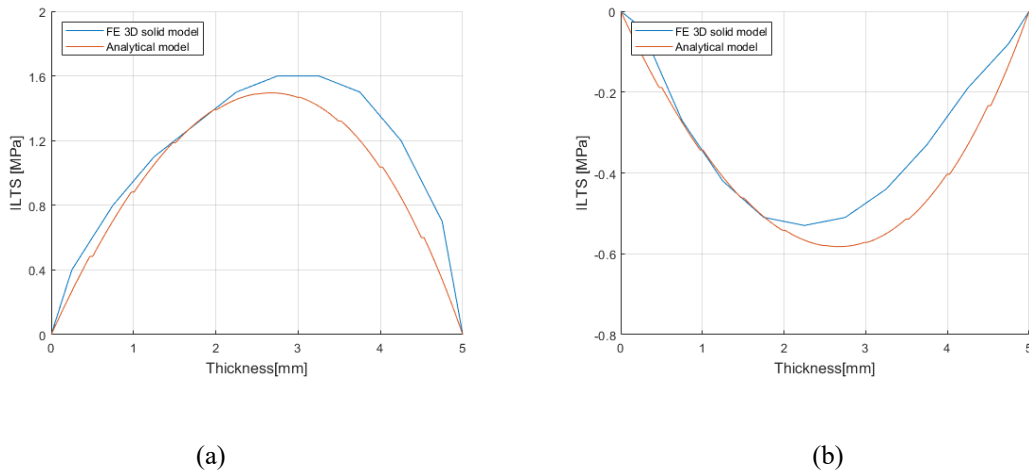


Figure 10.6. (a): ILTS through-the-thickness of the maximum value. (b): ILTS through-the-thickness of the minimum value.

In Fig 10.6 is shown a comparison in case of positive completely ILTS and completely negative ILTS. The maximum value is reached between the 6th and 7th ply in the 3D solid model and is in the middle of the laminate for the analytical model.

10.3 Double geometric curvature FE Test: Change of curvature

The post processing model showed good results in comparison with the 3D solid FE model in terms of distribution over an area, maximum value and distribution along thickness of the ILTS for the two simple tested models. It is now verified on a geometry which main feature is a change of curvature. The geometry is a sweep between two curves, one is a 40mm radius arc of 150° on the ZY plane, the other is composed by 2 arcs on XZ plane. One has a radius of 92.5mm and the other has a radius of 70mm, the two radii have opposed verse and between them there's a fillet that guarantees tangent continuity. This geometry represents a feature that can easily be found in the regular design of composite components. Because of the improvement in technology, it is easier to make molds for composite components with very complicated geometries, this has the effect to push the design to optimal solutions in terms of geometry efficiency.

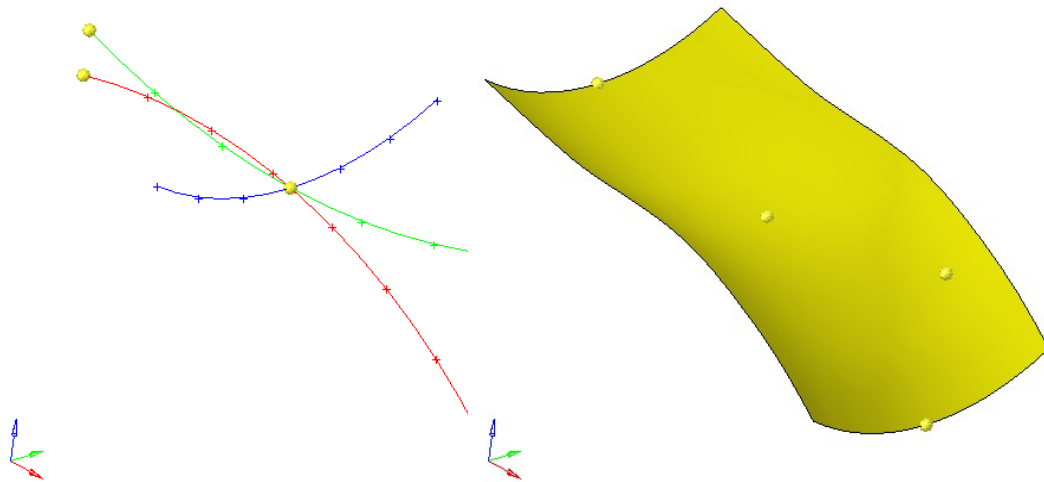


Figure 10.7. Double Geometry curvature: construction of the surface

In Fig. 10.7 are illustrated the 3 base arcs constituting the main geometry on the left. In blue the R 40mm arc that has been used for the sweep along the intersection of the red R 92.5 arc and the green R 70 mm arc. On the left is represented the resultant of the sweep.

The mesh is not completely aligned with the principal geometric curvature radii, indeed one of the short edges has an average mesh size of 2.5mm, the other one of 3.5 mm, while one of the long edges has a mesh size of 2 mm and the opposite of 3mm in order to generate a slightly distorted mesh as often happens in components with a certain complexity. The mesh is composed of linear shell elements (CQUAD/ CTRIA of Optistruct). The long edges are constrained with rigid links (RBE2). One has all its DoF fixed, while on the other one is applied a displacement of 5mm along Y+, the displacements in X and Z are fixed. This geometry is not exempt from free edges effect but the main point is to test the behavior of the analytical model on a change of geometric curvature in a double geometric curvature surface. The elements have the normal imposed to be in Z-, and the material reference direction is set along Y for all of them.

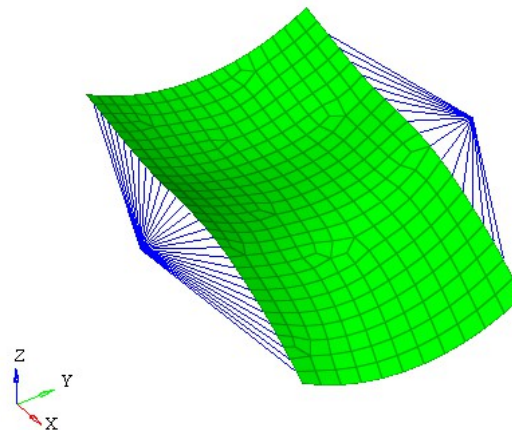


Figure 10.8. 2D FE model representation

The 3D solid model is created extruding the 2D shell elements along their normal

direction. The material reference direction for the 3D model is set along Y, while the Z direction of each element is along the extrusion direction. Moreover are generated several models with different thickness in order to test a wide range of geometric curvature/ laminate thickness ratio (C/LT ratio). The solid elements are linear CHEXA in Optistruct, to define the laminate is assigned a PCOMPLS property to all the solid elements.

In Fig. 10.9 are shown 4 different geometric curvature/ Laminate Thickness (C/LT) models. The ratio is calculated respect to the smallest Radius of the surface, in this case $R = 40\text{mm}$.

They represent.

- 33 C/LT ratio, 1.2 mm laminate made by 6x 0.2 mm plies
- 10 C/LT ratio, 4.0 mm laminate made by 10 x 0.4 mm plies
- 5 C/LT ratio, 8.0 mm laminate made by 20 x 0.4 mm plies
- 2 C/LT ratio, 20.0 mm laminate made by 20 x 1 mm plies

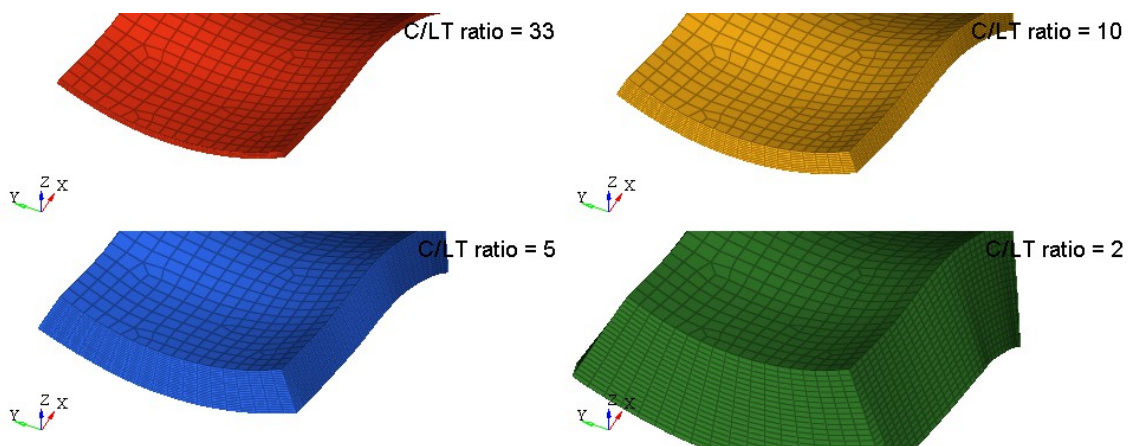


Figure 10.9. Different C/LT ratio illustrated with 3D layered solid model

The first screening test is done on a wide range on C/LT ratio with two simple orthotropic laminates:

- All plies as cloths at 0°
- All plies as cloths at 45°

The cloth material properties are indicated in table 1.

The results obtained with the postprocessing model are compared to the respective 3D solid FE model in terms of distribution of the ILTS on surface, along the thickness and the maximum value. Extreme values on free edges are excluded from the comparison as they are depending on multiple factors.

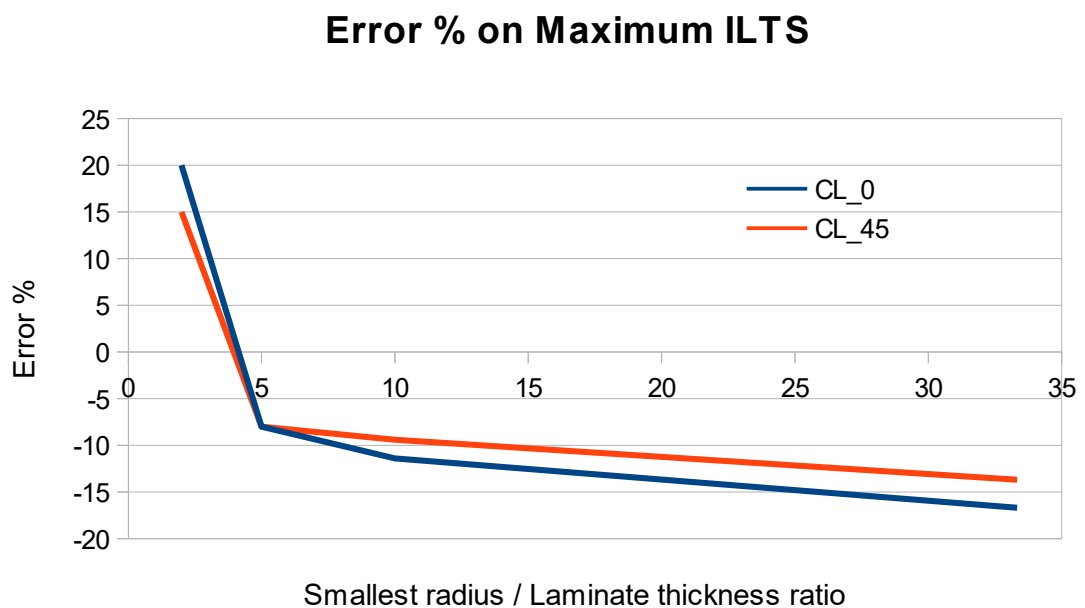


Figure 10.10. Error % on maximum ILTS value calculated by analytical model respect to 3D solid model results

The comparison of the maximum ILTS value shows a good agreement between analytical and 3D solid model (Fig. 10.10), indeed the analytical postproc model tends to underestimate the maximum ILTS for a wide range between 5 and 33 radius/laminate thickness ratio. The underestimation respect to the 3D solid model floats between -10% and -15%. The opposite for very thick laminates in the range 5-2 geometric curvature radius/ thickness, where, however the error is around a maximum of 20% of

overestimation which could be acceptable.

The ILTS distribution on the component is compared between the models. The Fig. 10.11 illustrates the ILTS results of a 4 mm laminate with 10 cloths of 0.4mm each of thickness oriented at 0° . The analytical model (on the right) has quite a good prediction on the area of interest. The change of geometric curvature seems to not be an issue for the post processing ILTS calculation. The 3D model ILTS results are cut with an ISO to better show the most stressed area which is in the middle of the laminate, while the analytical model shows only the maximum value of each element representing the surface.

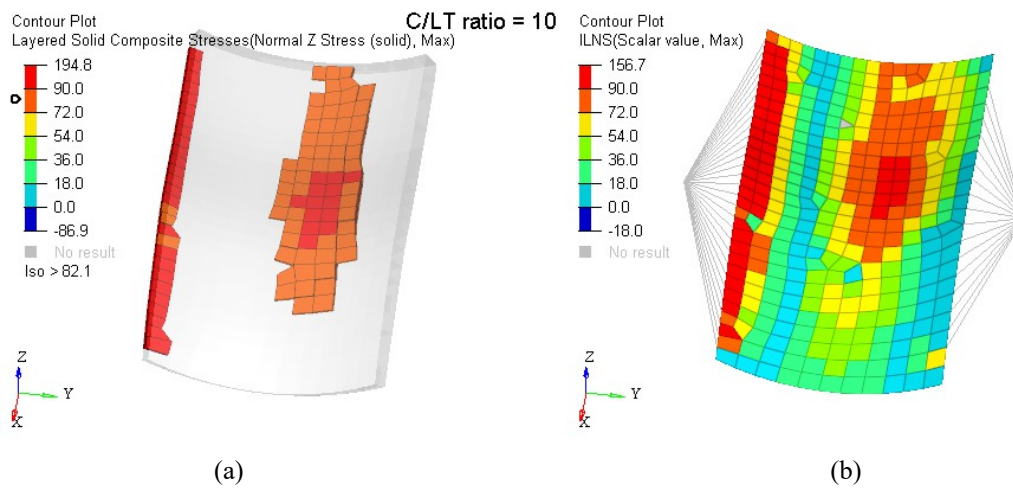
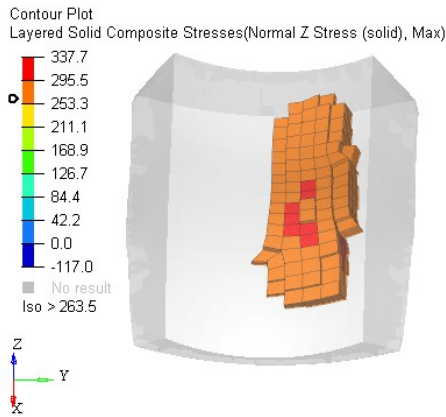
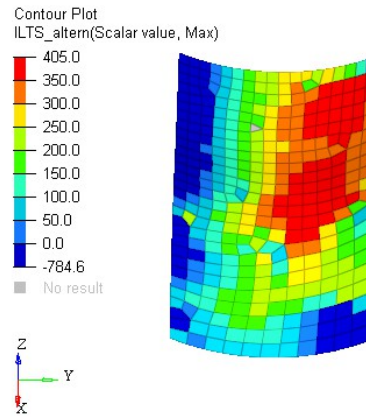


Figure 10.11. 4mm laminate thickness. (a): ILTS results of 3D solid model. (b): 2D Fem model with ILTS calculated with analytical model.

The biggest error on the maximum ILTS value has been obtained at 2 radius/laminate thickness ratio, with a 20mm thickness laminate on the R 40 mm radius. However the distribution of ILTS calculated with the post processing model agrees with the 3D solid model one as in Fig. 10.12.



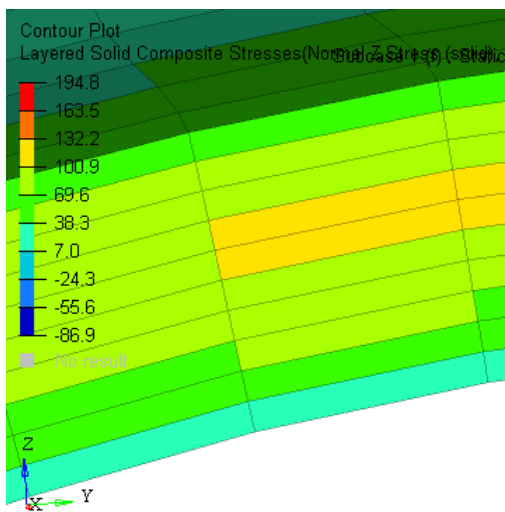
(a)



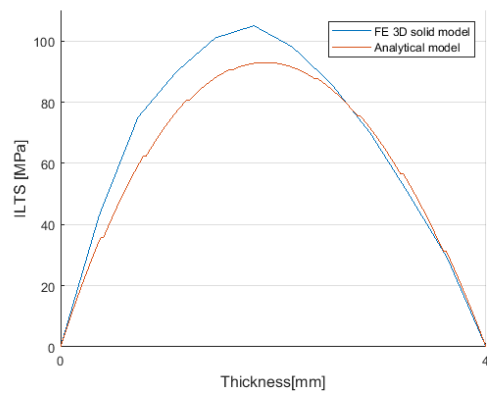
(b)

Figure 10.12. 48 mm laminate thickness. (a): ILTS results of 3D solid model. (b): 2D Fem model with ILTS calculated with analytical model.

Besides, has been done a comparison between the 3D solid model and the analytical model for the ability to catch the distribution along the laminate thickness of the ILTS. The best agreement of the analytical model respect to the 3D solid model is achieved with a C/LT ratio of 10 while the worst correlation has been observed with big thicknesses and a C/LT ratio of 2. Indeed in Fig. 10.13 is represented the comparison for a C/LT ratio of 10, on the left is shown the ILTS distribution of the 3D solid model, on the right is illustrated the comparison with the post processing model. The maximum ILTS is not centered in the middle of the laminate but is slightly moved toward the top of the laminate for both the models.



(a)



(b)

Figure 10.13. 4 mm laminate thickness. (a): ILTS results of 3D solid model. (b): through-the-thickness ILTS comparison

On the contrary there is no such good agreement between the model for a C/LT ratio of 2, as shown in Fig. 10.14, and this is also a consequence of a worse correlation in terms of magnitude. The maximum ILTS should be placed between the 7th and 8th ply as for the 3D solid model, while the post processing model calculates it almost in the middle of the 20 plies laminate.

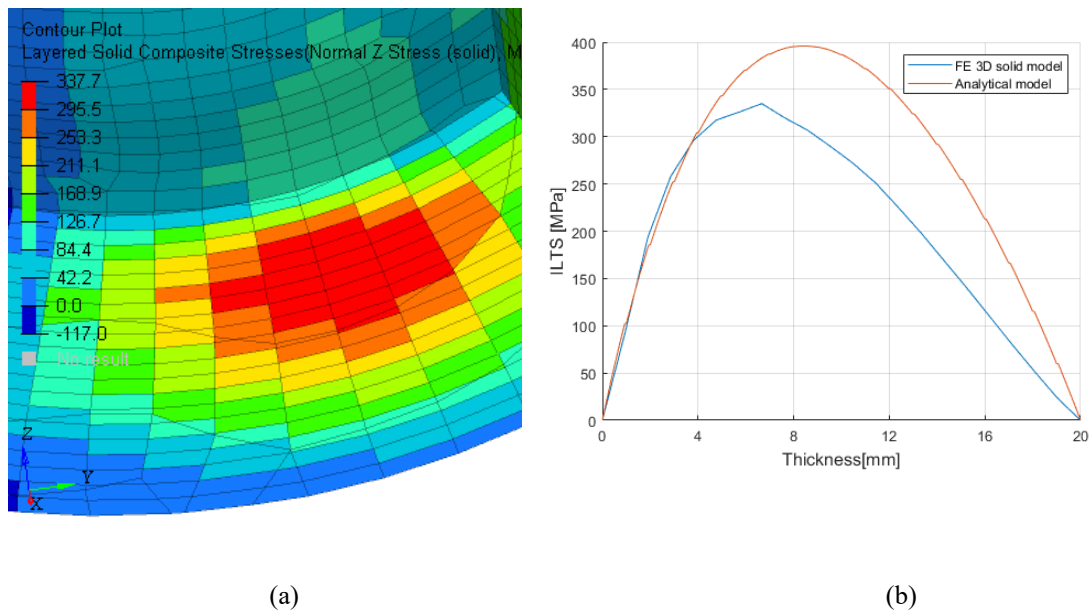


Figure 10.14. 20 mm laminate thickness. (a): ILTS results of 3D solid model. (b): through-the-thickness ILTS comparison

The results obtained with the post processing analytical model with the orthotropic material are in good agreement with the 3D solid FE model. The test continues with an analysis of a more anisotropic material. The baseline model is the 4mm laminate thickness made by 10 plies. The material properties of the UD used to compose the laminate are shown in table 2, the UDs are all oriented with the same angle to keep the laminate highly anisotropic. Moreover, a range of orientation between 0° and 90° is tested. The error on the maximum ILTS value does not exceed 15%, indeed it floats between -5% and +15% as displayed in Fig. 10.15.

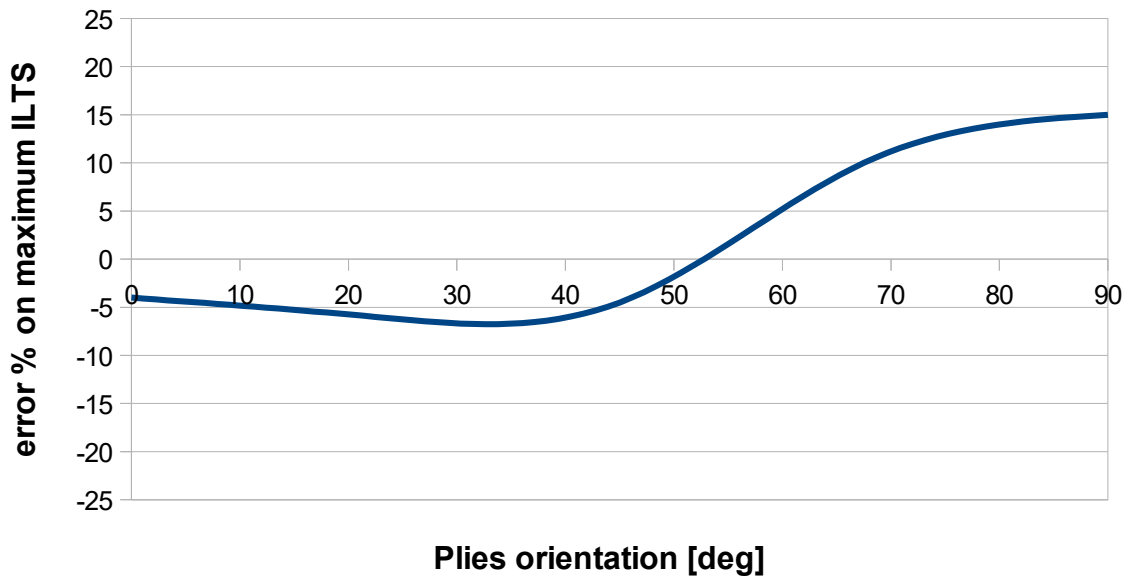


Figure 10.15. error % on maximum ILTS value calculated with analytical model respect to 3D solid model. Trend of error with different angled laminates.

In Fig. 10.16 can be compared the ILTS result on the 2D FE model calculated with the postprocessing method against the 3D solid model. The analytical model is in good agreement with the 3D solid model regarding the ILTS distribution on the geometry apart from some isolated elements.

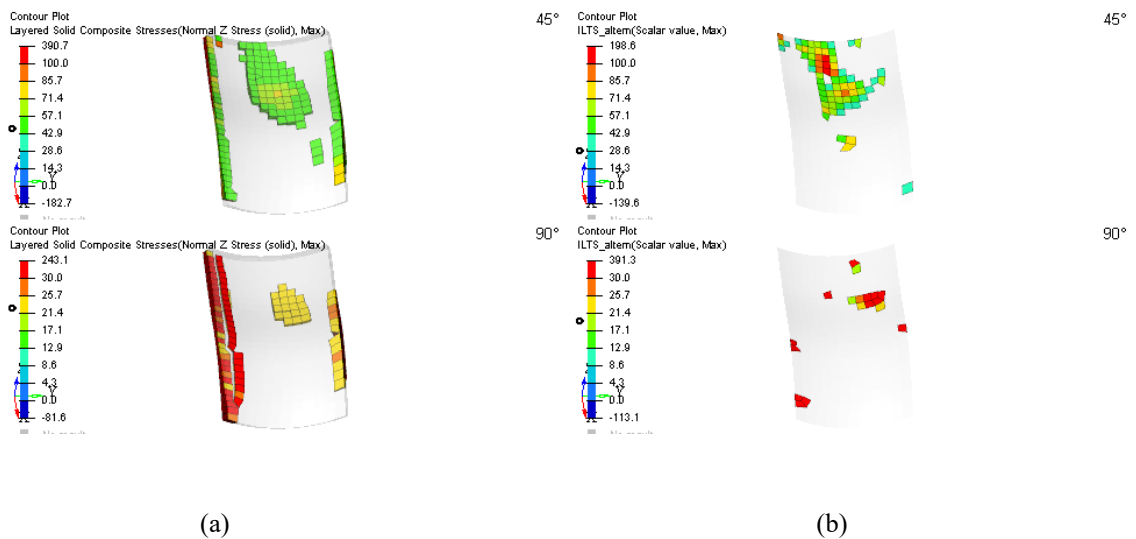


Figure 10.16. ILTS results: distribution.. (a): ILTS results of 3D solid model. (b): analytical model.

11. Single geometric curvature FE Test: deformative curvature purposely not aligned with the principal directions of geometric curvature

The ILTS post processing analytical model revealed able to predict the most critical areas of actual components, with respect to the 3D FE solid model results. Moreover the maximum ILTS values calculated by the analytical model show a consistent discrepancy between -20% and -10% for a wide range of radius/ laminate thickness ratios for the single and double curvature areas of the examined cases. The ILTS through-thickness distribution is in line with 3D results in models with simple geometries and loading condition, in which the possible misalignment of the principal directions of strain with the principal direction of geometric curvature happens to be usually small, or even null in the ETH [3] test cases.

A simple test has been developed to investigate such an issue. The aim is to generate a deformative curvature whose principal directions are 45° inclined with respect to the geometric curvature, in order to maximize the angular discrepancy between those direction. Such a condition is found to be typical of an open, thin-walled (or moderately thick) circular cross section (“C” shaped) profile subject to torsion. Also, the lamination has been chosen in order to maximize its unsymmetric nature with respect to the midsurface, and the fiber orientation is chosen in order to be highly unsymmetrical with respect to the principal directions of curvature.

The following test consists hence in a single curvature geometry derived as the angular portion of an hollow cylinder with axis along Z direction, whose inner and outer radii are 0.5 mm and 1.5 mm, respectively - thus obtaining a unit thickness to mean radius ratio; an axial extension of 3mm and an angular extension of 350° have been employed in order to let the (limited) boundary layer perturbation to decay before reaching the central gauge area of the model.

The geometry is meshed along the midsurface with 2D quadrilateral elements whose

average size is 0.1mm; the mesh is structured and the element edges are aligned with the principal curvature directions, namely the axial and the circumferential direction.

The two axial extremities of the profile segment are pointwisely kinematically linked in order to force a periodic displacement and rotation field, apart from a nonzero imposed twist; in this way the warping motion predicted by the De Saint Venant torsion is allowed, along with any other assessment induced by the absence of symmetry of the material with respect to the cross sectional plane. Also, the modeled portion is expected to be representative of an infinitely long profile subject to twist.

The actual implementation consists in a rigid body RBE2 link, which kinematically defines the differential twist rotation of the two ends of the modeled profile portion, and a set of multi-point constraints (MPC) which impose to each node of the first end of the profile portion (the highest in the Z axial coordinate) a motion equating the sum of the motions of the correspondent nodes on the second profile end, and on the rotating rigid body, i.e. eq 11.1

$$d = r + e \tag{Eq. 11.1}$$

The condition is the following: the displacement and rotations (d) of the Z+ end of portion nodes is equal to the sum of the RBE (r) plus the Z- end of portion nodes (e) displacement and rotations.

The RBE2 is placed next to the mesh, 1 mm shifted in Z+ with respect to the profile first end, and it affects as many otherwise free (i.e. not connected to elements) dependent nodes as the ones along the cylinder ends. The RBE2 master node is centroidally placed along the beam axis. The actual positioning of the RBE2 within the model is however unimportant.

Fig 12.1 represents the meshed model with the RBE2, and a representative MPC whose imposed kinematic relation may be graphically recognized as follows: displacement and rotations of the green node along the first profile end set equal to the sum of motion of the blue node along the rotating rigid body and of motion of the red node along the second profile end.

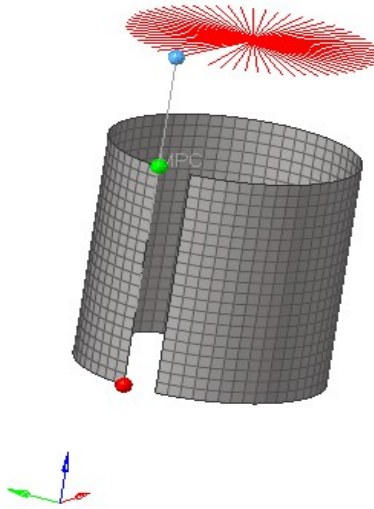


Figure 11.1. 2D shell FE model representation

The master node of the RBE2 is fixed in displacement, the X and Y rotations are constrained to 0, whereas a unit (1 rad) rotation in Z is locally imposed. The actual twist rate is 1 radian over an axial length of 3 mm, but the structural response is linear and all the quantities may be accordingly scaled. The elements' normals are inward oriented, with a inner shell top surface, and an outer shell bottom surface; material orientation is defined with respect to the axial Z direction, so that a 0° oriented unidirectional ply is characterized by axially oriented fibers.

The laminate is composed by 10 plies with a thickness of 0.1 mm each, the offset is null so that the shell elements and the associated nodes are positioned along the midsurface.

The material for all the plies is a UD CFRP composite whose properties are reported in table 2. The first - innermost - five plies are oriented at +45° and remaining - outermost - five plies are oriented at -45°. As told before, the laminate is deliberately non symmetric, non balanced, and designed to exhibit the most general membrane/curvature elastic coupling.

By radially extruding the quadrilateral elements of the shell model a 3d brick model is derived, for comparison. To increase the stress prediction capabilities of this control model, triquadratic 20 nodes hexahedral elements have been employed. A single 3d brick layer has been employed for each lamina. The RBE2 and the MPC links have been

adapted to include the newly generated nodes.

A suitable set of positioning constraints have been added to both the models in order to uniquely position the elastic body, thus inhibiting its residual rigid body motions.

In Fig. 11.2 below the deformed shapes are reported for both the 3D brick and the shell models. This particular test loading condition generates a deforming curvature which is not aligned with the principal curvature of the geometry. Furthermore the ILTS is in compression for a half of the laminate and in tension for the other half.

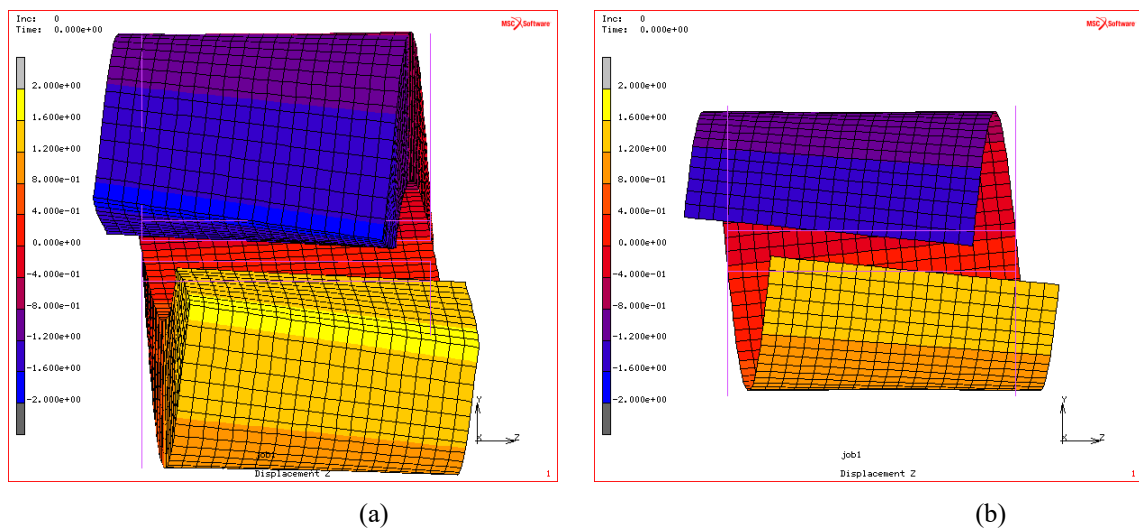


Figure 11.2. Comparison of deformation: (a) the 3D solid FE model, (b): the 2D shell FE model. The contour plot represents the displacement in Z referenced to the global coordinates.

For the single geometric curvature model tested in Cap. 7.1.1 the error on the maximum ILTS calculated by the analytical model was previously illustrated to be around -35%/-38% for a geometry whose geometric curvature radius/ laminate thickness ratio was unity as in the case under scrutiny.

In Fig. 11.3 is represented the ILTS distribution along the laminate thickness. The analytical models (both the basic model and the enhanced one) are able to predict the area of the laminate with the maximum peak of ILTS. But are not capable to catch the ILTS go under the value of 0.0 and become negative.

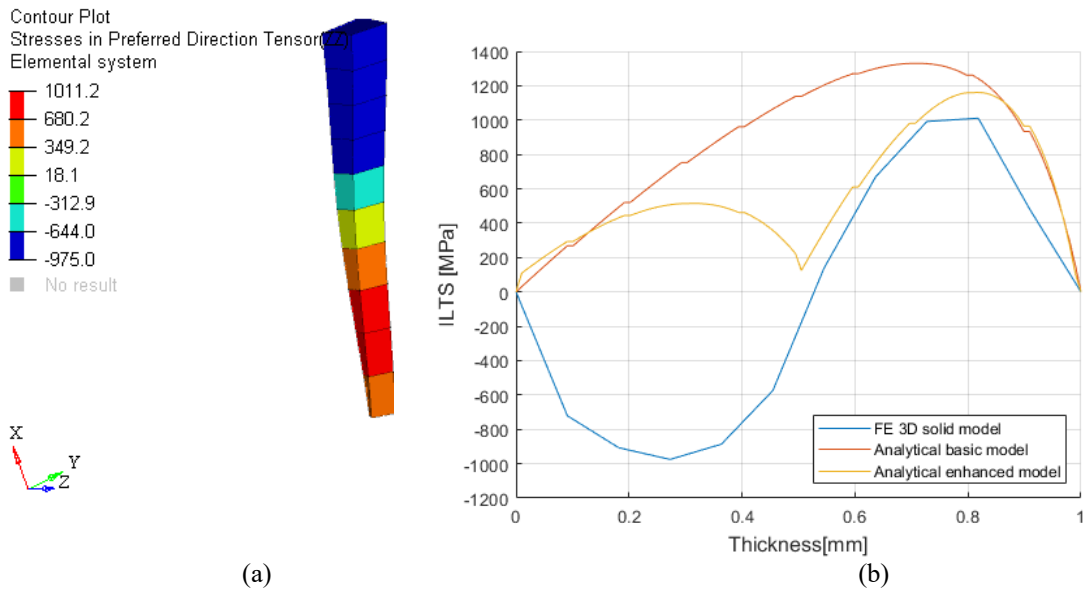


Figure 11.3. (a): 3D model ILTS result along thickness, (b): comparison of ILTS trend through-the-thickness

The ILTS trend through-the-thickness calculated by the 3D solid model presents half of the laminate section in compression and half in traction. The basic analytical model, without in-plane shear deformations included, is not representing the right trend of ILTS, thus the curve presents the usual parabolic shape instead of a double curvature. Moreover, also the enhanced model is incorrect, the ILTS curve has two peaks, which are in agreement with the 3D model about the position through the laminate, but both are positive. The 3D solid model, instead, has one peak (representing the maximum ILTS) positive and one negative peak, the ILTS curve crosses the 0 at around half of the laminate thickness. The enhanced analytical model presents a change of curvature at around half of the laminate thickness and there is no jump of ILTS, which means the interface conditions are not violated, but the whole curve is in the positive dominion of ILTS. Besides, the basic analytical model overestimates the maximum ILTS by 40% respect to the 3D solid model while the enhanced analytical model overestimates it by 11%, which is in contrast to the simple tests done previously.

12. Postprocessing 3D FE model: an alternative to the analytical postprocessing model

The post processing analytical model manifested a relevant issue, the inability to always catch the ILTS trend through-the-thickness. The problem location could be: inside the finite difference implementation or also in the definition of the in plane shear stress $\gamma_{\phi\theta}$, indeed the basic analytical model is far away from the 3D solid model trend curve of ILTS while the enhanced model calculates a double curvature, even if all in positive sign. The finite difference implemented method receives in input the strain from 2D FE model and provides a through-the-thickness displacement. A simple model, combining 2D results and 3D post processing elements, has been implemented to check the quality of the finite difference results. The model is here illustrated on only one element. The objective of this model is basically to create a FE representation of the finite difference model, the difference is the way to submit the input. Thus the combined 2D/3D model has displacement and rotations (which are related to strain) as input.

Starting from the 2D shell FE model, at the element of interest, a shell 4 node in this case, a structure representing an angular section of the laminate is created. Four rigid bars, aligned with the local normal direction, are spawned at the undeformed element vertices. The extension of the rigid bars is equal to the laminate thickness. RBE2 rigid links are employed below to embody those rigid bars. Since in this case there is a non zero curvature, the Bars are not mutually parallel, so they delimit an angular section of the laminate represented by the shell. Then a column of 8 node brick elements is created along such angular section as a morphed extrusion of the underlying shell quadrilateral element. In general, each layer of the laminate could be represented by one or more brick element in the column, in this case there is one brick for every layer. The laminate consists of 10 plies, 5 at -45° and 5 at $+45^\circ$. The material direction and the material properties are assigned at each brick based on the ply it represents. In Fig. 12.1 is illustrated the 3D brick element construction based on the 2D shell finite elements, in

green are represented the bricks extruded from the quadrilateral shell, which is in gray.

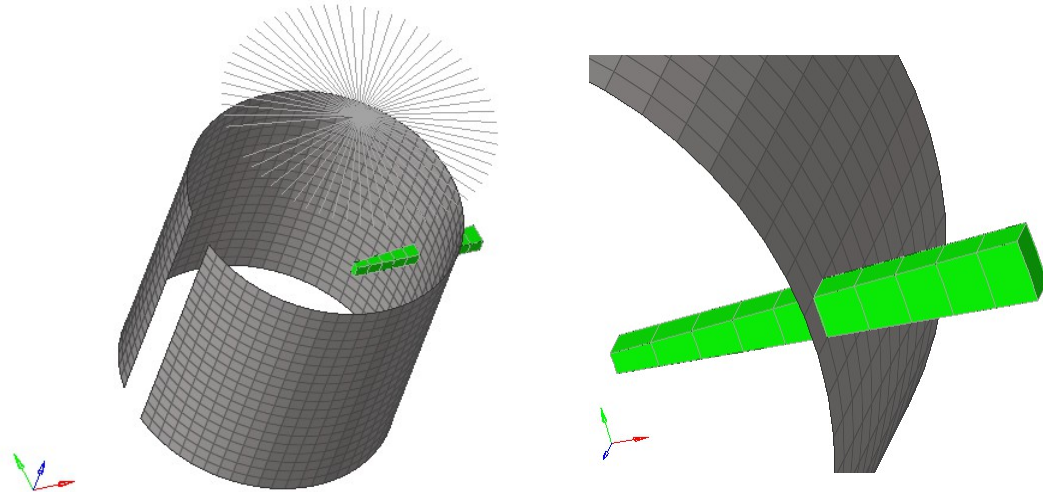


Figure 12.1. 2D/3D model. Original model: In gray 2D shell and RBE2. In green Postprocessing 3D FE solid elements .

The assumption at the base of the analytical model is that the angular section of the curved laminate maintains straight edges during the deformation. The angular section is bounded by straight walls and all the deformations depend only on the displacement along the radius coordinate. Every node of the brick elements is strung to the rigid bars and so is guided in its motion. Indeed the brick nodes on the four edges of the angular section are the slave nodes of the four rigid links, while the four nodes of the quadrilateral element are the masters. Thus the nodes of the bricks element have imposed rotations and imposed displacements except the displacement through-the-thickness. Furthermore, not mandatory, the normal displacements of the four nodes pertaining to the same layer boundary may be linked to a common normal displacement value. Such a constraint reduces the number of actual unknowns matching that of the finite difference procedures. In Fig. 12.2 are highlighted in red the rigid links connecting the bricks nodal displacements and rotation (for the exception of the through-the-thickness displacement) to the 2D shell ones, indeed the links are keeping the brick edges straight in line as required by the thick-walled kinematic relations [98].

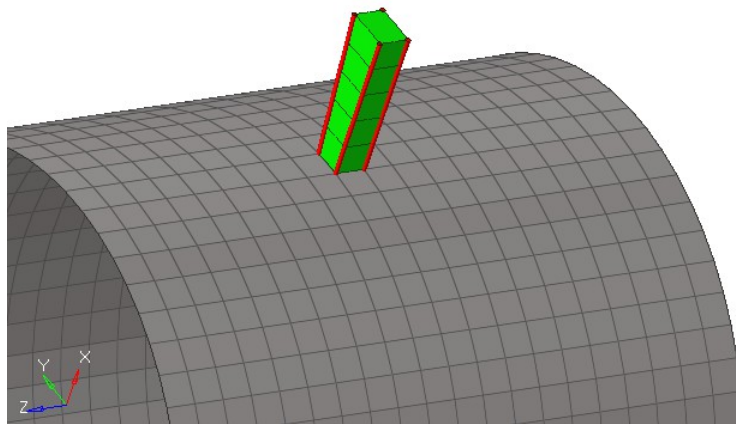


Figure 12.2. FE model. 2D shell and RBE2 in grey. 3D solid elements in green

A standard finite element solver is called to derive the radial equilibrium configuration of the brick elements, and hence the ILTS distribution, as function of the imposed rigid bar roto-translation. There is no rigid body motion as the rigid bars are not mutually parallel, so the radial motion is elastically constrained.

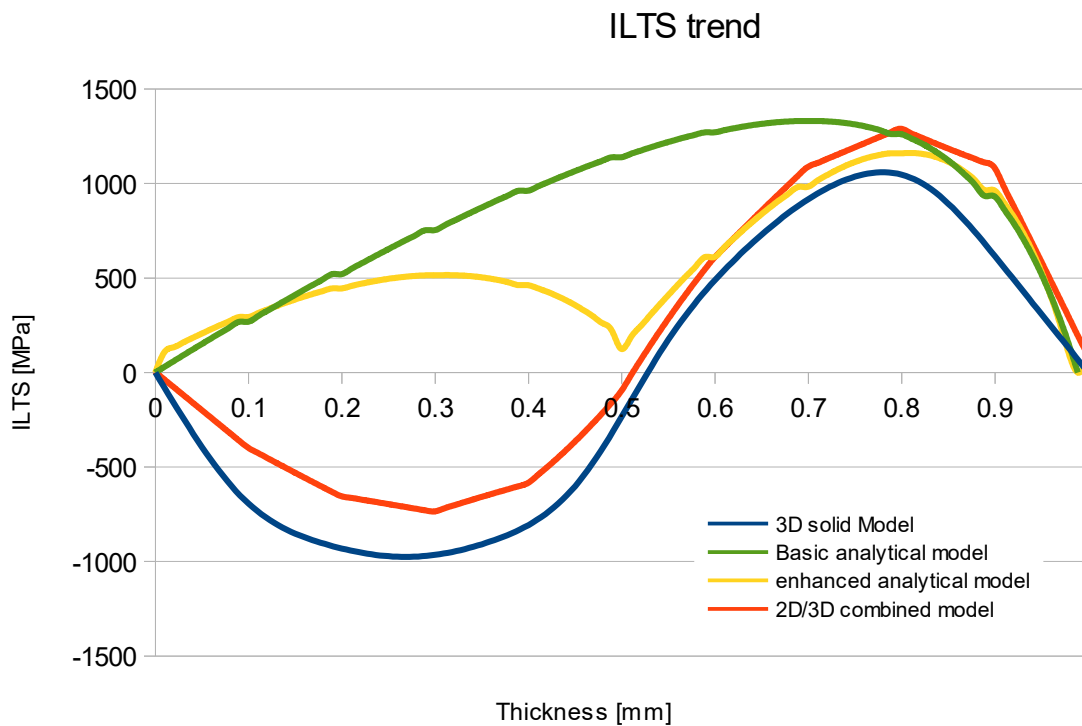


Figure 12.3. ILTS through-the-thickness comparison

The ILTS through-the-thickness trend of the most stressed element is illustrated in Fig. 12.3. The ILTS results calculated with the 2D/3D global/local model have the same trend as the 3D solid FE model, indeed the first half of laminate angular section is in compression while the other half is in traction. The error on maximum ILTS value is +20% for the 2D/3D global/local model, +40% for the basic analytical model and +11% for the enhanced analytical model respect to the 3D solid model. Moreover, the error on the compressive ILTS peak predicted by the 2D/3D global/local model is around 20% too. This method created to check the analytical model differential equilibrium could actually be implemented as a post processing method, with all the computational cost benefits deriving by this type of methods. The present method for retrieving the ILTS at post-processing belongs to the wider family of global-local approaches. From the computational point of view it benefits of the assumed decoupling of the local scale response (i.e. the radial equilibrium assessment of the hexahedral element row) from the global scale response (the shell element assembly which embodies the loaded component). In particular, since the procedure employs an unmodified shell model as a starting point, no further numerical cost is added at the global solution stage. The ILTS calculation procedure involves - for each element subject to this further scrutiny - the solution of a very frugal FE submodel, which in the representative case of Fig. [XXX il sigaro] involves only 44 nodes (ten element layers involve eleven layers of nodes, each of which consists in four nodes; the four Rigid Links control nodes are fully constrained and hence not counted), whose only active d.o.f. is the radial displacement. Due to the massive presence of MPCs (MultiPoint Constraint) the system matrix is dense, but still very tiny. In the proposed example, the matrix solution step at the single element local stage required 0.04s on a single 2.5GHz Sandy Bridge class CPU core; it is however expected that such a performance may be greatly increased with a dedicated small matrix solver, and some basic optimization. Moreover, the evaluation of ILTS for a set of elements may be performed in parallel.

13. Design application: Ferrari Formula

One Front Wing

The enhanced post processing analytical model is in the end tested on an actual component designed under strict constraints of stiffness and strength. The model in question is a Ferrari F1 Front Wing. Because of industrial secrecy, the model is also tested on a less “attractive” project. The model is a Ferrari F138 properly morphed Front Wing, the laminates are simplified and the material used are those presented in table 1 and 2 for all the previous tests. the Leading edge is oriented along X-, while the width of the wing is along Y direction. In Fig 13.1 is shown the complete model of the Front wing.

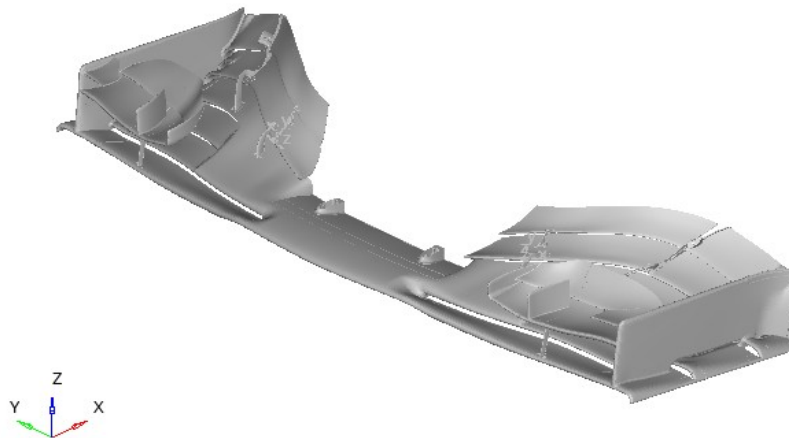


Figure 13.1. Front Wing Model

The mesh consists of 3D tetra elements (CTETRA in Optistruct) for all the solid components parts as Inserts, hooks, stays, Cores, glue, and 2D linear shell elements (CQUAD and CTRIA in Optistruct) for the carbon fiber composite shells. The average mesh size is around 1.5 mm in the critical areas and 2.5 mm for the rest of the surfaces.

The 2D element normal is set inward and the material reference direction is set along Y direction. The laminate is simplified with respect to the original which is classified, it is divided in big areas and every area consists of a symmetric laminate made by cloths and UDs with a ratio UDs/cloths in the range between 0.15 and 3.5 . The cloths plies are set with a thickness of 0.3mm, while the UDS of 0.15mm. The Main shell has also 2 ribs running along the width into the second element, these are modeled with T- junctions between the shell and themselves. The model consists of 1609797 elements and 481828 nodes. The typical loadcase for a front wing is represented by the aerodynamic force at the maximum speed and the stiffness test done to check the legality. The most challenging test involves the aeroloads at maximum speed plus the inertia along Z, in this case are considered 30G so the total load is around 15 kN. Due to the big amount of results and the complexity of the FE model, in view of the 3D solid model construction, is chosen to shrink the area of interest to the root of the second element. The area highlighted in red , illustrated in Fig. 13.2, is made by a set of 2D shell elements where the analysis will be focused, it consists of top and bottom laminate, no ribs, of the area around $Y = 250$ mm. this area is particularly interested by a high level of inplane stress, has a double geometric curvature with important changes of Radius and has 2 ribs causing stress concentration, that's why is the perfect candidate to check the ILTS along the laminate.

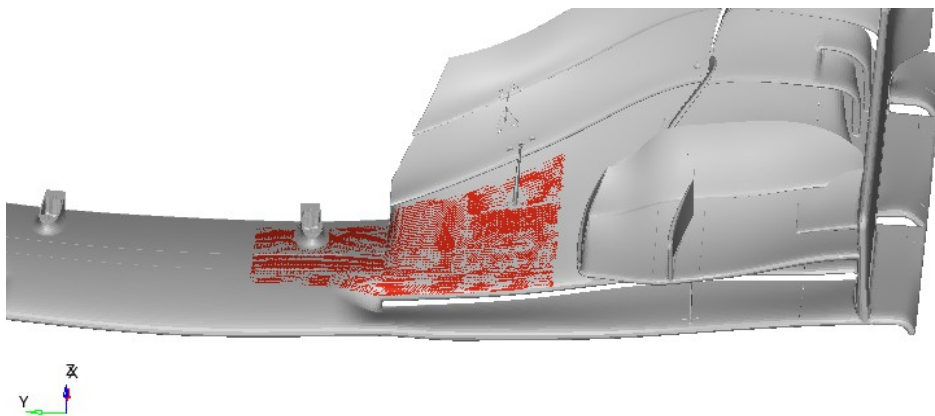


Figure 13.2. In red, the area of interest for ILTS calculation

The results of the 2D FE model calculated are the stresses for both composite and solids, strain of the composites, displacements and forces. They are calculated for all the elements, but the strain required for the post processing analytical model are written in a file apart. The interested area is converted into a 3D solid FE elements. The 3D

elements (CHEXA in Optistruct) are made by extruding the shell elements along their normal, each layer of the laminate is represented by one brick, and along the laminate thickness there are as many bricks as the total number of plies. In Fig. 13.3 is shown a section of the Top extruded laminate. The original 2D shell elements are kept with a dummy non structural property just to transfer the aerodynamic load that was applied to them. The 3D solid elements have their normal inward, as the 2D shells elements, and the material reference direction is set to be along Y.

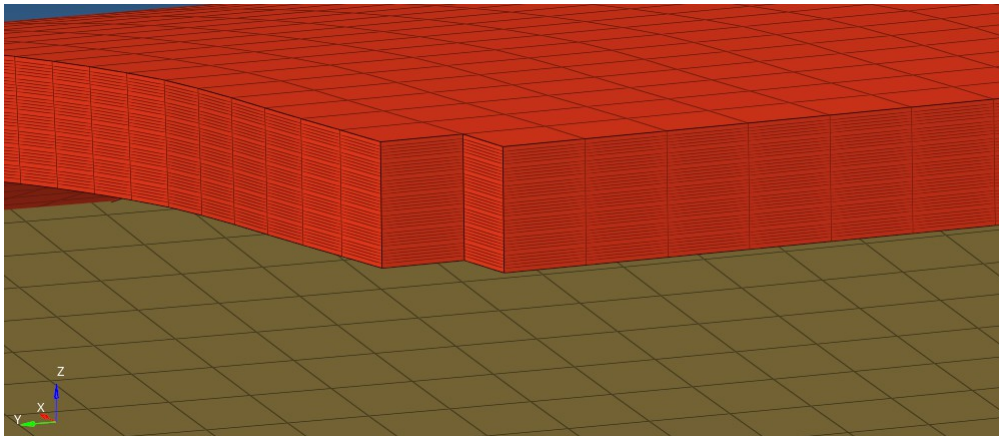


Figure 13.3. 3D solid multilayered model section

The 3D solid elements have been created only in the area of interest around $Y = 250$ mm, which means that the rest of the front wing is still modeled as 2D shell elements. The interface between 3D solid elements and 2D shell elements consist of a flange, as in Fig. 13.4 represented in Bordeaux, of a remarkable thickness. It is made directly from the faces of the 3D solid elements located at the interface. In this way, the 3D solid elements at the interface are supported in all their DoFs.

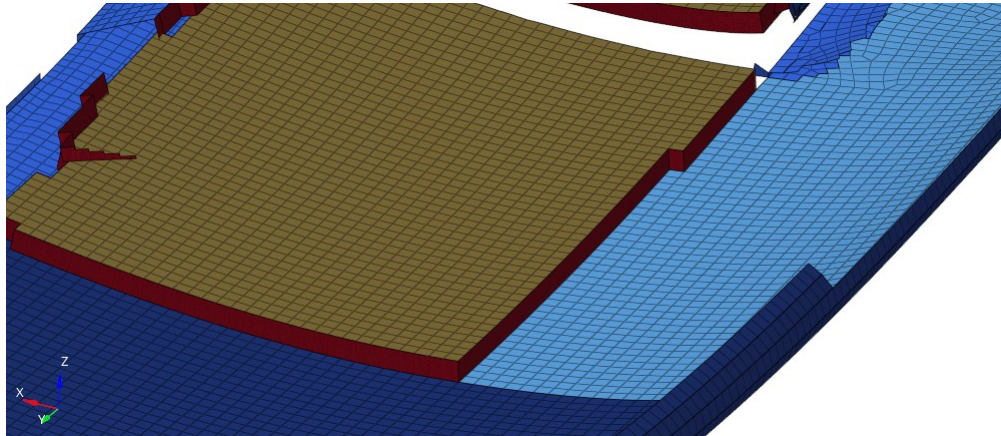


Figure 13.4. Connection Flange between 2D shell and 3D solid model

The same work around has been done for the Ribs interface, indeed a 2D shell flange connects the ribs to the 3D solid elements. At least three elements are covered by the flange to spread the shear load. In Fig. 13.5 the rib's flange is displayed in blue and is attached to the 3D solid elements (in red).

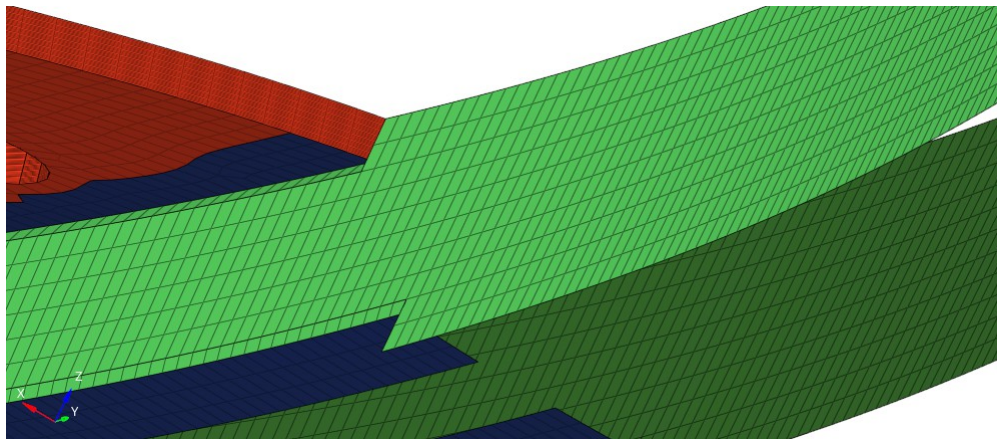


Figure 13.5. In blue the connection flange between main laminate and 2D shell ribs

The 3D solid model is made by 186371 elements and 726574 nodes. Both models are run with the same number of processors and the run time of the 3D solid model, even if only a little part of it is really 3D modeled, is 14 times longer than the 2D shell model. Since the amount of overtime needed by the detailed 3D model respect to the 2D model is enormous, has been tested a simplified 3D solid FE model.

All the bricks of the along the laminate of the 3d solid model have been shrunk into a single solid 8 noded element (CHEXA in Optistruct) with the same property

(PCOMPLS in optistruct), element normal and material reference direction as the 2d model. The single solid 3D element model is made by 1638350 elements and 509189 nodes, and the running time respect to the 2D shell model is “only” 3 times longer. In Fig. 13.6 are compared the 3 FE models in the area of interest, from the left the 2D linear shell model, in the middle the 3D solid model with an accurate representation of the laminate along the thickness (1 brick for each layer) and on the right the 3D solid model simplified .

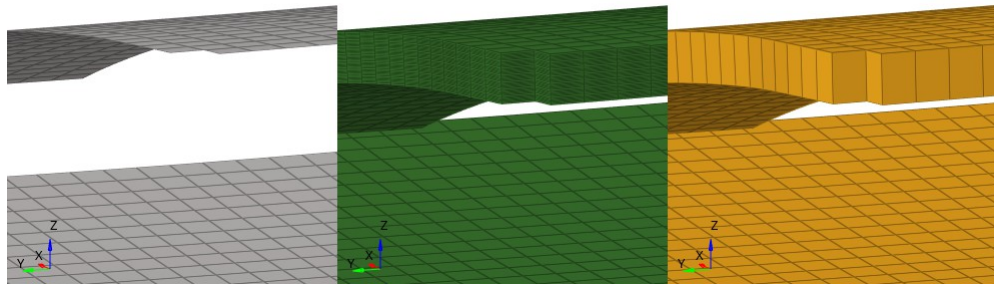


Figure 13.6. Area of interest: on the left 2D shell model, in the middle 3D solid multilayered model, on the right 3D single layer model

13.1 Front Wing FE Test: Results

The first comparison between the three models concerns the stiffness, indeed a 3D brick model has the intrinsic feature to be more compliant than a shell. The table 3 shows how significant is the loss of stiffness of the 3D solid model compared to the 2D shell model with the same applied load (aerodynamic + 30G of gravity). Even if only a portion of the front wing is converted to 3D, a big amount of stiffness loss passing from 2D to 3D is quite justifiable because the area of interest is the “root” of the wing. The 3D solid single brick model is slightly stiffer than the layered 3D solid model, its compliance is 18% against 22% respect to the 2D shell model.

	Delta Compliance
<i>FW 2D shell model</i>	Ref
<i>FW 3D solid single brick model</i>	18%
<i>FW 3D solid model</i>	22%

Table 3. Compliance comparison

About what concerns the ILTS calculation of a complex carbon fiber component as a front wing, the Fig 13.7 illustrates the distribution in the area of interest. On the left there are the 3d solid models, on top the layered 3D model and on bottom the single brick model. On the right the 2D shell mesh with the ILTS results calculated with the post processing analytical model. The results that are shown are normalized. The ILTS results are divided by the maximum, significant, value, and the thicknesses are divided by their maximum.

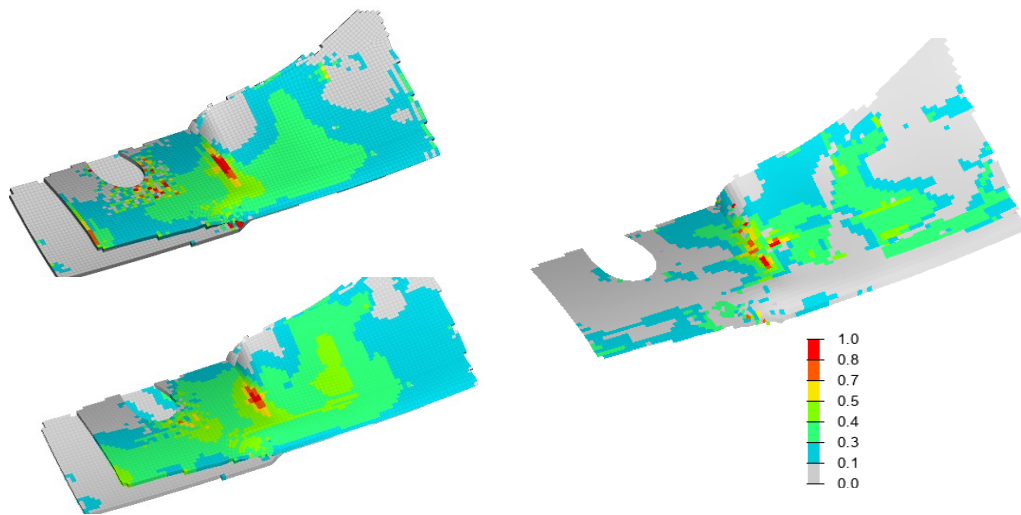


Figure 13.7. ILTS result comparison: leftside, top, multilayered 3D model. Left, bottom, single layer 3D model. Right, 2D shell model with analytical postprocessing results.

As can be seen, the difference between the two solid models is negligible, although the most stressed area appears to be more circumscribed in the single layer model. Moreover the multi layer solid model seems to suffer the checkerboard effect in the area of the insert where there are RBE2 connecting node to node the laminate and the insert bonding. The maximum ILTS is present in the top part of the laminate, indeed in Fig 62 the multilayered model is represented without an ISO cut of the results, because the stresses are high already in the first layer of the laminate. The analytical model is able to highlight the most stressed area that is the change of geometric curvature between the Middle straight section and the curl of the wing. The other stressed region that is

slightly more outboard seems to be over afflicted by the presence of the ribs respect to the 3D solid models, indeed there's a stripe of elements with high ILTS right at the T connection with the ribs as illustrated in Fig. 11.8.

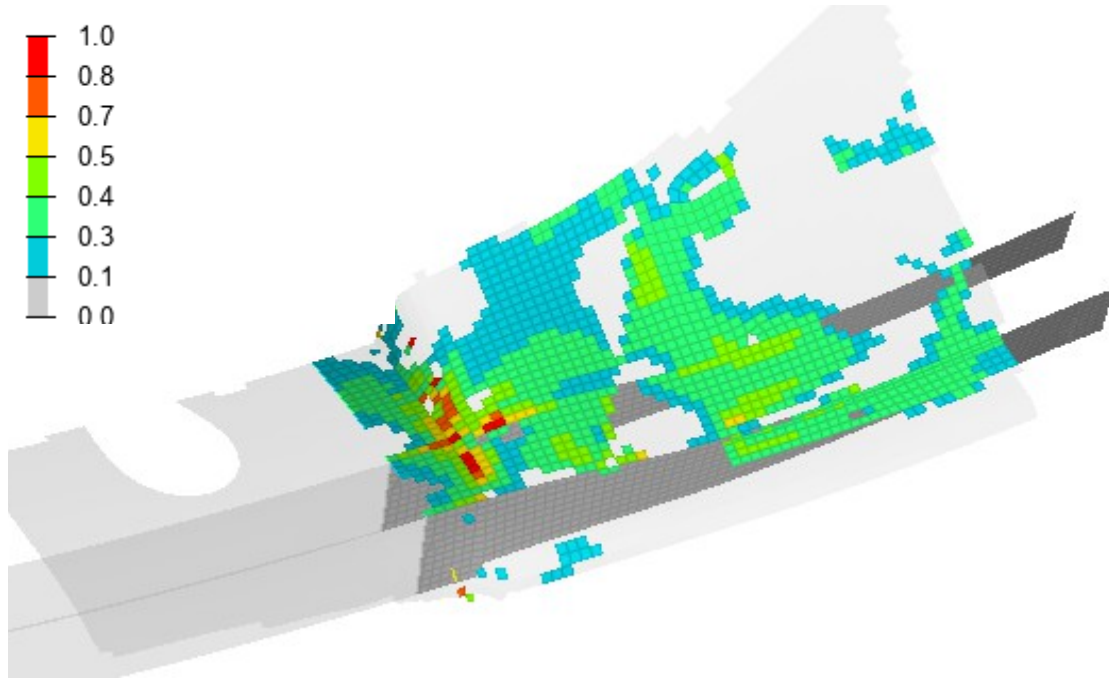


Figure 13.8. analytical model ILTS results on 2D shell model, distribution of stress and rib influence

Moreover, speaking of through-the-thickness ILTS results, in Fig. 11.9 are represented the trend curves along the thickness of the most stressed element. The 3D model has a particular trend of ILTS, indeed the maximum value is among the first plies of the laminate, moreover it does not have a parabolic shape, but near the bottom of the laminate there's another peak of ILTS. This can be explained in the light of the presence of the rib right under the considered element, as can be seen in Fig 11.9 on bottom picture where is represented the ILTS contour of the multilayered solid model. The analytical model calculates the ILTS with the usual parabolic trend, the maximum value is shifted toward the top of the laminate but not as the 3D model is suggesting, additionally it is not able to detect the second peak of ILTS next to the rib. The maximum value of ILTS calculated by the analytical model is underestimated by 20%.

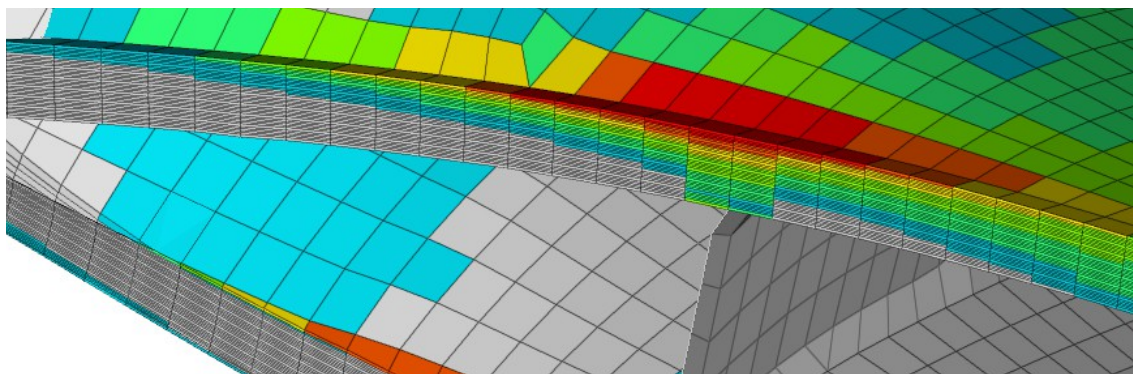
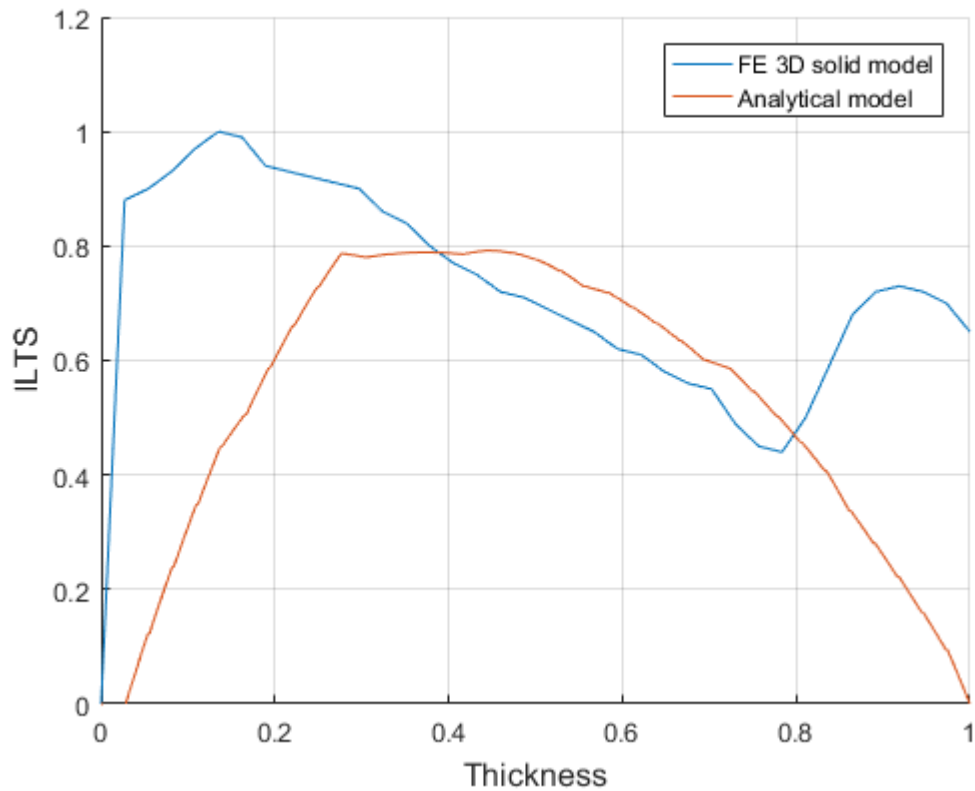


Figure 13.9. ILTS trend along thickness. Top: comparison between 3D solid model and analytical model. Bottom: 3D solid model results section cut in maximum stressed area.

The ILTS Results are normalized with its maximum value.

The thickness is normalized with its maximum value

The enhanced analytical postprocessing method exhibits some difficulties in predicting the ILTS distribution, being unable to observe the camel's back shape of the ILTS through-thickness curve. Further work

14. Conclusions

The postprocessing analytical model presented in this study has been developed with the aim to enrich the results obtainable from a 2D shell FE model, which naturally lacks the ILTS stress component, since it is based on a plane stress hypothesis. The alternative option involving a full 3d representation of the laminate is computationally inefficient. The following results have been developed or revised within the thesis.

- *An analysis of an unavoidable source of error in the postprocessing approach to the ILTS*

In deriving the ILTS distribution at a postprocessing stage, based on FE results obtained through a customary curvature-unaware four noded, quadrilateral shell element model, some error is expected due to the innate inconsistency of the laminate stiffness matrices (i.e. constitutive relations) between the curvature-aware and curvature-unaware shell formulations. Such an inconsistency has been quantified for some commonwise laminates as a function of the curvature radius to thickness ratio, and it has been observed that the curvature-aware formulation is neither consistently stiffer, nor consistently more compliant than its curvature-unaware counterpart, depending such a behaviour on the specific deformation mode. An original analysis tool based on an eigenvalue analysis has been proposed to quantify the issue.

- *Geometric curvature radii estimation techniques:*

Two distinct methods have been implemented and compared, and one of them has been chosen for further development due to the more reliable results it returned for arbitrarily oriented elements and non structured meshes. Both the method rely on an auxiliary eight

noded quadrilateral mesh, which may be easily produced by commonly available FE preprocessors, thus being applicable to each single element regardless of the topology of its neighborhood.

- *Assessment of the ILTS results in single geometric curvature test cases:*

A postprocessing procedure proposed in literature (here named *basic analytical model*) has been tested under various single geometry curvature test cases, and it was found to underestimate the maximum ILTS value of about 10÷20% in a wide 2÷10 interval of the ratio between the geometric curvature radius and the laminate thickness; the prediction capabilities of such method have been observed to significantly decrease for the relatively thicker laminates, whereas for moderately thick laminates (with respect to the curvature radius) the ILTS distribution agrees with the 3D solid model results both in the through-thickness distribution, and along the component midsurface. Such a procedure consistently underestimates the actual maximum ILTS value if compared with a reference 3d brick model; slightly worse accuracy has been observed in the case of unstructured meshes, where the element edges were not aligned with the local principal directions of geometric curvature. It has been however observed that most of the test cases from the literature exhibit material and applied load symmetry with respect to principal directions of geometric curvature; at this point, the basic analytical model has been tested on more general cases, thus evidencing further loss in its ILTS prediction capabilities. An amended version of such a postprocessing procedure, which also includes the contribution of in-plane shear deformation components, has been proposed, which appeared promising. After the consequent update of the finite difference implementation, the obtained enhanced analytical model performs acceptably (less than 20% underestimation of the peak ILTS) even in the case of arbitrarily oriented, highly anisotropic materials (UD plies).

- *Assessment of the ILTS results in double geometric curvature test cases:*

Three different double curvature test cases were analyzed. The enhanced ILTS postprocessing procedure returned results comparable with the control 3d brick model. The ILTS through-thickness peak values are consistently underestimated by 10÷15% in the 5÷33 geom. curvature radius / laminate thickness ratio interval. In the case of thicker (or more curved) laminates, where the aforementioned ratio falls below approximately 4, some overestimation of the peak ILTS value is observed, even though the through-thickness and the along the surface distributions are similar to their counterpart in the 3D control solid models. A specific test has been designed to verify the response of the postprocessing procedure to bodies showing varying geometric curvature values; such a test is of particular interest since a constant double curvature condition is not obtainable on a finite specimen area, but in a few trivial cases. We observed no further issues in ILTS prediction in the presence of mild geometric curvature variation. In general, double curvature test cases showed an error growing with the angular mismatch between the principal directions of orthotropy of the material (highly anisotropic UD plies), and the principal directions of curvature; being the observed error bounded in the 20% range, it was considered acceptable based on the curvature-awareness model discrepancies.

- *A further test case to verify the postprocessing analytical method with respect to angular misalignment between principal directions of curvature, and principal directions of strain.*

The test has been developed, which was not previously considered in literature, to further investigate the limits of the proposed postprocessing analytical method, both in the basic and in the shear strain enriched versions. A single curvature geometry is

employed, with 45° inclined principal directions of material orthotropy and of strain; an S-shaped ILTS through-thickness distribution, spanning both the compressive and the tensile ranges has been obtained in the 3d brick control model, which was not previously analyzed in literature. A substantial failure of the postprocessing analytical methods was sadly observed in predicting such a behavior; the basic analytical model returned in fact a single ILTS tractive peak, whereas two peaks were correctly predicted by the enhanced model, but both again in the tractive range.

Such a novel test case urged for a redefinition of the ILTS retrieval procedure.

- *An alternative to the analytical postprocessing model based on the local 3d brick representation of an element extracted from the global 2d shell model.*

A further technique for retrieving ILTS distribution at the postprocessing stage of a 2D shell model calculation has been defined from scratch, that returns acceptable results even in the last test case described above; the plate element nodal displacements and rotations are sampled in place of the strains, and a dedicated finite element 3D brick local model is employed, whose radial equilibrium in stretched condition is calculated by a standard FE solver (vs. a dedicated finite difference procedure). Such a technique correctly predicts the S-shaped, through-thickness evolution of the ILTS, and it predicts both the tractive and the compressive peak values with a 20% overestimation error, which is in line with that induced by the curvature-awareness inconsistency of the laminate constitutive law for the specific curvature radius to thickness ratio of 1.

Such a local 3D FE approach is suggested for application in the general case of principal directions of strains not aligned with the principal directions of curvature.

- *Application to a Formula One Front wing*

The proposed enhanced analytical method has been benchmarked on an actual component whose complexity emphasizes the computational cost advantages of a 2D shell FE model calculation, combined with the proposed post processing analysis. The maximum ILTS value calculated by the postprocessing procedure underestimates by 20% the value returned by the control 3D solid model, thus returning a result which is in line with respect to the previous tests performed on simpler geometries, with the notable exceptions of the component areas in the proximity of T connections with stiffening or attachment ribs, which perturb too sharply the geometry of the shell midsurface. In particular, the complex FE model emphasizes the inability of the postprocessing procedure to reliably predict a through-thickness ILTS camel's back variation in the vicinity of the connection to the rib.

REFERENCES

- [1] N. N. Huang e T. R. Tauchert, «Thermal stresses in doubly-curved cross-ply laminates», *Int. J. Solids Struct.*, vol. 29, n. 8, pagg. 991–1000, 1992, doi: 10.1016/0020-7683(92)90070-A.
- [2] R. Roos, G. Kress, e P. Ermanni, «A post-processing method for interlaminar normal stresses in doubly curved laminates», *Compos. Struct.*, vol. 81, n. 3, pagg. 463–470, dic. 2007, doi: 10.1016/j.compstruct.2006.09.016.
- [3] R. Roos, «Model for interlaminar normal stresses in doubly curved laminates», PhD Thesis, ETH Zurich, 2008.
- [4] T. W. Clyne e D. Hull, *An introduction to composite materials*. Cambridge university press.
- [5] R. Gibson, *Principles of Composite Material Mechanics*. .
- [6] M. R. Wisnom, Z. J. Petrossian, e M. I. Jones, «Interlaminar failure of unidirectional glass/epoxy due to combined through thickness shear and tension», *Compos. Part Appl. Sci. Manuf.*, vol. 27, n. 10, pagg. 921–929, gen. 1996, doi: 10.1016/1359-835X(96)00038-3.
- [7] P. N. B. Reis, J. A. M. Ferreira, F. V. Antunes, e M. O. W. Richardson, «Effect of Interlayer Delamination on Mechanical Behavior of Carbon/Epoxy Laminates», *J. Compos. Mater.*, vol. 43, n. 22, pagg. 2609–2621, ott. 2009, doi: 10.1177/0021998309344649.
- [8] A. M. Amaro, P. N. B. Reis, e M. F. S. F. de Moura, «Residual Strength after Low Velocity Impact in Carbon-Epoxy Laminates», *Mater. Sci. Forum*, vol. 514–516, pagg. 624–628, mag. 2006, doi: 10.4028/www.scientific.net/MSF.514-516.624.
- [9] A. M. Amaro, P. N. B. Reis, e M. F. S. F. de Moura, «Delamination Effect on Bending Behaviour in Carbon-Epoxy Composites: Bending Behaviour in Carbon-Epoxy Composites», *Strain*, vol. 47, n. 2, pagg. 203–208, apr. 2011, doi: 10.1111/j.1475-1305.2008.00520.x.
- [10] C. T. Herakovich, «On the Relationship between Engineering Properties and Delamination of Composite Materials», *J. Compos. Mater.*, vol. 15, n. 4, pagg. 336–348, lug. 1981, doi: 10.1177/002199838101500404.

- [11] R. Pipes, R. Byron, e N. J. Pagano, «Interlaminar stresses in composite laminates under uniform axial extension», *Mechanics of composite materials*, pagg. 234–245, 1994.
- [12] P. W. Hsu e C. T. Herakovich, «Edge Effects in Angle-Ply Composite Laminates*», *J. Compos. Mater.*, vol. 11, n. 4, pagg. 422–428, ott. 1977, doi: 10.1177/002199837701100405.
- [13] A. C. Garg, «Delamination—a damage mode in composite structures», *Eng. Fract. Mech.*, vol. 29, n. 5, pagg. 557–584, gen. 1988, doi: 10.1016/0013-7944(88)90181-6.
- [14] W. Hintze, D. Hartmann, e C. Schütte, «Occurrence and propagation of delamination during the machining of carbon fibre reinforced plastics (CFRPs) – An experimental study», *Compos. Sci. Technol.*, vol. 71, n. 15, pagg. 1719–1726, ott. 2011, doi: 10.1016/j.compscitech.2011.08.002.
- [15] D. Geng *et al.*, «Delamination formation, evaluation and suppression during drilling of composite laminates: A review», *Compos. Struct.*, vol. 216, pagg. 168–186, mag. 2019, doi: 10.1016/j.compstruct.2019.02.099.
- [16] A. M. Amaro, P. N. B. Reis, M. F. S. F. de Moura, e M. A. Neto, «Influence of open holes on composites delamination induced by low velocity impact loads», *Compos. Struct.*, vol. 97, pagg. 239–244, mar. 2013, doi: 10.1016/j.compstruct.2012.09.041.
- [17] S.-X. Wang, L.-Z. Wu, e L. Ma, «Low-velocity impact and residual tensile strength analysis to carbon fiber composite laminates», *Mater. Des.*, vol. 31, n. 1, pagg. 118–125, gen. 2010, doi: 10.1016/j.matdes.2009.07.003.
- [18] J. A. Nairn e S. Hu, «The initiation and growth of delaminations induced by matrix microcracks in laminated composites», *Int. J. Fract.*, vol. 57, n. 1, pagg. 1–24, set. 1992, doi: 10.1007/BF00013005.
- [19] J. Wang e B. L. Karihaloo, «Matrix crack-induced delamination in composite laminates under transverse loading», *Compos. Struct.*, vol. 38, n. 1–4, pagg. 661–666, mag. 1997, doi: 10.1016/S0263-8223(97)00103-7.
- [20] H. J. Phillips e R. A. Shenoi, «Damage tolerance of laminated tee joints in FRP structures», *Compos. Part Appl. Sci. Manuf.*, vol. 29, n. 4, pagg. 465–478, gen. 1998, doi: 10.1016/S1359-835X(97)00081-X.
- [21] J. Fan, X. Cheng, S. Wang, X. Guo, e T. Zhang, «Experimental and numerical

- investigation of composite bolted π -joint subjected to bending load», *Compos. Part B Eng.*, vol. 78, pagg. 324–330, set. 2015, doi: 10.1016/j.compositesb.2015.03.094.
- [22] L. Tong, «An Assessment of Failure Criteria to Predict the Strength of Adhesively Bonded Composite Double Lap Joints», *J. Reinf. Plast. Compos.*, vol. 16, n. 8, pagg. 698–713, mag. 1997, doi: 10.1177/073168449701600803.
- [23] P. P. Camanho, C. G. Davila, e M. F. de Moura, «Numerical Simulation of Mixed-Mode Progressive Delamination in Composite Materials», *J. Compos. Mater.*, vol. 37, n. 16, pagg. 1415–1438, ago. 2003, doi: 10.1177/0021998303034505.
- [24] C. Kassapoglou e P. A. Lagace, «Closed Form Solutions for the Interlaminar Stress Field in Angle-Ply and Cross-Ply Laminates», *J. Compos. Mater.*, vol. 21, n. 4, pagg. 292–308, apr. 1987, doi: 10.1177/002199838702100401.
- [25] C. Kassapoglou, «Determination of Interlaminar Stresses in Composite Laminates under Combined Loads», *J. Reinf. Plast. Compos.*, vol. 9, n. 1, pagg. 33–58, gen. 1990, doi: 10.1177/073168449000900103.
- [26] X. Lu e D. Liu, «An Interlaminar Shear Stress Continuity Theory for Both Thin and Thick Composite Laminates», *J. Appl. Mech.*, vol. 59, n. 3, pagg. 502–509, set. 1992, doi: 10.1115/1.2893752.
- [27] X. Wang e S. J. Li, «Analytic solution for interlaminar stresses in a multilaminated cylindrical shell under thermal and mechanical loads», *Int. J. Solids Struct.*, vol. 29, n. 10, pagg. 1293–1302, 1992, doi: 10.1016/0020-7683(92)90239-P.
- [28] M. P. Connolly, «Simplified Equations for Interlaminar Stresses in Cross-Ply Laminates», *J. Reinf. Plast. Compos.*, vol. 13, n. 11, pagg. 1043–1053, nov. 1994, doi: 10.1177/073168449401301105.
- [29] J.-F. He, «Static Analysis of Laminated Shells Using a Refined Shear Deformation Theory», *J. Reinf. Plast. Compos.*, vol. 14, n. 7, pagg. 652–674, lug. 1995, doi: 10.1177/073168449501400701.
- [30] K. Rohwer e R. Rolfes, «Calculating 3D stresses in layered composite plates and shells», *Mech. Compos. Mater.*, vol. 34, n. 4, pagg. 355–362, lug. 1998, doi: 10.1007/BF02257903.
- [31] H. Matsunaga, «Interlaminar stress analysis of laminated composite and sandwich circular arches subjected to thermal/mechanical loading», *Compos. Struct.*, vol. 60, n. 3, pagg. 345–358, mag. 2003, doi: 10.1016/S0263-8223(02)00340-9.

- [32] G. Kirchhoff, «Über das Gleichgewicht und die Bewegung einer elastischen Scheibe», *Journal für Reine und Angewandte Mathematik*, 1850.
- [33] J. M. Whitney e N. J. Pagano, «Shear Deformation in Heterogeneous Anisotropic Plates», *J. Appl. Mech.*, vol. 37, n. 4, pagg. 1031–1036, dic. 1970, doi: 10.1115/1.3408654.
- [34] J. M. Whitney, «The Effect of Transverse Shear Deformation on the Bending of Laminated Plates», *J. Compos. Mater.*, vol. 3, n. 3, pagg. 534–547, mar. 1969, doi: 10.1177/002199836900300316.
- [35] J. N. Reddy, «A Simple Higher-Order Theory for Laminated Composite Plates», *J. Appl. Mech.*, vol. 51, n. 4, pagg. 745–752, dic. 1984, doi: 10.1115/1.3167719.
- [36] F. Auricchio e E. Sacco, «Refined First-Order Shear Deformation Theory Models for Composite Laminates», *J. Appl. Mech.*, vol. 70, n. 3, pagg. 381–390, mag. 2003, doi: 10.1115/1.1572901.
- [37] R. Rolfes, K. Rohwer, e M. Ballerstaedt, «Efficient linear transverse normal stress analysis of layered composite plates», *Comput. Struct.*, vol. 68, n. 6, pagg. 643–652, set. 1998, doi: 10.1016/S0045-7949(98)00097-2.
- [38] A. Nosier e A. Bahrami, «Interlaminar stresses in antisymmetric angle-ply laminates», *Compos. Struct.*, vol. 78, n. 1, pagg. 18–33, mar. 2007, doi: 10.1016/j.compstruct.2005.08.007.
- [39] D. H. Robbins e J. N. Reddy, «Modelling of thick composites using a layerwise laminate theory», *Int. J. Numer. Methods Eng.*, vol. 36, n. 4, pagg. 655–677, feb. 1993, doi: 10.1002/nme.1620360407.
- [40] S. J. Hossain, P. K. Sinha, e A. H. Sheikh, «A finite element formulation for the analysis of laminated composite shells», *Comput. Struct.*, vol. 82, n. 20–21, pagg. 1623–1638, ago. 2004, doi: 10.1016/j.compstruc.2004.05.004.
- [41] T. O. Williams, «A generalized, multilength scale framework for thermo-diffusional-mechanically coupled, nonlinear, laminated plate theories with delaminations», *Int. J. Solids Struct.*, vol. 42, n. 5–6, pagg. 1465–1490, mar. 2005, doi: 10.1016/j.ijsolstr.2004.08.007.
- [42] F. Tornabene, A. Liverani, e G. Caligiana, «Static analysis of laminated composite curved shells and panels of revolution with a posteriori shear and normal stress recovery using generalized differential quadrature method», *Int. J. Mech. Sci.*, vol. 61, n. 1, pagg. 71–87, ago. 2012, doi: 10.1016/j.ijmecsci.2012.05.007.

- [43] J. M. Hamdallah e J. J. Engblom, «Finite Element Plate Formulation Including Transverse Shear Effects for Representing Composite Shell Structures», *J. Reinf. Plast. Compos.*, vol. 9, n. 3, pagg. 226–239, mag. 1990, doi: 10.1177/073168449000900302.
- [44] C.-P. Wu e H.-C. Kuo, «An interlaminar stress mixed finite element method for the analysis of thick laminated composite plates», *Compos. Struct.*, vol. 24, n. 1, pagg. 29–42, gen. 1993, doi: 10.1016/0263-8223(93)90052-R.
- [45] W. Chih-Ping e Y. Chung-Bing, «Interlaminar stress mixed finite element analysis of unsymmetrically laminated composite plates», *Comput. Struct.*, vol. 49, n. 3, pagg. 411–419, nov. 1993, doi: 10.1016/0045-7949(93)90042-C.
- [46] R. Tanov e A. Tabiei, «Adding transverse normal stresses to layered shell finite elements for the analysis of composite structures», *Compos. Struct.*, vol. 76, n. 4, pagg. 338–344, dic. 2006, doi: 10.1016/j.compstruct.2005.05.007.
- [47] F. Tornabene, N. Fantuzzi, M. Baccocchi, e E. Viola, «A new approach for treating concentrated loads in doubly-curved composite deep shells with variable radii of curvature», *Compos. Struct.*, vol. 131, pagg. 433–452, nov. 2015, doi: 10.1016/j.compstruct.2015.05.049.
- [48] J. Y. Kim e C. S. Hong, «Three-dimensional finite element analysis of interlaminar stresses in thick composite laminates», *Comput. Struct.*, vol. 40, n. 6, pagg. 1395–1404, gen. 1991, doi: 10.1016/0045-7949(91)90410-N.
- [49] C. G. Davila e E. R. Johnson, «Analysis of Delamination Initiation in Postbuckled Dropped-Ply Laminates», *AIAA J.*, vol. 31, n. 4, pagg. 721–727, apr. 1993, doi: 10.2514/3.49019.
- [50] A. Schiffer e V. L. Tagarielli, «Predictions of the interlaminar tensile failure of a carbon/epoxy composite laminate», *Compos. Struct.*, vol. 133, pagg. 997–1008, dic. 2015, doi: 10.1016/j.compstruct.2015.07.070.
- [51] R. Krueger e T. K. O'Brien, «A shell/3D modeling technique for the analysis of delaminated composite laminates», *Compos. Part Appl. Sci. Manuf.*, vol. 32, n. 1, pagg. 25–44, gen. 2001, doi: 10.1016/S1359-835X(00)00133-0.
- [52] R. Krueger e P. J. Minguet, «Analysis of composite skin–stiffener debond specimens using a shell/3D modeling technique», *Compos. Struct.*, vol. 81, n. 1, pagg. 41–59, nov. 2007, doi: 10.1016/j.compstruct.2006.05.006.
- [53] R. Krueger, «Virtual crack closure technique: History, approach, and applications»,

- Appl. Mech. Rev.*, vol. 57, n. 2, pagg. 109–143, mar. 2004, doi: 10.1115/1.1595677.
- [54] R. Krueger, «The virtual crack closure technique for modeling interlaminar failure and delamination in advanced composite materials», in *Numerical Modelling of Failure in Advanced Composite Materials*, Elsevier, 2015, pagg. 3–53.
- [55] E. Pietropaoli e A. Riccio, «A Global/Local Finite Element Approach for Predicting Interlaminar and Intralaminar Damage Evolution in Composite Stiffened Panels Under Compressive Load», *Appl. Compos. Mater.*, vol. 18, n. 2, pagg. 113–125, apr. 2011, doi: 10.1007/s10443-010-9135-1.
- [56] T. E. Tay, F. Shen, K. H. Lee, A. Scaglione, e M. Di Sciuva, «Mesh design in finite element analysis of post-buckled delamination in composite laminates», *Compos. Struct.*, vol. 47, n. 1–4, pagg. 603–611, dic. 1999, doi: 10.1016/S0263-8223(00)00033-7.
- [57] D. H. Li, «Delamination and transverse crack growth prediction for laminated composite plates and shells», *Comput. Struct.*, vol. 177, pagg. 39–55, dic. 2016, doi: 10.1016/j.compstruc.2016.07.011.
- [58] C. G. Davila, P. Camanho, e A. Turon, «Cohesive Elements for Shells», 2007.
- [59] B. Li, Y. Li, e J. Su, «A combined interface element to simulate interfacial fracture of laminated shell structures», *Compos. Part B Eng.*, vol. 58, pagg. 217–227, mar. 2014, doi: 10.1016/j.compositesb.2013.10.038.
- [60] M. Soroush, K. M. Fard, e M. Shahravi, «Finite Element Simulation of Interlaminar and Intralaminar Damage in Laminated Composite Plates Subjected to Impact», *Lat. Am. J. Solids Struct.*, vol. 15, n. 6, lug. 2018, doi: 10.1590/1679-78254609.
- [61] Z. Mikulik, D. W. Kelly, B. G. Prusty, e R. S. Thomson, «Prediction of initiation and growth of single level delaminations in a transversely loaded composite specimen using fracture mechanics», *Int. J. Fract.*, vol. 149, n. 2, pagg. 119–141, feb. 2008, doi: 10.1007/s10704-008-9220-8.
- [62] B. D. Davidson, «Analytical Determination of Mixed-Mode Energy Release Rates for Delamination Using a Crack Tip Element», *Key Eng. Mater.*, vol. 120–121, pagg. 161–180, mag. 1996, doi: 10.4028/www.scientific.net/KEM.120-121.161.
- [63] Q. Ye e P. Chen, «Prediction of the cohesive strength for numerically simulating composite delamination via CZM-based FEM», *Compos. Part B Eng.*, vol. 42, n. 5, pagg. 1076–1083, lug. 2011, doi: 10.1016/j.compositesb.2011.03.021.

- [64] C. Davila, P. Camanho, e M. de Moura, «Mixed-mode decohesion elements for analyses of progressive delamination», presentato al 19th AIAA Applied Aerodynamics Conference, Anaheim, CA, U.S.A., giu. 2001, doi: 10.2514/6.2001-1486.
- [65] M. R. Wisnom, «Modelling discrete failures in composites with interface elements», *Compos. Part Appl. Sci. Manuf.*, vol. 41, n. 7, pagg. 795–805, lug. 2010, doi: 10.1016/j.compositesa.2010.02.011.
- [66] A. Gliszczynski, S. Samborski, N. Wiacek, e J. Rzczkowski, «Mode I Interlaminar Fracture of Glass/Epoxy Unidirectional Laminates. Part II: Numerical Analysis», *Materials*, vol. 12, n. 10, pag. 1604, mag. 2019, doi: 10.3390/ma12101604.
- [67] E. V. Iarve, M. R. Gurvich, D. H. Mollenhauer, C. A. Rose, e C. G. Dávila, «Mesh-independent matrix cracking and delamination modeling in laminated composites», *Int. J. Numer. Methods Eng.*, vol. 88, n. 8, pagg. 749–773, nov. 2011, doi: 10.1002/nme.3195.
- [68] T. Belytschko, R. Gracie, e G. Ventura, «A review of extended/generalized finite element methods for material modeling», *Model. Simul. Mater. Sci. Eng.*, apr. 2009.
- [69] M. McElroy, «An Enriched Shell Element for Delamination Simulation in Composite Laminates», set. 28, 2015.
- [70] M. McElroy, «Use of an enriched shell finite element to simulate delamination-migration in a composite laminate», *Compos. Struct.*, vol. 167, pagg. 88–95, mag. 2017, doi: 10.1016/j.compstruct.2017.01.057.
- [71] B. Y. Chen, S. T. Pinho, N. V. De Carvalho, P. M. Baiz, e T. E. Tay, «A floating node method for the modelling of discontinuities in composites», *Eng. Fract. Mech.*, vol. 127, pagg. 104–134, set. 2014, doi: 10.1016/j.engfracmech.2014.05.018.
- [72] S. Medikonda e A. Tabiei, «Studying delamination in composite laminates using shell elements and a strain-rate-dependent micro-mechanical model», *J. Compos. Mater.*, vol. 53, n. 28–30, pagg. 4015–4034, dic. 2019, doi: 10.1177/0021998319853024.
- [73] R. P. R. Cardoso e J. W. Yoon, «One point quadrature shell element with through-thickness stretch», *Comput. Methods Appl. Mech. Eng.*, vol. 194, n. 9–11, pagg.

- 1161–1199, mar. 2005, doi: 10.1016/j.cma.2004.06.017.
- [74] A. Hansbo e P. Hansbo, «A finite element method for the simulation of strong and weak discontinuities in solid mechanics», *Comput. Methods Appl. Mech. Eng.*, vol. 193, n. 33–35, pagg. 3523–3540, ago. 2004, doi: 10.1016/j.cma.2003.12.041.
- [75] B. Chen, S. T. Pinho, P. M. Baiz, e T. E. Tay, «AN EXTENDED PHANTOM NODE METHOD FOR CRACK INTERACTIONS IN COMPOSITES», *Blucher Mechanical Engineering Proceedings*, 2012.
- [76] D. De Cicco e F. Taheri, «Delamination Buckling and Crack Propagation Simulations in Fiber-Metal Laminates Using xFEM and Cohesive Elements», *Appl. Sci.*, vol. 8, n. 12, pag. 2440, dic. 2018, doi: 10.3390/app8122440.
- [77] L. Demasi, Y. Ashenafi, R. Cavallaro, e E. Santarpia, «Generalized Unified Formulation shell element for functionally graded Variable-Stiffness Composite Laminates and aeroelastic applications», *Compos. Struct.*, vol. 131, pagg. 501–515, nov. 2015, doi: 10.1016/j.compstruct.2015.05.022.
- [78] P. Davies, B. R. K. Blackman, e Brunner, «Standard Test Methods for Delamination Resistance of Composite Materials: Current Status», *Appl. Compos. Mater.*, vol. Volume 5, n. Issue 6, pag. pp 345–364, nov. 1998.
- [79] Wilkins, Eisenmann, Camin, Margolis, e Benson, «ASTM STP 775», in *Damage in Composite Materials: Basic Mechanisms, Accumulation, Tolerance, and Characterization*, .
- [80] D30 Committee, «Test Method for Measuring the Curved Beam Strength of a Fiber-Reinforced Polymer-Matrix Composite», ASTM International. doi: 10.1520/D6415_D6415M-06AR13.
- [81] D30 Committee, «Test Method for Through-Thickness Flatwise Tensile Strength and Elastic Modulus of a Fiber-Reinforced Polymer Matrix Composite Material», ASTM International. doi: 10.1520/D7291_D7291M-07.
- [82] J.-S. Charrier, F. Laurin, N. Carrere, e S. Mahdi, «Determination of the out-of-plane tensile strength using four-point bending tests on laminated L-angle specimens with different stacking sequences and total thicknesses», *Compos. Part Appl. Sci. Manuf.*, vol. 81, pagg. 243–253, feb. 2016, doi: 10.1016/j.compositesa.2015.11.018.
- [83] A. Makeev, G. Seon, Y. Nikishkov, e E. Lee, «Methods for assessment of interlaminar tensile strength of composite materials», *J. Compos. Mater.*, vol. 49,

- n. 7, pagg. 783–794, mar. 2015, doi: 10.1177/0021998314525979.
- [84] W. Jackson e R. Martin, «An Interlaminar Tensile Strength Specimen», in *Eleventh Volume: Composite Materials—Testing and Design*, E. Camponeschi, A c. di 100 Barr Harbor Drive, PO Box C700, West Conshohocken, PA 19428-2959: ASTM International, 1993, pagg. 333-333–22.
- [85] M. R. Wisnom e J. W. Atkinson, «Reduction in tensile and flexural strength of unidirectional glass fibre-epoxy with increasing specimen size», *Compos. Struct.*, vol. 38, n. 1–4, pagg. 405–411, mag. 1997, doi: 10.1016/S0263-8223(97)00075-5.
- [86] F. Bosia, M. Facchini, J. Botsis, T. Gmür, e D. de’Sena, «Through-the-thickness distribution of strains in laminated composite plates subjected to bending», *Compos. Sci. Technol.*, vol. 64, n. 1, pagg. 71–82, gen. 2004, doi: 10.1016/S0266-3538(03)00201-X.
- [87] G. Kress, R. Roos, M. Barbezat, C. Dransfeld, e P. Ermanni, «Model for interlaminar normal stress in singly curved laminates», *Compos. Struct.*, vol. 69, n. 4, pagg. 458–469, ago. 2005, doi: 10.1016/j.compstruct.2004.08.026.
- [88] S. Hahmann, «Visualization techniques for surface analysis», *Data Vis. Tech.*, pagg. 49–74, 1999.
- [89] S. G. Lekhnitskii, «ANISOTROPIC PLATES», mar. 01, 1968.
- [90] G. Evangelisti, «Il calcolo delle differenze finite nella matematica applicata: Conferenza tenuta il 15-3-1955», *Rendiconti Semin. Mat. E Fis. Milano*, vol. 26, n. 1, pagg. 69–87, dic. 1956, doi: 10.1007/BF02957789.
- [91] T. Y. Na, *Computational Methods in Engineering Boundary Value Problems*, Academic Press. 1980.
- [92] K. T. Kedward, R. S. Wilson, e S. K. McLean, «Flexure of simply curved composite shapes», *Composites*, vol. 20, n. 6, pagg. 527–536, nov. 1989, doi: 10.1016/0010-4361(89)90911-7.
- [93] *Marc® and Mentat® 2016*. MSC Software Corporation.
- [94] © 1994-2020 *The MathWorks, Inc.* .
- [95] John W. Eaton, *GNU Octave Manual*. Network Theory Limited.
- [96] «Altair® HyperWorks® v. 2017.2 - Optistruct». .
- [97] L. Marchignoli, «Valutazione numerica della componente normale di tensione in un laminato a doppia curvatura», Università degli studi di Modena e Reggio Emilia.

- [98] C. Wuthrich, «Thick-walled composite tubes under mechanical and hygrothermal loading», *Composites*, vol. 23, n. 6, pagg. 407–413, nov. 1992, doi: [https://doi.org/10.1016/0010-4361\(92\)90003-D](https://doi.org/10.1016/0010-4361(92)90003-D).